UNIVERSITY OF OTTAWA

DOCTORAL THESIS

Fabrication of III-V integrated photonic devices

Author:
Kashif AWAN

Supervisors:
Prof. Ksenia DOLGALEVA and Prof. Robert BOYD

A thesis submitted in partial fulfillment of the requirements for the degree of Doctor of Philosophy

uOttawa

Faculté de génie
Faculty of Engineering

Ottawa-Carleton Institute for Electrical and Computer Engineering
University of Ottawa

Declaration of Authorship

I, Kashif AWAN, declare that this thesis, titled "Fabrication of III-V integrated photonic devices", and the work presented in it are my own. I confirm that except where specific reference is made to the work of others, the contents of this dissertation are original and have not been submitted in whole or in part for consideration for any other degree or qualification in this, or any other university. This dissertation is my own work and contains nothing which is the outcome of work done in collaboration with others, except as specified in the text and Acknowledgements.

Kashif Awan
March, 2018
Ottawa, Canada

Abstract

This doctoral dissertation focuses on fabrication processes for integrated photonic devices based on III-V semiconductors. This work covers a range of III-V materials and a variety of devices. Initially, design, fabrication and optical characterization of aluminum gallium arsenide (AlGaAs) waveguides for enhanced optical nonlinear interactions was carried out. Based on our results, we proposed a new type of waveguide for AlGaAs integrated nonlinear optics. Photonic crystal nanocavities and waveguides are attractive components for integrated photonic devices, due to their control over spatial, spectral and dispersion properties of light. Fabrication process for high-Q GaAs photonic crystal nanocavities was developed. Design, fabrication and optical characterization of strip-loaded indium gallium arsenide phosphide (InGaAsP) waveguides were then carried out to demonstrate the potential of Quaternary III-V semiconductors for integrated nonlinear optics. Self-phase modulation and four-wave mixing were demonstrated in InGaAsP waveguides and nonlinear absorption was determined experimentally. Gallium nitride (GaN), due to its wide band-gap, has plethora of photonics and optoelectronics applications. First demonstration of GaN waveguides grown on (-201) β-Ga_2O_3 (gallium oxide) was carried out leading to an experimentally determined propagation loss of 7.5 dB/cm. In summary, this doctoral work presents repeatable and reliable micro and nanofabrication processes for III-V integrated photonic devices.

Acknowledgements

Nanofabrication is challenging as well as time consuming. Working with a variety of materials and devices requires perseverance as well as support; in the form of equipment training, technical discussions and scientific collaborations. I want to acknowledge Norbert Fehr for his assistance in waveguide and wafer design simulations for AlGaAs waveguide project as part of his CO-OP term with our research group while he was an undergraduate student in Nanotechnology Engineering at the University of Waterloo. AlGaAs wafers were grown and partly-funded by CMC Microsystems. AlGaAs waveguide patterning was carried out at INRS (Montreal), and plasma etching was done at CNF (Cornell). I also want to acknowledge David Sanchez for his assistance in AlGaAs optical characterization, as part of his summer internship with our research group. This project was supervised by Prof. Ksenia Dolgaleva.

The project on high-Q gallium arsenide nanocavities was headed by Prof. Antonio Badolato (uOttawa). Nanocavities were designed in collaboration with Prof. Vincenzo Savona (EPFL, Switzeland), and wafer growth was carried out in collaboration with Prof. Ataç İmamoğlu (EHTZ, Switzerland). All of the top-down fabrication was carried out at CNF (Cornell) in collaboration with Prof. Dolgaleva and Prof. Boyd.

InGaAsP wafer and waveguide design simultions were carried out in conjunction with Shayan Saeidi, a M.A.Sc. student of Prof. Ksenia Dolgaleva, and Dr. Lilian Sirbu, a visiting researcher at uOttawa. InGaAsP waveguides were patterned at CNF and etched at QNC (waterloo). Linear Optical characterization of the fabricated InGaAsP waveguides was also carried out in conjunction with Shayan Saeidi, whereas self-phase modulation, four-wave mixing and nonlinear abosorption experiments were carried out by Shayan Saeidi, Spencer Bonca, Payman Rasekh and Alperen Tüğen. This project was initiated and supervised by Prof. Dolgaleva.

Wafers for GaN grown on (-201) β-Ga_2O_3 were obtained from Tamura Corporation and Novel Crystal Technology, Inc. (Japan) by our collaborator Prof. Iman Roqan (KAUST, Saudi Arabia). Mufasila Muhammad, a Ph.D. student of Prof. Iman Roqan measured structural properties of the GaN wafer and also conducted photoluminescence measurements. GaN wavegudies were designed in conjunction with Madhavi Sivan, as part of her CO-OP term with our research group while she was an undergraduate student in Nanotechnology Engineering at the University of Waterloo. Waveguides were fabricated at CNF, and optical propagation losses were measured in conjunction with Spencer Bonca, an undergraduate Chemical Engineering student at uOttawa, as part of his CO-OP term. This project was headed by Prof. Dolgaleva in collaboration with Prof. Roqan.

Slow-light photonic crystal waveguides were designed by Dr. Sebastian Schulz, during his time as a Postdoctoral research in Prof. Robert Boyd's group at uOttawa, currently he is serving as a faculty member at the University of St. Andrews. Device fabrication, optical characterization and data analysis was carried out in conjunction with Dennis Liu (a University of Waterloo undergraduate CO-OP student), Dr. Schulz and Dr. Jeremy Upham (lab manager of Prof. Boyd's quantum photonics group). These slow-light photonic crystal waveguides were later experimentally shown to enhance spectral sensitivity of Mach-Zehnder interferometers, in collaboration with the University of Rochester's group of Prof. Boyd. Both of these silicon slow-light photonic crystal waveguide projects were supervised by Prof. Boyd.

I would like to acknowledge Dr. Sebastian Schulz, Dr. Jeremy Upham, Dr. Mikko J. Huttunen, Dr. Orad Reshef, Dr. Lilian Sirbu and Dr. Daniel Garcia Espinosa from uOttawa, for many useful discussions regarding my research projects. I would also like to acknowledge Anthony Olivieri, CRPuO (uOttawa) nanofabrication cleanroom staff, for many fruitful technical discussions and training on Raith electron beam lithography system. I also want to mention CNF (Cornell) staff members Vince Genova, Dr. Amrita Banerjee, Dr. Alan R. Bleier, Tom Pennell, Aaron Windsor and Jeremy Clark for constant support and helpful discussions during my frequent trips to CNF for device fabrication. I would also like to acknowledge Dr. Nathan Nelson-Fitzpatrick (Staff member at QNC, Waterloo) for valuable discussions regarding indium phosphide etching.

I acknowledge the use of facility and nanofabrication tools at INRS (Montreal), QNC (Waterloo), Carleton University Microfabrication Facility (Ottawa), CNF (Cornell) and CRPuO (uOttawa). I also want to acknowledge Canada Excellence Research Chair (CERC) Doctoral Fellowship, that provided financial support for my graduate studies.

I want to thank my fellow graduate students at Advanced Research Complex (uOttawa), especially graduate students in CERC group, for their companionship and making this a very pleasant and memorable journey for me. I would also like to thank Hugo Begin, Gloria Kaneza, Deniz Akmaner and Dr. Jeremy Upham for their support regarding administrative issues at uOttawa. I am extremely thankful to Prof. Antonio Badolato for his guidance and many fruitful discussions regarding my research projects. I want to thank Prof. Pierre Berini and Prof. Winnie Ye for agreeing to be part of my "comprehensive exam" and "doctoral thesis defense" committees. I am also grateful to Prof. Hanan Anis for agreeing to be part of my doctoral thesis defense committee. I also want to thank Prof. Roberto Morandotti for agreeing to be the external examiner for my doctoral thesis defense. This work would not be possible without constant guidance and support of my supervisors Prof. Ksenia Dolgaleva and Prof. Robert Boyd. I am thankful to both of them for the encouragement and investment of time and research resources in multiple fabrication projects that I undertook. Last but not the least, I extend gratitude to my parents for their love and support, and I am deeply indebted to my wife, Neelam, for her constant support during this time-demanding journey, and for doing more than her fair share in raising our kids.

List of publications

Peer-reviewed journal publications:

1. K. M. Awan, S. A. Schulz, D. X. Liu, K. Dolgaleva, J. Upham, and R. W. Boyd, "Post-process wavelength tuning of silicon photonic crystal slow-light waveguides.," Opt. Lett. 40, 1952–5 (2015).

2. K. Dolgaleva, P. Sarrafi, P. Kultavewuti, K. M. Awan, N. Feher, J. S. Aitchison, L. Qian, M. Volatier, R. Arès, and V. Aimez, "Tuneable four-wave mixing in AlGaAs nanowires," Opt. Express 23, 22477 (2015).
(Carried out simulations of AlGaAs nanowire waveguides for minimizing mode area and performed dispersion engineering of these waveguides.)

3. O. S. Magaña-Loaiza, B. Gao, S. A. Schulz, K. Awan, J. Upham, K. Dolgaleva, and R. W. Boyd, "Enhanced spectral sensitivity of a chip-scale photonic-crystal slow-light interferometer," Opt. Lett. 41, 1431 (2016).
(Was involved in the fabrication and characterization of the slow-light photonic crystal waveguide devices.)

4. S. Saeidi, K. M. Awan, L. Sirbu, and K. Dolgaleva, "Nonlinear photonics on-a-chip in III-V semiconductors: quest for promising material candidates," Appl. Opt. 56, 5532 (2017).
(Worked on the wafer design and waveguide designs.)

5. K. M. Awan, M. M. Muhammad, M. Sivan, S. Bonca, I. S. Roqan, and K. Dolgaleva, "Fabrication and optical characterization of GaN waveguides on (-201)-oriented β-Ga_2O_3," Opt. Mater. Express 8, 88 (2018).

6. S. Saeidi, P. Rasekh, K. M. Awan, A. Tugen, and K. Dolgaleva, "Demonstration of Optical Nonlinearity in InGaAsP/InP Passive Waveguides", under review for Opt. Express (2018)
(Worked on the waveguide designs, carried out the fabrication and setup the experiment for propagation loss measurements.)

7. K. M. Awan, and K. Dolgaleva, "Plasma-heated etching of InP", in-preparation for JVST-B (2018)

Conference proceedings:

1. S. A. Schulz, K. M. Awan, D. X. Liu, K. Dolgaleva, J. Upham, and R. W. Boyd, "Post-Process Tuning of Slow Light Photonic Crystal Waveguides," in Frontiers in Optics 2014 (OSA, 2014), p. FW1B.5.

2. K. M. Awan, N. Feher, R. Boyd, and K. Dolgaleva, "Aluminium gallium arsenide waveguide designs for efficient four-wave mixing," in 2015 Photonics North (IEEE, 2015), pp. 1–1.

3. K. M. Awan, K. Dolgaleva, M. M. Muhammed, and I. S. Roqan, "Epitaxially-grown Gallium Nitride on Gallium Oxide substrate for photon pair generation in visible and telecomm wavelengths," in 2016 Photonics North, PN 2016 (IEEE, 2016), pp. 1–1.

4. S. Saeidi, K. M. Awan, L. Sibru, and K. Dolgaleva, "Semiconductor Compounds for Nonlinear Photonics," in Advanced Photonics 2016 (IPR, NOMA, Sensors, Networks, SPPCom, SOF) (OSA, 2016), Vol. 2016, pp. 3–5.

5. S. Saeidi, K. M. Awan, L. Sirbu, and K. Dolgaleva, "Nonlinear Waveguides Based on III-V Semiconductors," in Frontiers in Optics 2016 (OSA, 2016), p. JTh2A.179.

6. B. Gao, O. S. Magana Loaiza, S. A. Schulz, K. M. Awan, J. Upham, K. Dolgaleva, and R. W. Boyd, "Enhanced Spectral Sensitivity of a Chip-Scale Photonic-Crystal Slow-Light Interferometer," in Frontiers in Optics 2016 (OSA, 2016), p. JW4A.64.

7. S. Saeidi, K. M. Awan, and K. Dolgaleva, "Quaternary III-V semiconductor compounds for integrated nonlinear optics," in 2017 Photonics North (PN) (IEEE, 2017), pp. 1–1.

8. K. M. Awan, K. Dolgaleva, M. M. Muhammed, and I. S. Roqan, "Gallium nitride on gallium oxide substrate for integrated nonlinear optics," in 2017 Photonics North (PN) (IEEE, 2017), pp. 1–1.

Contents

List of Figures

List of Tables

List of Abbreviations

PIC	**P**hotonic **I**ntegrated **C**ircuit
E-beam	**E**lectron beam
CAD	**C**omputer **A**ided **D**esign
ECR	**E**lectron **C**yclotron **R**esonance
RIE	**R**eactive **I**on **E**tching
ICP	**I**nductively **C**oupled **P**lasma
Q	**Q**uality factor
UV	**U**ltra **V**iolet
IR	**I**nfra **R**ed
CMOS	**C**omplementary **M**etal-**O**xide-**S**emiconductor
TPA	**T**wo **P**hoton **A**bsorption
SPM	**S**elf-**P**hase **M**odulation
FWM	**F**our-**w**ave **M**ixing
$\mathbf{A}_{\mathbf{eff}}$	**E**ffective mode **A**rea
TE	**T**ransverse **E**lectric
TM	**T**ransverse **M**agnetic
TEM	**T**ransverse **E**lectromagnetic
GVD	**G**roup **V**elocity **D**ispersion
AOWC	**A**ll-**O**ptical **W**avelength **C**onversion
MBE	**M**olecular-**B**eam **E**pitaxy
PECVD	**P**lasma-**E**nhanced **C**hemical **V**apour **D**eposition
SEM	**S**canning **E**lectron **M**icroscopy
PC	**P**hotonic **C**hrystal
PBG	**P**hotonic **B**and-**G**ap
RI	**R**efractive **I**ndex
PEC	**P**roximity **E**ffect **C**orrection
PSF	**P**oint **S**pread **F**unction
IPA	**I**sopropyl **A**lcohol
MIBK	**M**ethyl **I**sobutyl **K**etone
MOCVD	**M**etal-**O**rganic **C**hemical **V**apour **D**eposition
OPO	**O**ptical **P**arametric **O**scillator
EDFA	**E**rbium-**D**oped **F**iber **A**mplifier
SPCW	**S**ilicon-**P**hotonic **C**rystal **W**aveguides
AFM	**A**tomic **F**orce **M**icroscopy
FTSI	**F**ourier **T**ransform **S**pectral **I**nterferometry
OSA	**O**ptical **S**pectrum **A**nlyzer
MZ	**M**ach-**Z**ehnder
NLT	**N**onlinear **T**ransmission **M**ethod

Dedicated to my parents and my wife.

Chapter 1

Introduction

1.1 Integrated photonics

Photonics, also referred to as optics, is the science and engineering of generation, control and detection of photons for applications; such as manufacturing, medical imaging, next-generation displays, defense technologies, biometric security, biosensing, image processing, lighting, communications, data storage, astronomy, quantum computing and many more [1–10]. Some of these photonic applications have already been commercialized; however, a vast majority still await the big leap from research labs to market, as a commercial product. The biggest hindrance in commercialization of many photonic applications is the cost, complexity and scale of optical components. Integrated photonics can solve these issues, as photonic integrated devices are compact, robust, economical and scalable. Figure 1.1 shows a comparison of the dimensions of a setup on an optical table, against a photonic integrated circuit (PIC) on a chip.

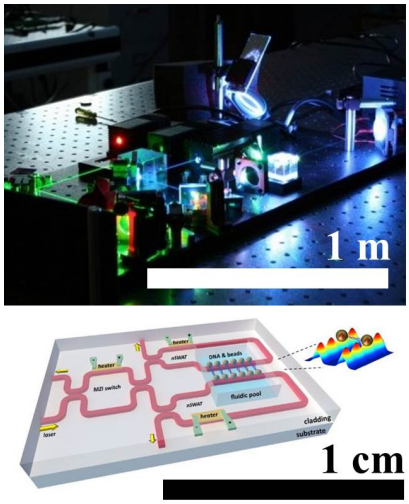

Figure 1.1: Size scale comparison of optical table setup (reproduced from nanohmics Inc.) and a photonic integrated chip (reproduced from M. Soltani, et. al., Nat. Nanotechnol. 9, 448–52 .(2014))

Integrated photonic devices have been demonstrated on a variety of material platforms, such as semiconductors, oxides and polymers [11–16]. However, semiconductors for PIC can be commercialized more readily, due to their compatibility with existing CMOS fabrication processes, to make use of foundries that are already established for mass production of electronic devices. This has stimulated research interest in integrated photonics using silicon, silicon nitride and III-V compound semiconductors (comprising elements from Group III and Group V of the Periodic

Table) such as gallium arsenide (GaAs), aluminum gallium arsenide (AlGaAs), indium phosphide (InP), gallium nitride (GaN), indium gallium arsenide phosphide (InGaAsP) and others [17–20].

A variety of photonic devices have been demonstrated in integrated systems over past few decades, by a large number of academic and industrial research groups engaged in this growing research field. Waveguides, tapers, mode converters, grating couplers, interferometers, ring resonators, photonic crystal waveguides, photonic crystal nanocavities, semiconductor lasers, optical detectors, quantum well-quantum dot emitters, heralded single photon sources, and many more photonic functionalities have been demonstrated in a wide variety of integrated devices based on silicon, silicon nitride, GaAs, InP and others [10, 16, 18, 20–31]. Present work focuses on III-V integrated photonic devices, owing to some of their key advantages over other competing semiconductor materials.

1.2 III-V integrated photonics

1.2.1 Direct band-gap

The electronic band-gap of a semiconductor is either direct or indirect. The lowest energy state in the conduction band and the highest energy state in the valence band are each characterized by a certain crystal momentum (k-vector) in the Brillouin zone [32]. If the k-vectors at conduction band minima and valence band maxima are the same, it is called a direct band-gap, else an indirect band-gap semiconductor. Direct band-gap semiconductors can produce light more efficiently than indirect band-gap, using the process of radiative recombination, where an electron from the conduction band annihilates with a hole in the valence band while radiating excess energy in the form of a photon [32].

Direct band-gap semiconductors support efficient radiative recombination as the electrons near the conduction band minima have a k-vector similar to the holes near the top of the valence band maxima. Having same momentum, the radiative recombination in a direct band-gap semiconductor is a two-body problem. In contrary, this is not the case for indirect band-gap semiconductors, hence for radiative recombination to occur the process must conserve momentum by the absorption or emission of a phonon, where the phonon momentum balances the difference in momentum between the electron and the hole momentum. This makes radiative recombination a three-body problem for indirect band-gap semiconductors, consequently less likely to occur in a given time, hence radiative recombination is far slower in indirect band-gap materials as compared to direct band-gap ones [32]. Applications that require rapid radiative recombination, such as LEDs (light emitting diodes) and laser diodes, are based on direct band-gap semiconductors. Figure 1.2 shows a schematic of a radiative recombination in a direct and indirect band-gap semiconductor.

1.2.2 Material platform for integrated photonics: III-V semiconductors or silicon

III-V semiconductors have multiple advantages over silicon and its compounds as a material of choice for integrated photonics. Being direct band-gap semiconductors, III-V semiconductors lase efficiently as compared to silicon and its compounds, which have indirect band-gap [32]. These materials are compatible with CMOS fabrication, and commercial foundries are already in place for III-V LEDs and laser diodes. Ternary and quaternary III-V semiconductors further allow for control of

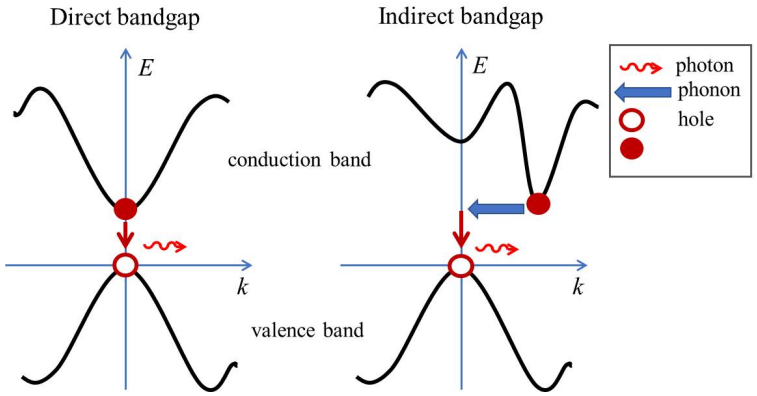

Figure 1.2: Schematic showing radiative recombination in direct and indirect band-gap semiconductors. For conservation of momentum, a phonon is also involved in case of indirect band-gap, resulting in lower probability of radiative recombination.

both band-gap and refractive index by varying material composition [33, 34]. III-V semiconductors can also be used for creating quantum wells and quantum dots, unlike silicon and its compounds. Quantum dots and quantum wells have been shown to have useful applications in optical emitters, solar cells, biosensing, *etc.* [35–37].

1.2.3 III-V integrated photonic devices

III-V semiconductors can be used to have sources, detectors and optical signal processing components, all on a single chip. Such monolithic integration can make mass production of integrated photonic devices a reality [38]. The competing technology is silicon photonics, which still lacks efficient emitters of light, hence currently, silicon photonic integrated chips use a III-V laser that is bonded onto the chip [39]. Such hybrid fabrication scheme is not suited for large scale production, and accuracy of bonding alignment can also reduce product yield.

III-V integrated devices have been used to demonstrate a variety of photonic components such as sources, detectors, modulators, interferometers, resonators, filters, couplers and various nonlinear optical phenomena such as self-phase modulation, second harmonic generation, four-wave mixing *etc.* [21, 34, 40–43]. Due to a large number of different III-V compounds as well as device requirements, a variety of fabrication processes have been used for such devices in literature. This makes III-V fabrication much more challenging than more standardized fabrication processes, such as those used for silicon. In this work a variety of fabrication processes for III-V semiconductor based waveguides and photonic crystals were developed. Repeatable and reliable fabrication processes were established during this doctoral thesis work, that will enable further investigations of linear and nonlinear optical properties of III-V integrated devices.

1.3 Fabrication of integrated III-V photonic devices

In this work, a variety of top-down fabrication processes have been developed. Apart from the growth of the semiconductor wafer, fabrication of III-V integrated photonic devices can be divided in up to three stages. First step is to pattern the semiconductor with the device layout, termed as lithography. Once pattern is ready, next step is to transfer this pattern into the semiconductor, this is accomplished by

etching. If needed, a third and final step of post-processing can be used for reducing etching roughness and/or passivation of top surface.

1.3.1 Electron beam lithography

Optical and electron beam (E-beam) are the most commonly used types of lithography; other less known but experimentally demonstrated lithography techniques include interference lithography, X-ray lithography, nanoimprint lithography and scanning probe lithography. In this work, E-beam lithography is used for initial patterning of all the devices. Both positive and negative E-beam resists have been used in this work. Figure 1.3 shows a schematic of patterning process using positive and negative E-beam resists.

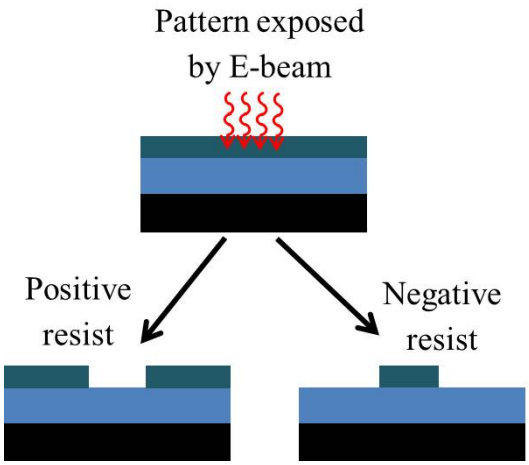

Figure 1.3: Schematic showing the difference between positive and negative E-beam resists. For positive E-beam resist, exposed area is removed, whereas in case of negative E-beam resist, unexposed area is removed.

E-beam lithography simply consists of scanning a beam of electrons over a surface coated with resist film sensitive to electrons, hence depositing energy in the desired pattern, resulting in transfer of the pattern to the resist film. Figure 1.4, reproduced from Thompson *et al.* shows a simplified schematic of an E-beam lithography system [44]. Electrons are generated by thermionic emission and controlled using deflection coils. Whole chamber is under high vacuum, resulting in long mean free path for generated electrons. A computer is used to transfer the pattern data—as defined in the E-beam computer-aided design (CAD)—into the E-Beam resist, by controlling electron beam via deflection coils and the stage using mechanical drive. E-beam lithography systems are capable of very high resolutions with minimum feature size of a few nm, but suffer from low throughput, as it is a sequential patterning process. Whereas photolithography systems have high throughput, but lower resolution and are preferred for commercial production.

Hard mask was required for some devices in this thesis work, hence E-beam was first used to pattern silica, which was subsequently used as the mask to etch pattern into underlying semiconductor. Three different E-beam systems were used in this work, namely, 100 keV Vistec VB6 system at LMN (INRS, Quebec), 100 keV Jeol 9500 system at CNF (Cornell, New York) and 30 keV Raith Pioneer system at CRPuO (University of Ottawa, Ontario). For each fabrication process, first an E-beam recipe was developed: determining spin conditions for E-beam resist, clearing

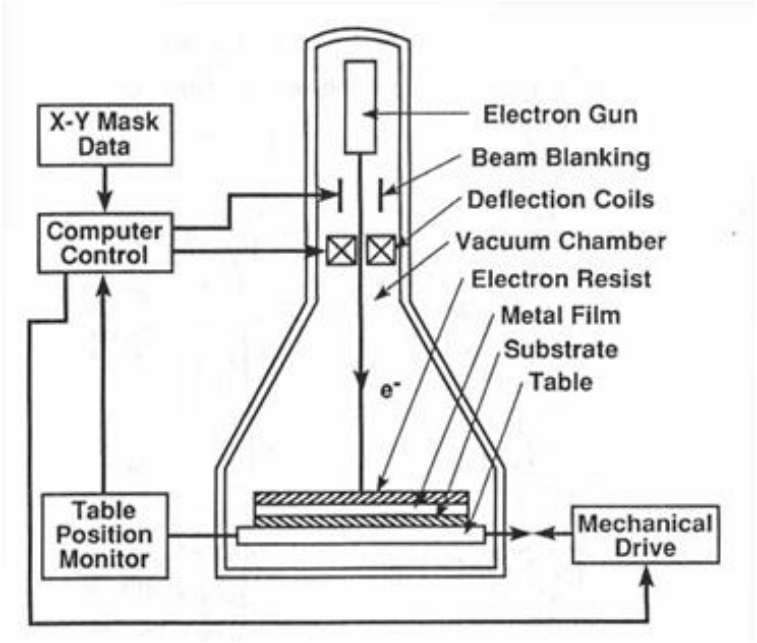

Figure 1.4: Simplified schematic of an E-beam lithography system [44].

dose and proximity effect correction, and development process, followed by creation of E-beam patterning CAD files of the intended pattern.

1.3.2 Etching

Once patterned with E-beam, next step is to transfer this pattern into the underlying semiconductor by etching, a term used for removal of excess material in a top-down fabrication process, so as to end up with the intended device structure. Etching can be divided into wet chemical etching and dry etching. Wet chemical etching is generally isotropic, *i.e.* etches equally in all directions, hence not suitable for structures such as ridges or holes with near-vertical sidewalls. Plasma etching is the most commonly used dry etching process. It can achieve near-vertical etched-facets, and hence was used for all the devices in this work. Figure 1.5 shows the difference between wet-chemical etching and plasma etching.

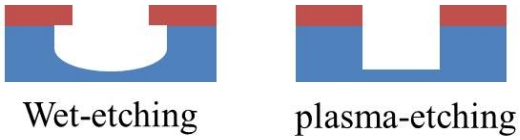

Figure 1.5: Schematic showing wet-etching results in an isotropic etching, whereas plasma etching is more directional, resulting in anisotropic etching.

Plasma Etching

Plasma is defined as the fourth state of matter, similar to a gas. It contains equal number of positive and negative charges; radicals, neutral gas atoms, neutral gas molecules and photons emitted by excited species. Electrons constitute most of the

negative species while positive ions form the positive species in the plasma. The number of electrons is equal to the number of positive ions, hence, plasma is electrically neutral overall [45]. Plasma can be created by applying an external electric field, strong enough to impart enough energy to bounded electrons in the gaseous atoms so that they can break free. These free electrons collide with other gas species resulting in ionization (ions are formed by removing an electron on collision with the atom or molecule), excitation (results in an excited electron within the atom, it then relaxes by emitting a photon) or fragmentation (breakup of gas molecule into radicals or smaller molecules). To give an example of the possible interactions of an electron with different species, Table 1.1 reproduced from Hays *et al.* shows some key reactions within the plasma that comprises of carbon tetrafluoride (also called tetrafluoromethane), oxygen and argon gases [45].

Table 1.1: Key reactions in argon-oxygen-carbon tetrafluoride plasma. Similar reactions happen in plasmas based on a different gas composition [45].

Reaction	Example
Positive ionization	$Ar + e \longrightarrow Ar^+ + 2e$ $O_2 + e \longrightarrow O_2^+ + 2e$
Dissociative ionization	$CF_4 + e \longrightarrow CF_3^+ + F + 2e$
Fragmentation	$CF_3Cl + e \longrightarrow CF_3 + +Cle^-$ $C_2F_6 + e \longrightarrow 2CF_3 + e$
Dissociative attachment	$CF_4 + e \longrightarrow CF_3^+ + F^-$
Dissociative ionization with attachment	$CF_4 + e \longrightarrow CF_3 + +F^- + e$
Excitation	$O_2 + e \longrightarrow O_2^* + +e^-$
Photoemission	$O_2^* \longrightarrow O_2 + h\nu$

O_2^* *is the excited state of* O_2

Etching mechanisms in plasma etching

Plasma etching involves three etching mechanisms: sputtering, chemical etching and ion-enhanced chemical etching. Figure 1.6 is a schematic showing the three mechanisms of etching in a plasma etching process [46, 47]. Sputtering involves only physical etching, *i.e.* material is removed using kinetic energy of ions that bombard material surface. Chemical etching is very similar to wet etching, only difference being the use of gaseous form of reactants, involving radicals of plasma gases used in the etching chemistry. Ion-enhanced chemical etching makes use of both the ion bombardment and the chemical etching by gaseous radicals. Ion bombardment weakens the chemical bonds of the material to be etched, hence enhancing the subsequent chemical etching process [46, 47].

The proportion of physical and chemical etching in a plasma etching process dictates which of the aforementioned etching mechanisms dominate. Sputtering is a highly anisotropic etching process, however, due to ion-bombardment, it results in roughness on the etched surface. Whereas chemical etching is primarily isotropic, but the etched surface is much smoother as compared to sputtering. Ion-enhanced chemical etching offers a middle ground between sputtering and chemical etching, a well-balanced plasma etching recipe will primarily involve ion-enhanced chemical etching, resulting in an anisotropic etching process with bearable etched-surface

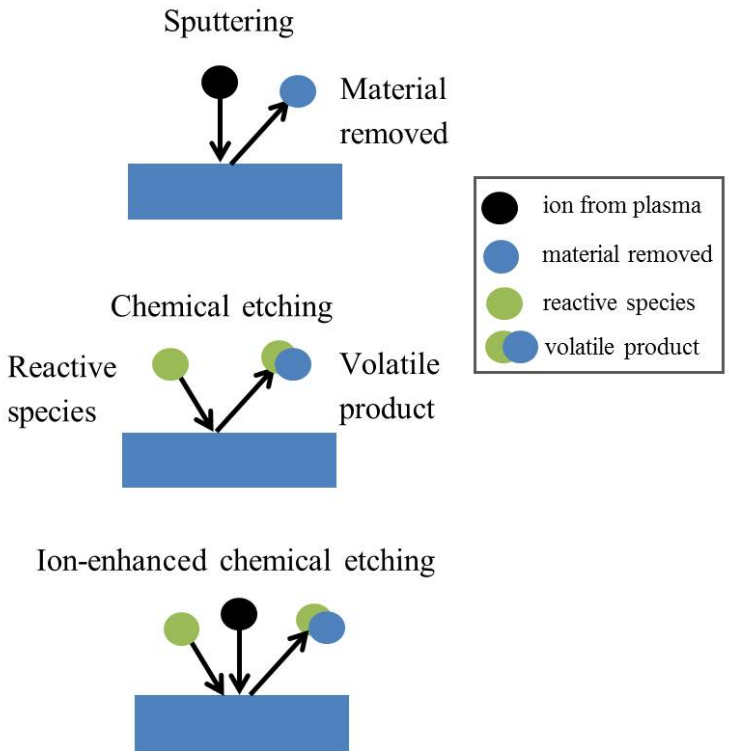

Figure 1.6: Schematic showing etching mechanisms of plasma etching: sputtering, chemical etching and ion-enhanced chemical etching.

roughness. Current work involves systematic plasma etch recipe optimization resulting in balanced etching recipes for AlGaAs, GaAs, GaN and InGaAsP integrated photonic devices.

ICP-RIE system

There are a variety of plasma etching systems, classified based on how plasma is generated and accelerated. In this work, three types of plasma etching systems were used, namely, ECR (Electron cyclotron resonance etcher), RIE (Reactive ion etcher), and ICP-RIE (Inductively Coupled plasma reactive ion etcher). However, ICP-RIE system was the major work horse for etching during the course of the present work.

Figure 1.7 shows a simplified schematic of an ICP-RIE system. Gaseous reactants enter the evacuated chamber through gas inlets on top of the reaction chamber. Plasma is then generated in these gases by a coil driven by an RF source, also called ICP generator. Generated plasma has a characteristic color, that depends on the gas chemistry used for the etching recipe, *e.g.* the oxygen plasma has a pink color whereas the chlorine plasma appears purple. Generated plasma is then accelerated toward the substrate surface to be etched, by a second RF generator, called RIE or Bias generator. Substrate is mounted on an electrode that is helium-cooled for dissipating heat generated by plasma on the substrate.

The availability of two RF sources in an ICP-RIE system, one for plasma generation (ICP generator) and the other to control the bias between plasma and sample (RIE or bias generator), effectively means that one has the luxury of controlling ion density in the plasma independent of the ion energy, since ion energy is controlled by a separate RF source. This makes ICP-RIE very attractive for semiconductor device

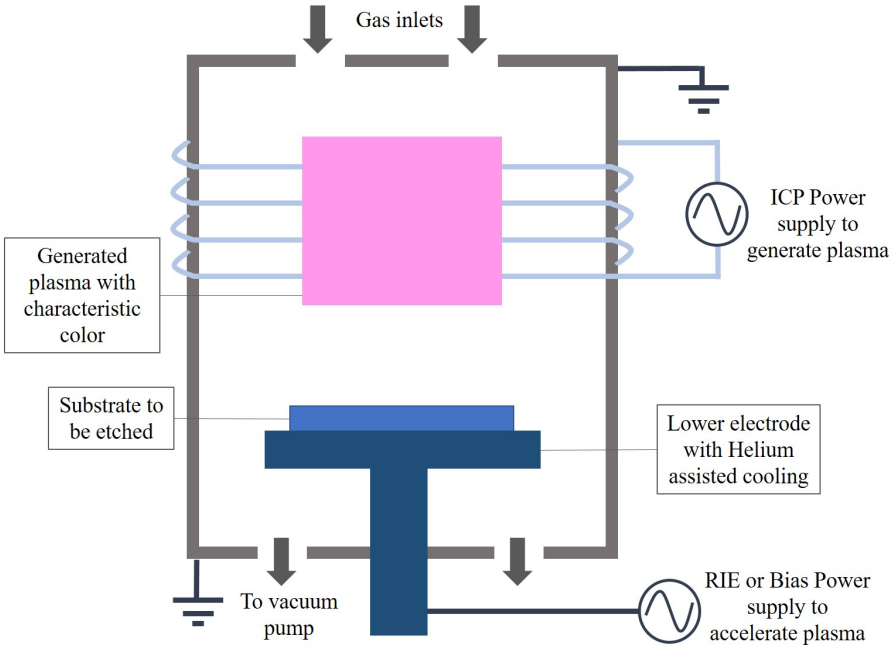

Figure 1.7: Simplified schematic of an ICP-RIE system. Plasma is generated by ICP RF coil using gases in the etching chemistry. Generated plasma is then accelerated toward helium cooled substrate by RIE supply to begin plasma etching.

fabrication as it allows more control over the balance between chemical and physical etching. Hence, ICP-RIE systems were primarily used for most of the device fabrication over the course of the present work.

1.3.3 Post-Processing

Due to physical etching induced by ion bombardment, plasma etching is known to cause damage to semiconductor layer, resulting in higher roughness than wet chemical etching [48]. A few published studies have shown that doing a wet-chemical etching followed by plasma etching can considerably reduce etching roughness, thus leading to better optical quality, and lower propagation losses [46, 48, 49]. Similarly, some III-V semiconductors suffer from stoichiometric imbalance due to higher affinity of some elements from their composition to oxygen, as compared to others. GaAs is one such example: gallium forms oxides more readily than arsenide, so, when it is exposed to the atmosphere, the purity of the crystal lattice is reduced, leading to problems for both passive and active devices [46]. Passivation, another type of post-processing, is employed to avoid such problems [46, 49]. In current work, we have employed low etching rate wet-etching to reduce etching roughness of GaN waveguides.

1.4 Thesis layout

Introductory chapter includes the motivation and background of this work, along with the fundamentals of semiconductor device fabrication. From chapter 2 through chapter 6, details of specific integrated photonic devices with complete description of the fabrication process for each device is covered. Chapter 2 covers the design,

fabrication and characterization of AlGaAs waveguides for enhanced nonlinear optical effects. Chapter 3 is focused on the fabrication of GaAs photonic crystal nanocavities, designed for High-Q (high quality factor) and small mode volume for photon polariton blockade, in collaboration with various research groups.

As a representative of quaternary semiconductors, design, fabrication and optical characterization of InGaAsP waveguides is presented in chapter 4, as a contender for integrated nonlinear optics, specifically for longer wavelengths with applications in spectroscopy. Chapter 5 is focused on the first demonstration of GaN waveguides grown on (-201) β-Ga_2O_3 (gallium oxide), including the details of waveguide design, wafer growth and complete fabrication process. Linear optical characterization results are also included in chapter 5. Optimized design for four-wave mixing is finally presented, as a future direction for this project.

Chapter 6 provides a brief description of projects other than III-V integrated devices, that were undertaken during the course of this doctoral thesis work. These include fabrication of plasmonic devices for nanoantennas, slow-light in photonic crystal waveguides for enhancing spectral sensitivity of an interferometer and post-process wavelength tuning of silicon photonic crystal slow-light waveguides. Chapter 7 provides a brief summary and conclusion, followed by appendix listing journal publications, conference proceedings and conference presentations; resulting from this doctoral thesis work.

Chapter 2

AlGaAs waveguides for enhanced nonlinear optical effects

2.1 Nonlinear optics

Nonlinear optics refers to the interaction of light with matter in the regime where the material response to the applied electromagnetic field is nonlinear in the amplitude of this field. Nonlinear optical phenomena are only measurable at high light intensities, whereas at low light intensities, the properties of materials remain independent of the intensity of the incident light. Due to the requirement of high light intensity, detailed studies of nonlinear optical effects were only possible after the advent of lasers, beginning with the discovery of second-harmonic generation by Franken, *et al.* in 1961. Lasers were used to experimentally study light-matter interaction in a variety of material systems, leading to discovery of various nonlinear optical effects.

2.1.1 Light-matter interaction

Optical nonlinearity arises as a consequence of light-matter interaction. To precisely describe nonlinear optical interactions, let us consider how the dipole moment per unit volume, or polarization $\widetilde{P}(t)$ of a material system, depends on the applied optical field $\widetilde{E}(t)$. In the linear-optics regime, the material polarization depends linearly on the field strength of the incident light. The relationship between the polarization and the incident field strength is given by the equation

$$\widetilde{P}(t) = \epsilon_0 \chi^{(1)} \widetilde{E}(t), \tag{2.1}$$

where $\chi^{(1)}$ is a proportionality constant known as the linear susceptibility, and ϵ_0 is the permittivity of free space. In the nonlinear optical regime, the optical response of a material can be represented as a power series expansion of the polarization $\widetilde{P}(t)$ with the strength of the applied optical field $\widetilde{E}(t)$:

$$\widetilde{P}(t) = \epsilon_0 \left[\chi^{(1)} \widetilde{E}(t) + \chi^{(2)} \widetilde{E}^2(t) + \chi^{(3)} \widetilde{E}^3(t) + \cdots\right]. \tag{2.2}$$

Here $\chi^{(2)}$ and $\chi^{(3)}$ are the second- and third-order nonlinear optical susceptibilities, respectively. So one can express the polarization as a sum of the linear and nonlinear contributions,

$$\widetilde{P}(t) = \widetilde{P}^{(1)} + \widetilde{P}^{(2)}(t) + \widetilde{P}^{(3)}(t) + \cdots, \tag{2.3}$$

where $\widetilde{P}^{(1)}(t)$ represents linear polarization, and all higher-order terms ($\widetilde{P}^{(2)}(t)$, $\widetilde{P}^{(3)}(t)$, *etc.*) are collectively called nonlinear polarization [50].

2.1.2 Nonlinear optical phenomena

A variety of nonlinear optical phenomena have been demonstrated experimentally, such as nonlinear optical absorption, self-phase modulation, second-harmonic generation, third-harmonic generation, cross-phase modulation, four-wave mixing and sum-frequency generation among others.

Second-order nonlinear optical interactions (also called $\chi^{(2)}$ processes) can occur only in noncentrosymmetric materials. Among these phenomena are the sum-frequency generation, difference-frequency generation, optical parametric oscillation and second-harmonic generation. However, third-order nonlinear optical interactions (also called $\chi^{(3)}$ processes) can occur for both centrosymmetric and noncentrosymmetric media. They include Kerr nonlinearities such as self-phase modulation, cross-phase modulation, four-wave mixing and third-harmonic generation [50].

Third-order contribution to the nonlinear polarization is given by the relationship

$$\widetilde{P}^{(3)}(t) = \epsilon_0 \chi^{(3)} \widetilde{E}^3(t). \tag{2.4}$$

If we consider the simple case of monochromatic applied field

$$\widetilde{E}(t) = \mathcal{E} \cos \omega t \tag{2.5}$$

with the constant amplitude $\mathcal{E}$, the third-order polarization can be rewritten in the form

$$\widetilde{P}^{(3)}(t) = \frac{1}{4}\epsilon_0 \mathcal{E}^3 \cos 3\omega t + \frac{3}{4}\epsilon_0 \chi^{(3)} \mathcal{E}^3 \cos \omega t. \tag{2.6}$$

Here we can see two manifestations of the third-order nonlinearity: the first term of equation 2.6 represents third-harmonic generation, whereas the second term represents the nonlinear (intensity-dependent) contribution to the refractive index

$$n = n_0 + n_2 I. \tag{2.7}$$

Here n_2 is the Kerr coefficient, given by [50]

$$n_2 = \frac{3}{2 n_0 \epsilon_0 c} \chi^{(3)}. \tag{2.8}$$

Four-wave mixing and its applications

Four-wave mixing (FWM) is a third-order nonlinear optical effect. It has numerous applications, such as, *e.g.* wavelength conversion, all-optical signal processing and generation of single photons [34, 51, 52]. Figure 2.1 (a) shows the energy diagram for a degenerate four-wave mixing process, where two pump photons are absorbed by the material resulting in the emission of an idler and a signal photon. Figure 2.1 (b) depicts the same process in frequency domain [50].

FWM is a parametric process: it requires the phase-matching condition to be satisfied. Phase-matching condition refers to

$$\Delta k = 0, \tag{2.9}$$

where Δk, for the case of degenerate four-wave mixing [Figure 2.1 (c)], can be defined as

$$\Delta k = 2k_{\text{pump}} - k_{\text{signal}} - k_{\text{idler}}, \tag{2.10}$$

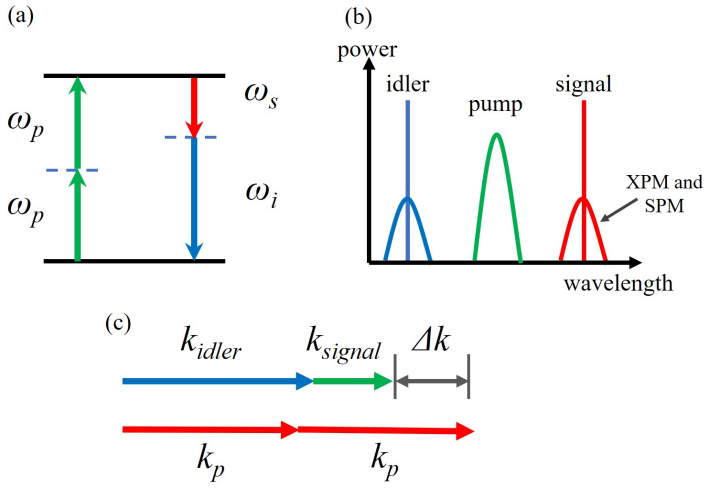

Figure 2.1: (a) Energy level diagram representing degenerate four-wave mixing, (b) Spectral representation of four-wave mixing and (c) phase-matching requirement for four-wave mixing.

where k_{pump}, k_{signal} and k_{idler}, represent the wavevectors of pump, signal and idler, respectively. Substitution of equation 2.9 and wavevectors in above equation results in the phase-matching condition in the form of angular frequencies:

$$2\frac{n_{\text{pump}}\omega_{\text{pump}}}{c} = \frac{n_{\text{signal}}\omega_{\text{signal}}}{c} + \frac{n_{\text{idler}}\omega_{\text{idler}}}{c}. \tag{2.11}$$

Since the energy conservation holds, the phase-matching condition can be rewritten as

$$2n_{\text{pump}} = n_{\text{signal}} + n_{\text{idler}}. \tag{2.12}$$

However, dispersion makes it impossible to achieve a perfect phase matching, since the refractive indices n_{pump}, n_{signal} and n_{idler} for the pump, signal and idler wavelengths, respectively, are different because of material dispersion (for the normal dispersion, the refractive index is an increasing function of frequency). Dispersion can introduce walk-off between the interacting waves at different wavelengths propagating through a medium, due to wavevector mismatch: Δk becomes non-zero. This walk-off reduces the efficiency of the FWM process. For efficient wavelength conversion, Δk has to be as small as possible, ideally zero [50].

Nonlinear parameter γ is the figure of merit for the third-order nonlinearity of a material or device. γ is defined as

$$\gamma = \frac{2\pi n_2}{A_{\text{eff}}\lambda_0}, \tag{2.13}$$

where A_{eff} is the effective mode area of the light propagating in the device and n_2 is the nonlinear refractive index as defined in equation 2.8. It is evident from equation 2.13, that third-order nonlinear optical processes, such as four-wave mixing, will be maximized with high n_2 and a low A_{eff}. Integrated optical waveguides provide the advantage of highly confined optical mode, resulting in low A_{eff}. Such devices are attractive for applications utilizing nonlinear optical processes, such as all-optical wavelength conversion[51] and on-chip spectroscopy. These applications are a major motivation for our research group's work on III-V passive waveguides.

Nonlinear absorption

Optical absorption is the process of absorption of a photon by atoms of the medium, as the radiation propagates through the medium. The medium absorbs energy from photon for inter or intra-band transitions. Thus for absorption to occur, the photon energy must be equal or greater than the energy-gap of such transitions. In the process of nonlinear optical absorption, an atom makes a transition from its ground state to an excited state by the simultaneous absorption of two or more photons [50, 53]. Two- and three-photon absorption processes are based on the simultaneous absorption of two and three photons, respectively, in a single event. Nonlinear absorption has some key applications in fluorescence microscopy and spectroscopy [54–56]. However, nonlinear absorption reduces the efficiency of other nonlinear optical effects such as second-harmonic generation or four-wave mixing, as it results in a loss of the incident optical power. Therefore, both linear and nonlinear absorption should be minimized for increasing the efficiency of a nonlinear optical process, such as FWM.

2.2 AlGaAs waveguides for integrated nonlinear optics

III-V semiconductors hold promise for photonic integration, owing to their direct band-gap and compatibility with CMOS processing. In addition, there is an abundance of different III-V semiconductors with different band-gap wavelengths, ranging from the near-UV (*e.g.*, GaN and related compounds) to the near-IR (InP and related compounds). This enables on-chip light sources operating at different wavelengths, further enhanced by the ternary and quaternary representatives of the class III-V. Ternary and quaternary III-V semiconductors have the advantage of tuning the band-gap wavelength, as well as adjusting the optical properties, such as the refractive index and linear and nonlinear optical susceptibilities, over a range of values [57]. One can grow layers of varying composition, provided that they are lattice matched, such that passive and active integrated optical devices can be fabricated and operated on the same chip (monolithic integration) [33].

Ternary III-V semiconductors are alloys of three elements from the columns III and V of the periodic table, such as, *e.g.*, $Al_xGa_{1-x}As$ and $In_xGa_{1-x}As$. One can change the material composition of the ternary compounds by changing the concentrations of the pairs of elements represented by the composition variables x and $1-x$. This leads to changes in the band-gap wavelength as well as refractive index and other optical properties. Similarly, quaternary III-V semiconductors represent alloys of four III-V elements, such as, *e.g.* $In_xGa_{1-x}As_yP_{1-y}$. Quaternary compositions allow for adjusting simultaneously the band-gap energy and the lattice constant, due to the presence of two independent variables x and y. Vegard's law [58] enables one, to calculate unknown material parameter (the lattice constant or band-gap energy) for a ternary or quaternary material as a function of composition variable(s) x and y, using the corresponding binary alloy data. As an example, for a ternary material $Al_xGa_{1-x}As$, band-gap energy $E_{Al_xGa_{1-x}As}$ can be interpolated as

$$E_{Al_xGa_{1-x}As}(x) = xE_{AlAs} + (1-x)E_{GaAs}, \tag{2.14}$$

where E_{AlAs} and E_{GaAs} are the corresponding parameters of the binary compounds AlAs (aluminum arsenide) and GaAs (gallium arsenide) [33, 59]. Quaternary semiconductors are discussed further in Chapter 4, where we present our work on $In_xGa_{1-x}As_yP_{1-y}$ waveguides.

AlGaAs waveguides have shown promise for applications in all-optical wavelength conversion and all-optical signal processing [34, 51, 60]. Being a semiconductor, AlGaAs is compatible with CMOS processing, hence, AlGaAs based integrated optical devices can be scaled to accommodate for commercial volumes. Low propagation optical losses and tailorable band-gap make it attractive for integrated nonlinear optics. Aluminum galium arsenide (AlGaAs) is a ternary semiconductor compound where the concentrations of aluminum (Al) and galium (Ga) can be adjusted based on the formula $Al_xGa_{1-x}As$, such that they make 100% together (*e.g.*, GaAs has 100% of Ga, while $Al_{0.5}Ga_{0.5}As$ corresponds to 50% of Ga and 50% of Al). Different $Al_xGa_{1-x}As$ compositions result in ternary compounds with different optical properties as the composition affects the value of the energy gap. By a proper selection of the material composition, it is possible to shift the energy gap in AlGaAs in such a way that two-photon absorption (TPA) can be made negligible for the wavelength range centered around 1550 nm (the Telecom C-band wavelengths). It has been shown in earlier studies [61] that the specific composition that allows one to achieve this corresponds to $Al_{0.18}Ga_{0.82}As$.

2.2.1 Optical waveguides

Conduits of dielectric medium surrounded by media with lower refractive indices form optical waveguides. The underlying principle for optical waveguides is total internal reflection. One can distinguish between waveguide structures with one-dimensional and two-dimensional confinement of light. Waveguide structures with one-dimensional confinement are called planar waveguides, these are slabs of dielectric conduits sandwiched between two cladding layers, as shown in Figure 2.2. The diagram shows the propagation of light in a symmetric slab dielectric waveguide using ray-optics representation. For the total internal reflection at the interfaces between the core and claddings to occur, it is necessary that the refractive indices of the core (n_2) and the claddings (n_1) satisfy $n_2 > n_1$. Then the light is transported in the inner medium with the higher refractive index (commonly referred to as, the core or the guiding layer), without escaping into the claddings. The slab dielectric waveguide is called "symmetric" in case when the upper and lower claddings are made of the same material and, consecutively, have equal refractive indices. Light traverses waveguides in the form of optical modes, that maintain same transverse distribution and polarization at all locations along the symmetric waveguide, due to the self-consistency condition which requires that the wave reproduces itself after

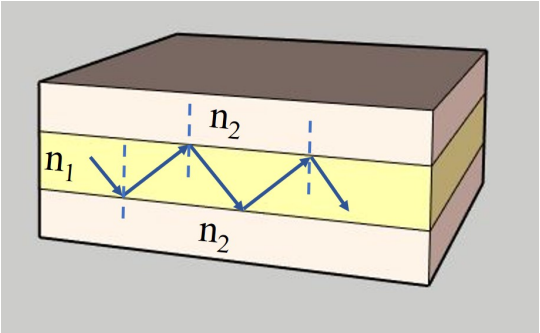

Figure 2.2: Schematic of a symmetric slab dielectric waveguide depicting a guided mode bounded due to total internal reflection at the boundary between the core and claddings with the refractive indices n_2 and n_1, respectively.

two consecutive reflections at the core-cladding interfaces. Fields that satisfy this condition are solution of Maxwell's equations that satisfy all the boundary conditions, and called eigenmodes (in short, modes) of the optical waveguide [9].

Waveguide modes are discrete with respect to the values of the propagation constants and the angles that the ray makes with respect to the propagation direction. If a waveguide's dimensions are relatively small with respect to a specific wavelength, single-mode operation can be achieved, that allows only for the fundamental modes to be supported by the waveguide. These modes can be further classified on the basis of the dominant polarization component into Transverse Electric (TE), Transverse Magnetic (TM), and Transverse electromagnetic (TEM) modes. TE modes have the electric field perpendicular to the direction of propagation, with a small component of the magnetic field in the direction of the propagation. Similarly, for TM modes, the magnetic field is perpendicular to the direction of propagation with a small component of the electric field in the direction of the propagation. In the case of TEM modes, both the electric and the magnetic field are perpendicular to the direction of propagation [9].

Dielectric Optical waveguides can be classified into planar and channel waveguides. Planar (also called slab) waveguides only confine light in the y-axis, while channel waveguides confine light in the direction of both x and y axes, where z-axis is the direction of propagation. Figure 2.2 shows schematic of a dielectric slab waveguide, and figure 2.3 shows schematics of commonly used channel waveguides, namely strip-loaded, strip, rib and embedded-strip waveguides [9].

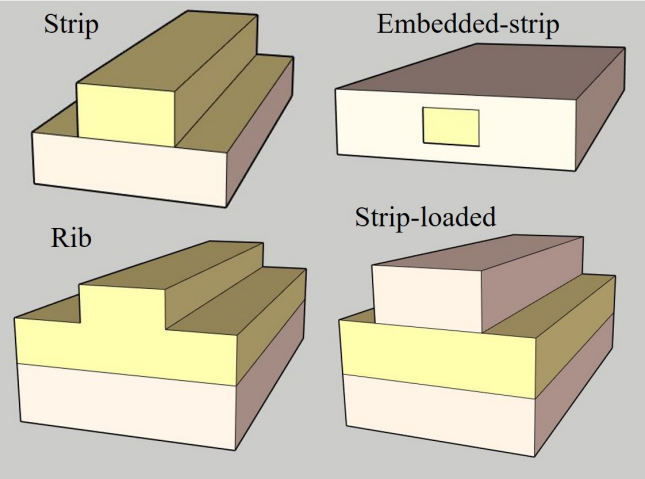

Figure 2.3: Schematic showing commonly used types of channel waveguides. Strip, embedded-strip, rib and strip-loaded waveguides are shown where guiding layer is indicated with yellow color.

2.2.2 Group velocity dispersion in waveguides

Group velocity dispersion (GVD) is responsible for the temporal walk-off between the interacting wavelengths that co-propagate through a medium. The larger the spectral difference between the interacting wavelengths, the shorter the distance they travel together in the nonlinear medium before getting separated in time. Hence, for any parametric nonlinear optical process, the nonlinear conversion efficiency is reduced due to GVD. Mathematically, GVD is defined as the second derivative of

the propagation constant β with respect to the angular frequency:

$$\beta_2 = \frac{d^2\beta}{d\omega^2}. \tag{2.15}$$

Dispersion in an optical waveguide is composed of two contributions, namely: the material dispersion and the waveguide dispersion. Material dispersion and the corresponding parameters describing this contribution (the dispersion coefficient D and GVD) are pre-defined and fixed for a specific material. Waveguide dispersion, arising from the difference in the propagation constants of the guided wave in the core and claddings, can be adjusted and even engineered through the design of the waveguide geometry. If the waveguide core dimensions are larger than the wavelength, the propagating mode interacts primarily with the core material and experiences insignificant waveguide dispersion. The overall dispersion experienced by the guided modes in such structures is primarily material [51].

When the dimensions of an optical waveguide are smaller than the wavelength of light propagating through it, the mode penetrates significantly deeper with its evanescent tails into the medium surrounding the guiding layer, hence the guided mode "sees" both the core and a considerable portion of the cladding, making the waveguide dispersion in such structures significant. In extreme cases, where the surrounding medium has the refractive index significantly different from that of the guiding layer (*i.e.*, high index contrast, for example, in the case of the air and semiconductor material), the waveguide dispersion could compensate (or even overcompensate) for the material dispersion [34]. In the range of values where GVD is approaching zero, the walk-off is minimized, and larger wavelength separation between the interacting waves is possible. This is necessary for widely tunable parametric nonlinear optical interactions, such as tunable four-wave mixing.

2.2.3 Designing III-V channel waveguides

The first step in designing III-V waveguides is to identify the composition of the guiding layer. As mentioned earlier, we will be using $Al_{0.18}Ga_{0.82}As$ as the core of our waveguides, to nullify two-photon absorption at 1.55 μm. Next, the composition of the cladding layers is to be selected, while keeping in mind the requirement that it must have a lower refractive index than the core layer, and must be lattice-matched for low-defect growth of the stack. The lattice mismatch between different layers of a semiconductor structure could result in a poor-quality epitaxial growth, leading to high defect density and, subsequently, low optical quality. Figure 2.4, reproduced from Bett, *et al.* [62], shows a plot of lattice constant as a function of band-gap energy, for various III-V binary compounds. Lattice is well-matched if the constituent binary compounds, for a ternary compound, lie on a nearly vertical line on this plot. This is true for AlAs and GaAs, hence, the two have good lattice matching for all compositions, *i.e.*, for all values of x from 0 to 1, inclusive. Similarly, a lattice-matched substrate is then selected. For AlGaAs, the semiconductor industry standard substrate is GaAs; hence, was selected as the substrate for our wafer designs.

Once the wafer stack composition is fixed, the 2D waveguides can then be designed, based on the design criteria. In this work, all the waveguide designs were performed using eigenmode solver of *Lumerical Mode Solutions*, a commercial photonics design software. The waveguide dimensions are then further optimized—as per the design criteria—by varying thickness of the stack layers, as well as the width and etching depth of the waveguide. This is discussed further in subsequent sections for each type of AlGaAs waveguides.

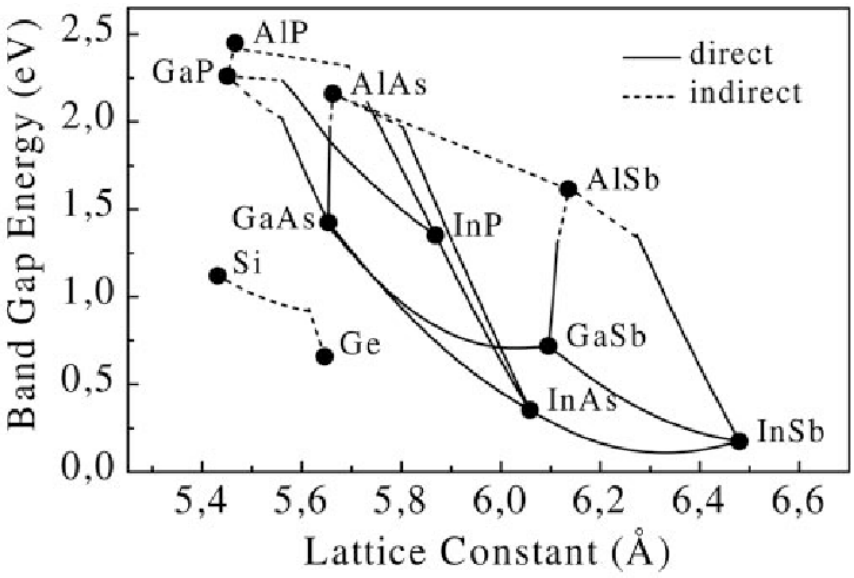

Figure 2.4: Plot of crystal lattice constant as a function of band-gap energy for commonly used binary III-V semiconductors, reproduced from Bett, *et al.* [62].

2.2.4 Strip-loaded and nanowire AlGaAs waveguides for nonlinear optics

All-optical wavelength conversion (AOWC) can be an important tool for all-optical signal processing, which can lead to a realization of higher bandwidth links in optical networks. AlGaAs waveguides can make AOWC achievable through nonlinear optical phenomena such as, *e.g.*, FWM. A comprehensive study on FWM in AlGaAs strip-loaded waveguides has been performed by Dolgaleva, *et al.* [51]. The characteristic feature of strip-loaded waveguides is a relatively low refractive index contrast, resulting in weakly guided modes that propagate in the core region, fully buried underneath the upper cladding. The etching depth in such structures does not extend beyond the interface between the upper cladding and the core. The guided modes thus reside in the material and do not "see" much of surface roughness acquired through the dry etching process. As the result, the propagation loss in strip-loaded waveguides is relatively low, around 1 dB/cm in AlGaAs waveguides [51]. At the same time, the relatively weak mode confinement results in relatively large values of the effective mode area A_{eff} (see equation 2.16), around $4 - 6\ \mu\text{m}^2$, which leads to a relatively low efficiency of the nonlinear optical processes in such structures. Since there is no dispersion engineering in these structures, the material dispersion is the dominant dispersion mechanism, making such waveguides suitable for FWM over a small range of wavelengths. FWM in AlGaAs strip-loaded waveguides has been demonstrated over a spectral range of 40 nm at most [51].

A more sophisticated nanofabrication procedure with an optimized dry etching process enables more quality-sensitive waveguides with ultra compact dimensions, namely, AlGaAs nanowires. These structures have a much higher refractive index contrast as the required etching depth extends beyond the guiding layer into the lower cladding, and the sidewalls of the guiding channel appear to be exposed to the air. The resulting effective mode area are very small, $A_{\text{eff}} < 1\ \mu\text{m}^2$, leading to higher efficiency of nonlinear optical interactions. At the same time, such structures

can be dispersion-engineered to have zero-dispersion crossing point in the wavelength range of interest, *e.g.*, around 1550 nm, leading to a much wider FWM frequency conversion range. However, such devices exhibit much higher propagation losses, as the guided mode is largely exposed to the fabrication induced sidewall roughness. A variety of nonlinear optical effects have been demonstrated in AlGaAs nanowires [34, 63, 64]. The demonstrated FWM tunability range was close to 100 nm, however reported propagation losses were greater than 1 dB/mm [34].

2.2.5 Proposed compromise: Half-core waveguides

In present work, we propose a new type of AlGaAs waveguide, as a compromise between strip-loaded and nanowire waveguides, such that it has advantage of either waveguides *i.e.* small effective modal area and reasonable propagation loss. This proposed design has the core half-etched, inspiring us to coin the term half-core waveguide for this structure. Having half of the core exposed to the air leads to a relatively strong mode confinement and, at the same time, relatively low propagation loss. Figure 2.5 shows the schematics of the three waveguide structures: strip-loaded, nanowire and the proposed compromise, the half-core waveguides. The figure also schematically shows the location of the guided mode in all three structures. To experimentally investigate our hypothesis, optimized waveguides were designed for each type of AlGaAs waveguide, fabricated and characterized, as detailed in the subsequent sections of this chapter.

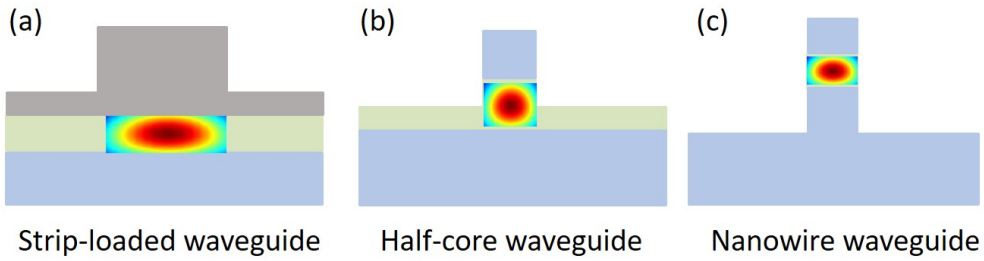

Figure 2.5: Schematic of strip-loaded, half-core and nanowire waveguides, with their corresponding mode location.

2.3 Optimized AlGaAs waveguide designs

For an experimental comparison of the three types of AlGaAs waveguides, design optimization was performed for each waveguide, targeting enhanced nonlinear optical interactions. Wafer composition, layer thickness, waveguide width and height is parametrized for each type of waveguides. These parameters are then optimized as per the design criteria, listed in next section. *Lumerical Mode Solutions* was used to simulate the waveguide modes; the resulting Electromagnetic field distribution for eigenmodes was used for computing the effective mode area A_{eff} for the fundamental modes. The expression for the effective mode area, provided by Lumerical, is

$$A_{\text{eff}} = \frac{\left[\int_{-\infty}^{\infty}\int_{-\infty}^{\infty} |E(x,y)|^2 \,\mathrm{d}x\,\mathrm{d}y\right]^2}{\int_{-\infty}^{\infty}\int_{-\infty}^{\infty} |E(x,y)|^4 \,\mathrm{d}x\,\mathrm{d}y}; \tag{2.16}$$

it matches the definition of the effective mode area for the third-order nonlinear optical interactions, given in [51]. We have also extracted the values of the GVD (β_2) and the dispersion parameter D, given as

$$D = -\frac{2\pi c}{\lambda^2}\beta_2. \tag{2.17}$$

2.3.1 Design criteria

The design criteria used for the design optimization of the three types of AlGaAs waveguides are as listed below:

- *Lattice matching and two-photon absorption:* As discussed earlier, we need to select a semiconductor composition for the waveguide fabrication in such a way that it has all its layers lattice-matched to the substrate. The composition of the guiding layer is already fixed as $Al_{0.18}Ga_{0.82}As$, so as to have the photon energy at 1.55 μm smaller than one-half of the band-gap energy.
- *Single-mode operation:* As per equation 2.13, the nonlinear coefficient can be maximized by minimizing the effective mode area. The effective mode area is minimum for the fundamental mode. Furthermore, multimode waveguides can reduce efficiency of the nonlinear conversion process, if portion of the incident optical power is coupled to higher modes. Hence, the designed waveguides have to be single-mode, supporting the fundamental TE and/or TM modes only.
- *Enhancing optical intensity by minimizing A_{eff}:* Apart from using fundamental mode, one can also increase the refractive index contrast between the epitaxial layers of the wafer to further reduce A_{eff}, by picking up the compositions of the core and claddings (within the range of values allowed by lattice matching and band-gap energy requirements). Furthermore, one can design the waveguide geometry in a way that the effective mode area is as small as possible for a given refractive index contrast, hence maximizing the intensity and enhancing nonlinear optical interactions.
- *Cut-off wavelength:* Since these AlGaAs waveguides are designed for four-wave mixing, having a broad operation wavelength range can provide suitable conditions for broadly tunable FWM. These waveguides are designed to have wavelength cut-off around 2 μm. Hence these waveguides can be used for FWM wavelength conversion from 1.55 μm to 2 μm without suffering from two-photon absorption.
- *Dispersion management:* FWM is a parametric process; hence, in order to achieve a broad wavelength tuning range, one needs to make sure that the dispersion is low and positive in the wavelength range of interest. That is why, fitting the zero-dispersion point within this range would be beneficial. Dispersion engineering is employed in the cases where high refractive index contrast is available to achieve zero GVD. This is possible to implement only in the nanowire waveguide geometry.

2.3.2 Optimized strip-loaded waveguide

The strip-loaded waveguide was parametrized, as shown in figure 2.6, for the optimization simulations. The core concentration of aluminum remained at 18%, while

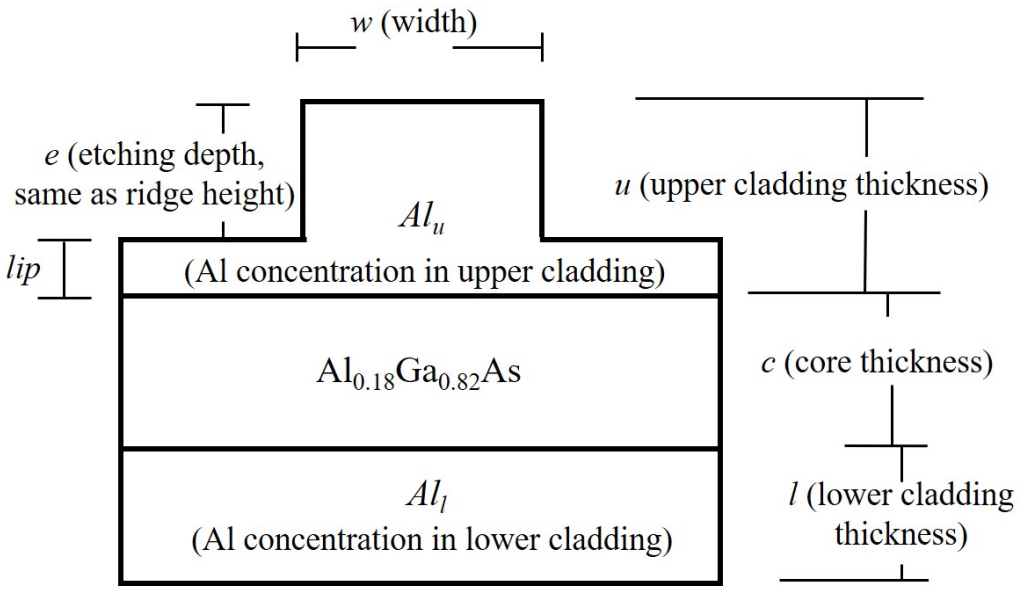

Figure 2.6: Schematic of parametrized strip-loaded waveguide, showing the waveguide variables that can be altered for optimizing the design.

the aluminum content in the upper and the lower claddings must be greater than that in the core and less than or equal to 70%. Figure 2.7 shows the change in the refractive index of AlGaAs with the variation of the aluminum concentration between 0 and 100% (x = 0 to 1 on the graph) for the wavelength 1.55 μm at room temperature. It can be seen that, as aluminum concentration increases, the refractive

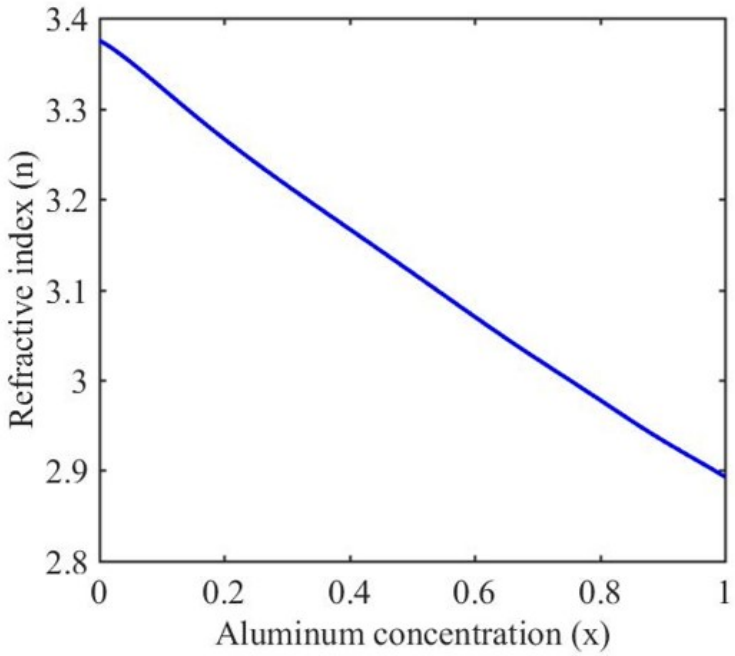

Figure 2.7: Plot of refractive index as a function of aluminum concentration for $Al_xGa_{1-x}As$ at 1.55 μm at room temperature.

index decreases. Hence, using AlAs will give the highest refractive index contrast

(between core and cladding layers) and the best mode confinement; however, aluminum is known to oxidize readily when its concentration in AlGaAs exceeds 70%. To be on the safe side, we kept the maximum aluminum concentration in our design at 65%. The material dispersion model for AlGaAs at various Al concentrations and temperatures was adapted from experimental data reported by Gehrsitz, *et al.* [65]. The effect of the waveguide variables (shown in Figure 2.6) on the mode area is understood by sweeping one variable at a time and keeping other parameters fixed. Simulations were carried out to optimize the waveguide design by minimizing A_{eff} while maintaining single-mode operation for the operating wavelength range.

The optimization of strip-loaded AlGaAs waveguides began with looking at the effect of the size of the *lip*, which is the thickness of the upper cladding that is not etched away, as shown in figure 2.6. All other variables were kept constant, while the lip size was varied. The effect of the lip size on A_{eff} can be seen in figure 2.8, which shows that a decrease in the lip size results in a decrease of the mode area. However, etching the upper cladding completely is expected to result in an increase

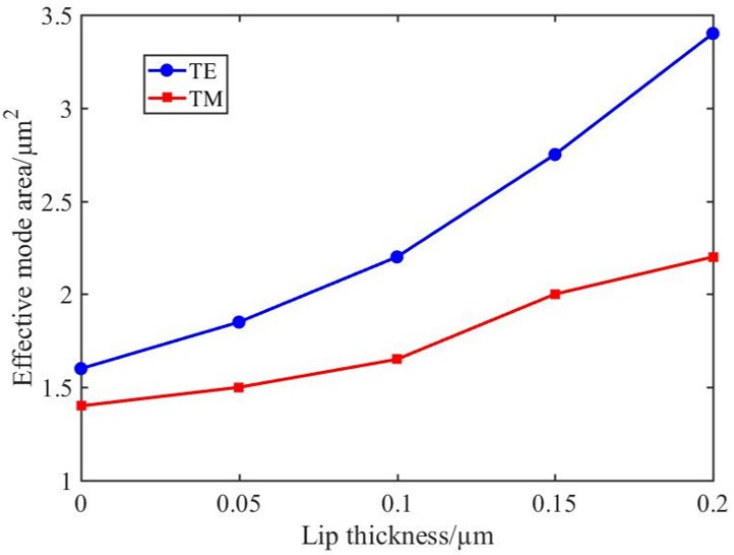

Figure 2.8: Plot of A_{eff} as a function of the *lip* size with all other variables kept constant, as listed in table 2.1.

of the propagation loss in the waveguide, therefore, a practically achievable lip size of 100 nm was chosen while keeping in mind that well-controlled etching will be required to fabricate this design, since there is no etch-stop—a material layer that is chemically inert to the etching recipe, *e.g.*, silica in case of silicon-on-silica wafers acts as the etch-stop layer—in this case. The values used for variables, other than lip size are listed in table 2.1.

The next critical parameter that is required to be minimized is the core thickness. Intuitively, the smaller the waveguide core, the more confined the mode is, resulting in low A_{eff}. However, to be able to achieve the minimum possible core thickness without the loss of guidance, the refractive index contrast between the core and claddings should be maximized. We were restricted to 400 nm core thickness because any smaller core thickness results in mode cut-off for 2 μm wavelength. Hence, the core thickness was fixed at 400 nm for the rest of the parameter optimization.

The effect of the variation of the lower cladding thickness l on A_{eff} of the strip-loaded waveguide was then simulated, the results are shown in figure 2.9 (a); the

Table 2.1: Waveguide variable definitions and values, used for optimizing lip size, as shown in figure 2.8.

Waveguide parameter	value
u (Thickness of upper cladding)	0.7 μm
c (Thickness of core)	0.5 μm
l (Thickness of lower cladding)	4 μm
w (Waveguide width)	1.6 μm
lip (Unetched part of upper cladding)	varied
e (Waveguide etching depth)	varied, as lip is varied: $e = u - lip$
Al_l (Aluminum concentration of lower cladding)	65 %
Al_u (Aluminum concentration of upper cladding)	50 %

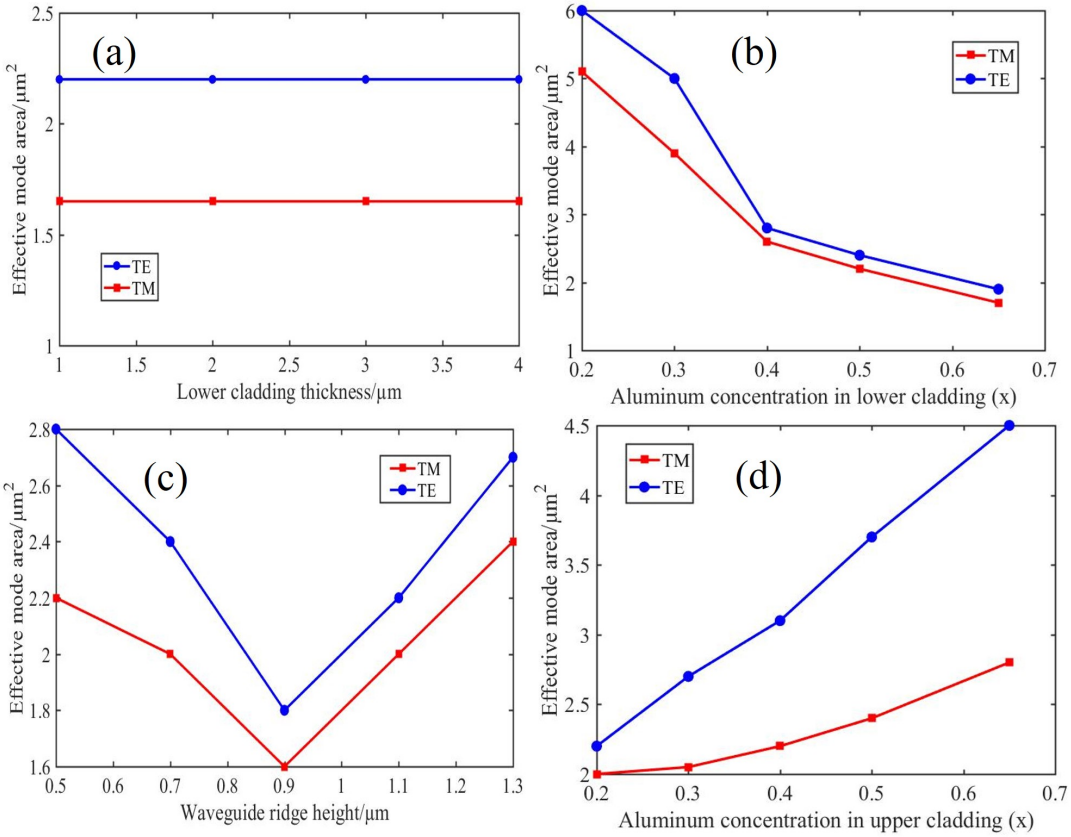

Figure 2.9: Strip-loaded waveguide optimization. (a) A_{eff} as a function of the lower cladding thickness. The values of other variables are fixed as follows: $u = 0.7$ μm, $c = 0.4$ μm, $lip = 0.1$ μm, $w = 1.6$ μm, $Al_u = 50\%$ and $Al_l = 65\%$. (b) A_{eff} as a function of aluminum concentration in the lower cladding. The values of other variables are fixed as $u = 0.7$ μm, $c = 0.4$ μm, $l = 4.0$ μm, $lip = 0.1$ μm, $w = 1.6$ μm and $Al_u = 50\%$. (c) A_{eff} as a function of the ridge height, where $ridge = u - lip$, and the values of other variables fixed as $c = 0.4$ μm, $l = 4.0$ μm, $lip = 0.1$ μm, $w = 1.6$ μm, $Al_l = 65\%$ and $Al_u = 50\%$. (d) A_{eff} as a function of aluminum concentration in the upper cladding; the values of other variables are fixed: $u = 1.0$ μm, $c = 0.4$ μm, $l = 4.0$ μm, $lip = 0.1$ μm, $w = 1.6$ μm and $Al_l = 65\%$.

figure caption specifies the parameters used for other variables while l was varied. It was clearly observed that the lower cladding thickness had no effect on the mode area; however, the lower cladding thickness was fixed at 3 μm to ensure sufficient thickness for the guided mode not to leak into the underlying GaAs substrate, which has higher refractive index than the waveguide core layer. Similarly, the effect of the aluminum concentration in the lower cladding Al_l can be observed in figure 2.9 (b). It proves that the concentration of aluminum in the lower cladding has a dramatic effect on the mode area of the waveguide. Therefore, the lower cladding must be fabricated with the largest aluminum concentration. However, it is known that aluminum readily oxidizes; hence, a maximum possible value of 65% was fixed for the lower cladding of the strip-loaded waveguide.

To determine the right thickness for the upper cladding, we fixed the lip size at the optimal value of 100 nm. As a result, the variations of the thickness of the upper cladding were translated into the variations of the height of the ridge. The plot in figure 2.9 (c) shows the effect of varying the ridge height (equal to $u + lip$) on A_{eff}. An optimal value of around 900 nm was found, leading to $u = 1$ μm.

Figure 2.9 (d) shows the impact of Al_u (the aluminum concentration in the upper cladding) on A_{eff}. It is clear from the data that the aluminum concentration in the upper cladding must be minimized in order to provide the smallest effective mode area. However, it must be noted that as Al_u is reduced to values closer to the aluminum concentration of the core layer, *i.e.* 18%, the mode starts shifting more into the upper cladding. So in this case, minimum A_{eff}, is not the only criteria for the selection of a suitable value for Al_u. An Al_u value that results in low A_{eff}, while keeping the mode confined in the core layer, was to be selected. It was found that the mode stays within the guiding layer for Al_u higher than 30%, resulting in sufficient refractive index contrast between the upper cladding and the guiding layer to contain the mode within the latter. Based on the simulations, the desired aluminum concentration in the upper cladding (for the core thickness 400 nm) was 35%.

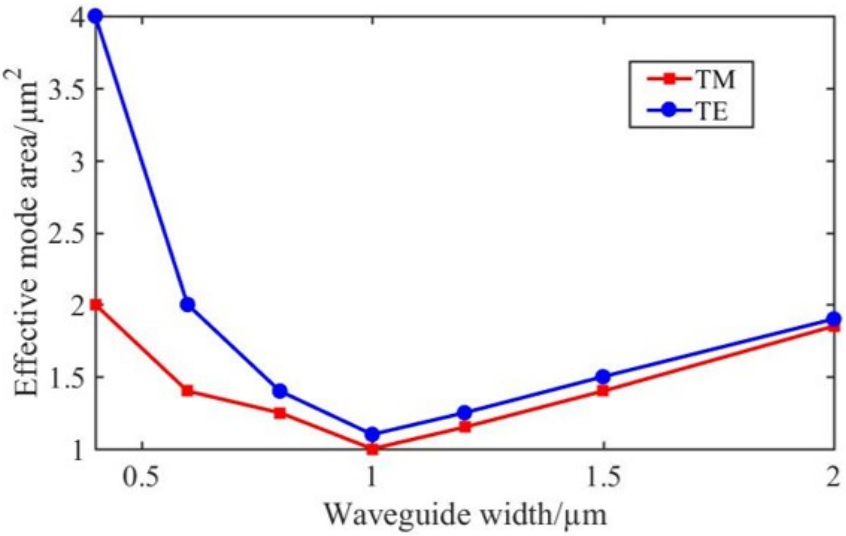

Figure 2.10: A_{eff} of strip-loaded waveguide as a function of the waveguide width, with other variables fixed at their optimal values, as shown in figure 2.11.

We investigated the effect of the waveguide width on the effective mode area while all other waveguide parameters were fixed at their optimum values. The result is shown in figure 2.10. It can be seen from the plot that the effective mode area for

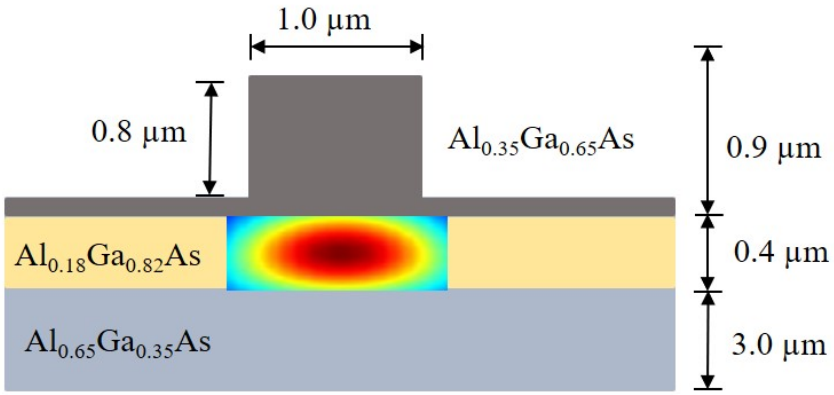

Figure 2.11: Optimized waveguide parameters for the strip-loaded AlGaAs waveguide.

both fundamental TM and TE modes reaches its minimum for the waveguide width around 1 μm. Figure 2.11 shows the schematic of an optimized strip-loaded AlGaAs waveguide. The simulated intensity distribution for the fundamental TE and TM modes of the optimized strip-loaded waveguide at 1.55 μm and 2.0 μm are shown in Figure 2.12. As mentioned earlier, in the design criteria, that we want to have

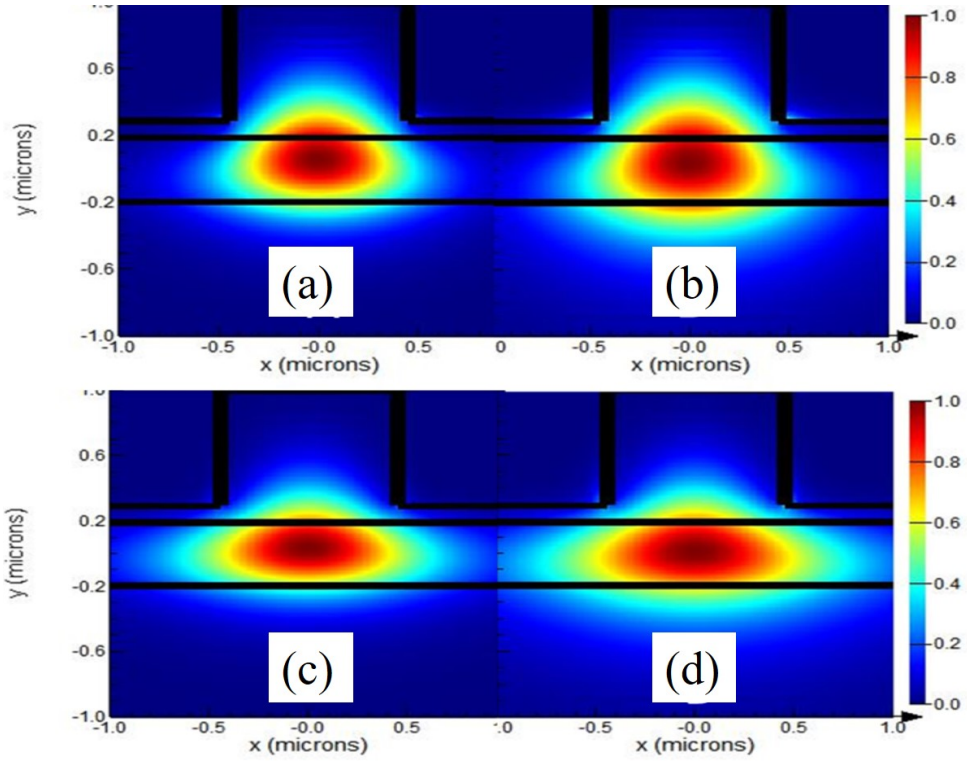

Figure 2.12: Simulated intensity distribution for the optimized strip-loaded waveguide: (a) TM mode at 1.55 μm wavelength, (b) TM mode at 1.55 μm wavelength, (c) TM mode at 2.0 μm wavelength and (d) TM mode at 2.0 μm wavelength.

wide spectral tunability for our passive devices, hence, even though the design is aimed for 1.55 μm, but we make sure that the cut-off wavelength is over 2.0 μm. The designed waveguide had an effective mode area of around 1.1 μm^2 for both TE and TM modes at a wavelength of 1.55 μm.

2.3.3 Optimized AlGaAs nanowires

Nanowire waveguides have ultracompact dimensions, which is only achievable by etching deep into the lower cladding and exposing the core sidewalls to the surrounding medium with a much lower refractive index (*e.g.*, the air). Thus, we have fixed the aluminum concentration in the core and both claddings at 18% and 65%, respectively, to create the maximum practically achievable refractive index contrast, leading to a strong mode confinement. Figure 2.13 shows the variable parameters for the nanowire waveguide, namely: c (core thickness), u (upper cladding thickness), l (lower cladding thickness), e (etching depth into lower cladding, i.e., how much thickness of the lower cladding is etched away) and w (width of the waveguide).

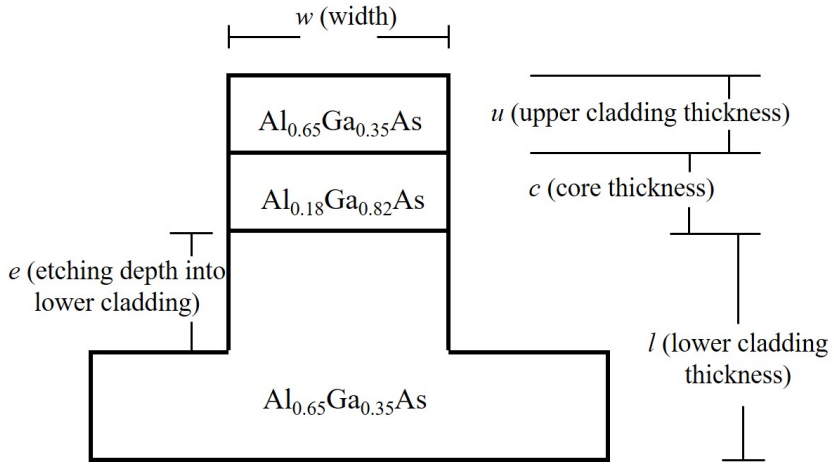

Figure 2.13: Schematic of parametrized AlGaAs nanowire waveguide, showing the waveguide variables that can be optimized in the design.

The core thickness is an important design parameter of nanowire waveguide. The effect of the core thickness variation on A_{eff} was investigated while keeping other waveguide parameters fixed. The results are shown in figure 2.14 (a) where the caption has the details of the values of the fixed parameters. The trend suggests that the best mode confinement is achieved for the core thickness lying between 500 and 700 nm. Similarly, the effect of the variation in the upper cladding thickness has been investigated while other parameters were fixed. The result is displayed in figure 2.14 (b) where A_{eff} is plotted as a function of the upper cladding thickness. It can be seen from the plot that as upper cladding thickness is reduced, the A_{eff} seems to decrease as well. This is expected, since, as we approach the case with no upper cladding ($u = 0$), we have a higher refractive index contrast, as the top of the guiding layer is exposed to air. However, for our design, we require an upper cladding to have a symmetrical mode, this facilitates coupling light into these compact waveguides. This mode symmetry can be achieved by having similar refractive index contrast of the guiding layer with upper and lower claddings. We chose a value of 0.4 μm as a suitable number for our design, as it provides the mode symmetry and is also practical from the fabrication point of view, since deep plasma etching is known to be very challenging.

The effect of the etching depth (into the lower cladding) on A_{eff} was then simulated, as shown in figure 2.14 (c). It can be observed that an increase in the etching depth reduces A_{eff}; however, the effect saturates around 0.8 μm, and 0.4 μm etching depth can result in good confinement, while, at the same time, can be achievable

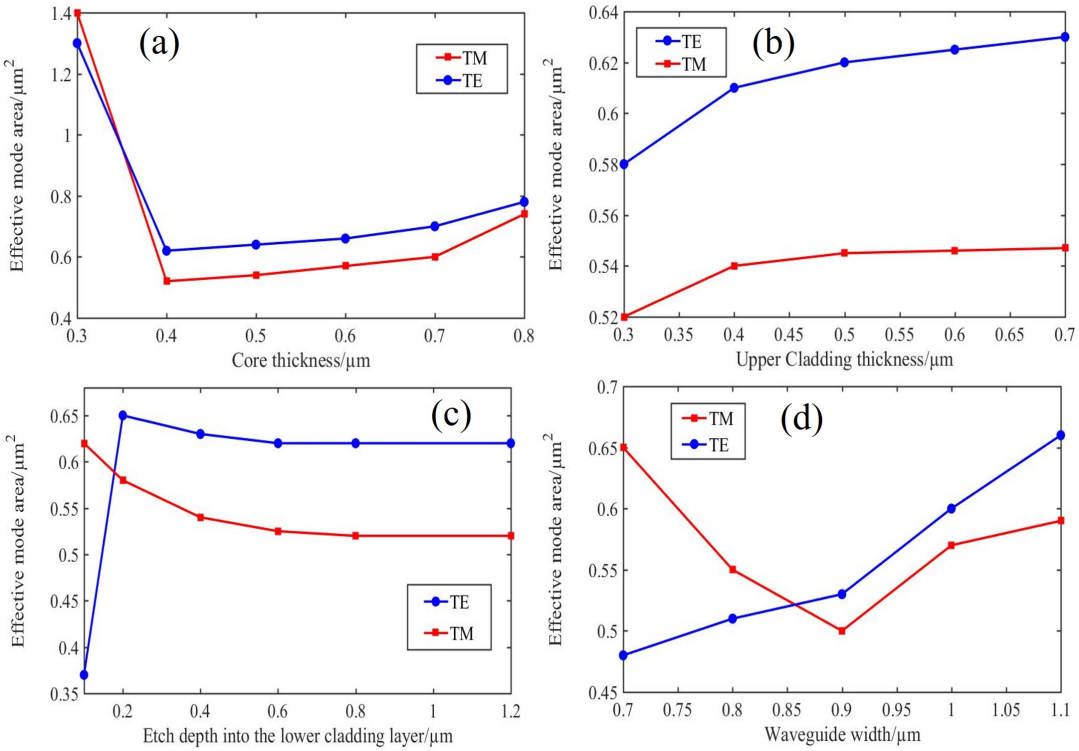

Figure 2.14: Nanowire waveguide optimization: (a) Plot of A_{eff} as a function of core thickness, values of other variables fixed as: $u = 0.8\ \mu$m, $l = 4.0\ \mu$m, $e = 0.5\ \mu$m, $w = 1.0\ \mu$m, (b) Plot of A_{eff} as a function of thickness of the upper cladding, values of other variables fixed as: $e = 0.5\ \mu$m, $c = 0.6\ \mu$m, $l = 4.0\ \mu$m, $w = 1.0\ \mu$m, (c) Plot of A_{eff} as a function of etching depth into the lower cladding, values of other variables fixed as: $c = 0.6\ \mu$m, $l = 4\ \mu$m, $u = 0.4\ \mu$m, $w = 1.0\ \mu$m, (d) Plot of A_{eff} as a function of the waveguide width, values of other variables fixed as: $u = 0.4\ \mu$m, $c = 0.6\ \mu$m, $l = 4.0\ \mu$m, $e = 0.4\ \mu$m.

from the fabrication standpoint (the deeper the etching depth, the more challenging it is to achieve it). So, an overall etching depth (from the top of the wafer to where the etching ends) of 1.4 μm was selected for the final design.

Lastly, the effect of the waveguide width on A_{eff} was simulated, and is shown in Figure 2.14 (d). The waveguide width of 0.9 μm provides the lowest value of A_{eff}, while still maintaining the guidance for the wavelengths up to 2 μm. Figure 2.15 shows the schematic of the optimized AlGaAs nanowire waveguide. The simulated intensity distribution for the fundamental TE and TM modes of the optimized nanowire waveguide are shown in Figure 2.16 for a fixed wavelength 1.55 μm. The waveguide has an effective mode area of around 0.5 μm^2 for both the fundamental TE and TM modes at the wavelength of 1.55 μm.

2.3.4 Optimized half-core waveguide

The half-core waveguide can provide a good mode confinement while exhibiting low propagation losses. In this structure, we etch through half of the core layer thickness. This improves the mode confinement (as compared to the strip-loaded waveguide), whereas the area where the mode is exposed to fabrication-induced roughness (on the etched facet) is smaller than that of the nanowire waveguide. The

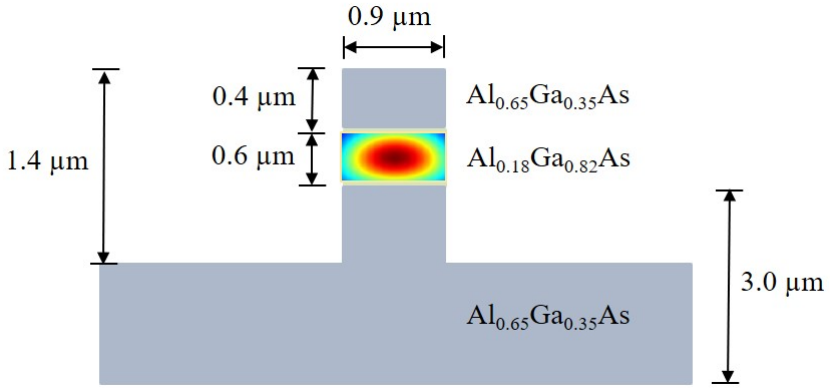

Figure 2.15: Optimized waveguide parameters for AlGaAs nanowire.

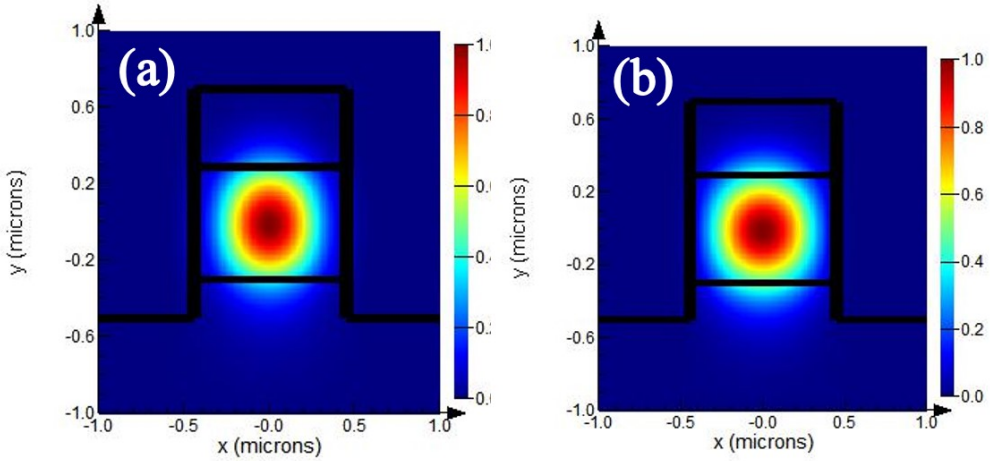

Figure 2.16: Simulated intensity distribution for the optimized nanowire modes at a wavelength of 1.55 μm: (a) TE and (b) TM.

aluminum concentrations in the core and claddings are selected to be 18% and 65%, respectively, to ensure the maximum refractive index contrast and, hence, a stronger mode confinement. Figure 2.17 shows the variables for the half-core waveguide design, namely: c (core thickness), u (upper cladding thickness), l (lower cladding thickness), e (etching depth into core, i.e. how much thickness of the core-layer is etched away) and w (width of the waveguide).

To observe the effect of the upper cladding thickness on A_{eff} of the half-core waveguide, simulations were performed where all other waveguide parameters were fixed, as shown in figure 2.18 (a) and specified in the figure's caption. It can be observed from the results that a smaller value of the upper cladding thickness leads to lower values of A_{eff}, however, for the reasons mentioned above for nanowire waveguide design, we selected an upper cladding thickness of 0.4 μm.

The effect of the core thickness variation on A_{eff}, while other parameters fixed (as specified in the figure caption), is shown in figure 2.18 (b). It can be concluded from the graph that a core thickness of 0.6 μm is the optimum: it was observed that for the core thickness smaller than 0.6 μm the waveguide cannot maintain guidance for wavelengths up to 2 μm, while for the core thickness larger than 0.6 μm, A_{eff} demonstrates a rapid expansion.

As stated earlier, the etching depth was kept constant at half of the thickness of the core layer. However, we performed an analysis to quantify the effect of the

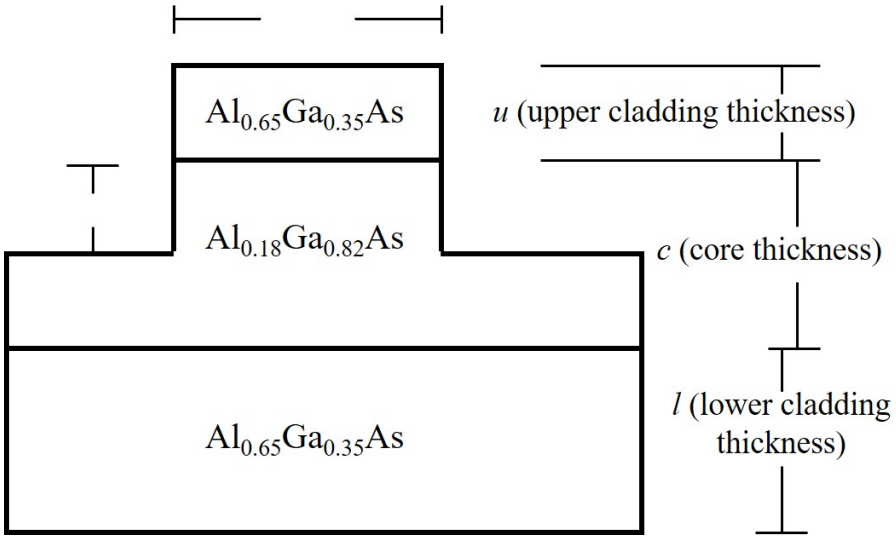

Figure 2.17: Schematic of parametrized AlGaAs half-core waveguide, showing the waveguide variables that can be optimized.

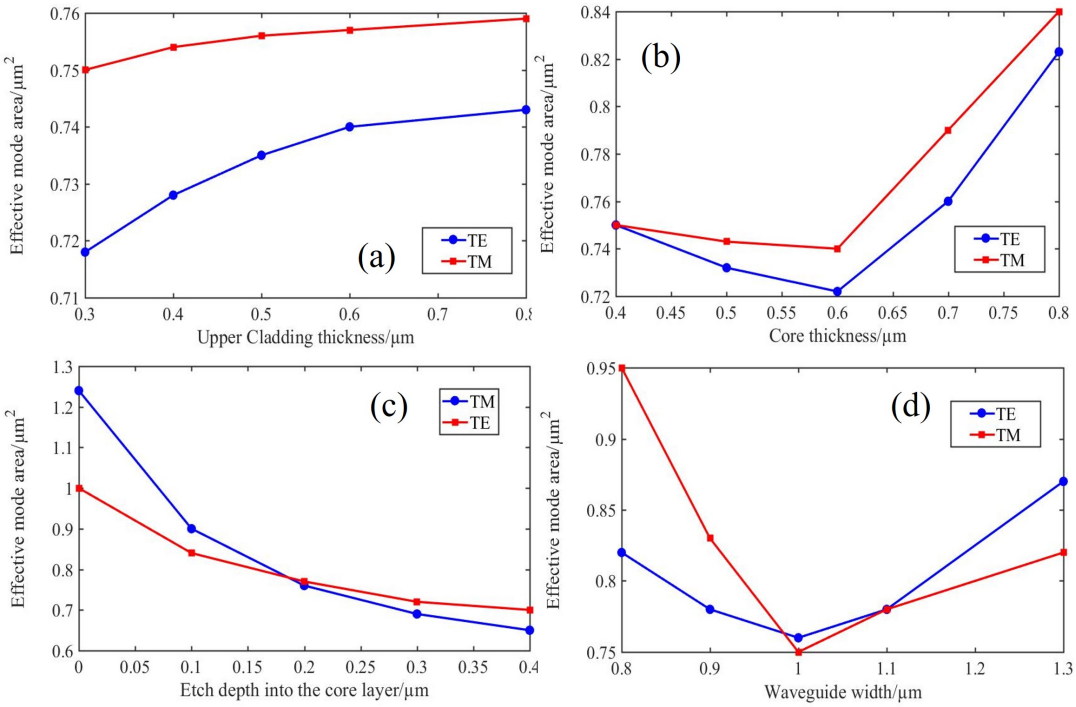

Figure 2.18: Half-core waveguide optimization: (a) Plot of A_{eff} as a function of the thickness of upper cladding, values of other variables fixed as: $e = 0.25\ \mu$m, $c = 0.5\ \mu$m, $l = 4.0\ \mu$m , $w = 1.0\ \mu$m, (b) Plot of A_{eff} as a function of the core thickness, values of other variables fixed as: $u = 0.4\ \mu$m, $l = 4\ \mu$m, $e = (c/2)\ \mu$m, $w = 1.0\ \mu$m, (c) Plot of A_{eff} as a function of the etching depth into core layer, values of other variables fixed as: $c = 0.6\ \mu$m, $l = 4.0\ \mu$m, $u = 0.4\ \mu$m, $w = 1.0\ \mu$m, (d) Plot of A_{eff} as a function of the waveguide width, values of other variables fixed as: $u = 0.4\ \mu$m, $c = 0.6\ \mu$m,$l = 4.0\ \mu$m, $e = 0.3\ \mu$m.

etching depth on A_{eff}. In these simulations, the etching depth into the core was varied while other parameters were kept constant. The result is shown in figure 2.18 (c), and the values of the fixed parameters are given in the figure caption. It can be

seen that, with increasing etching depth, A_{eff} decreases. But to minimize the effect of the sidewall roughness, we choose the etching depth to be fixed half-way through the core layer.

Finally, the effect of the waveguide width on A_{eff} was studied, and the results are presented in figure 2.18 (d). The optimum waveguide width for minimizing A_{eff} was found to be 1.0 μm. Figure 2.19 shows the schematic of the optimized half-core AlGaAs waveguide design. The simulated intensity distribution for the

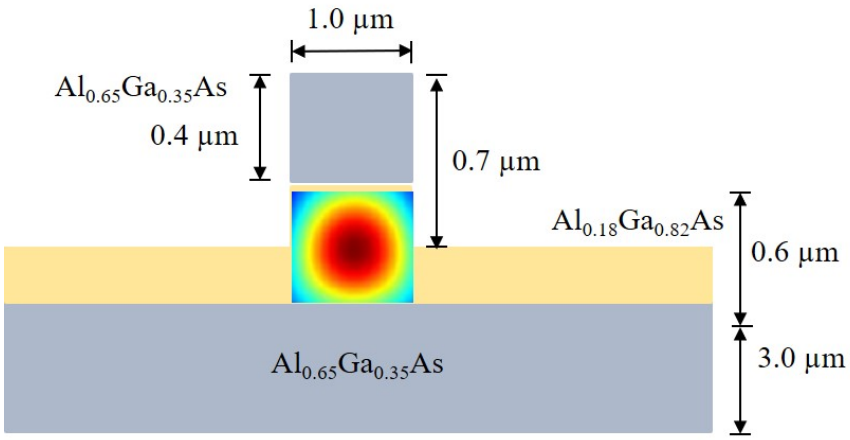

Figure 2.19: Optimized waveguide parameters for AlGaAs half-core waveguide.

fundamental TE and TM modes of the optimized half-core waveguide at 1.55 μm are shown in Figure 2.20. The waveguide has an effective mode area of around 0.75 μm^2

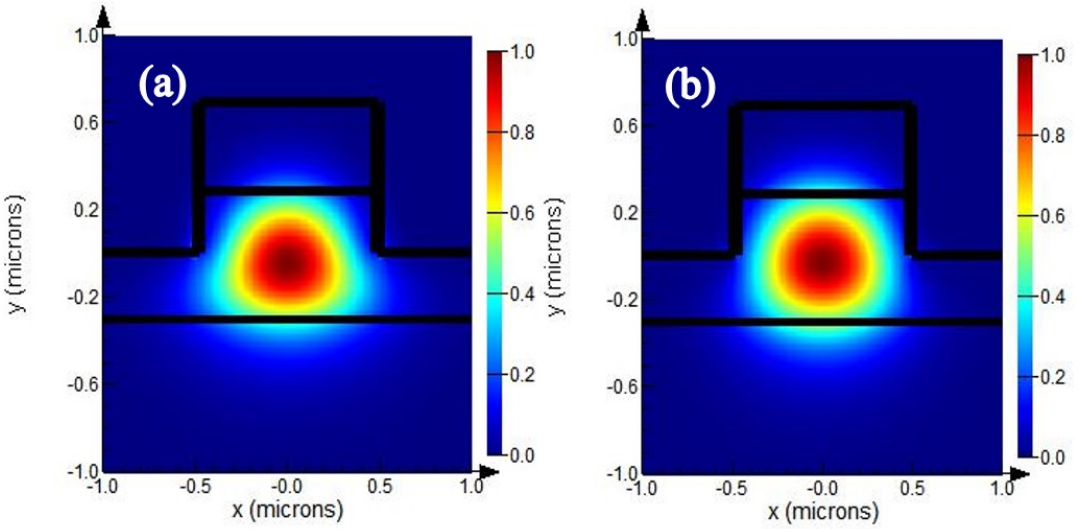

Figure 2.20: Simulated intensity distribution for optimized half-core waveguide modes at a wavelength of 1.55 μm: (a) TE and (b) TM.

for both TE and TM modes at the wavelength of 1.55 μm. Clearly, these numbers are much smaller than those for the strip-loaded waveguide, which has the mode area of 1.3 μm^2, and are slightly larger than those of the nanowires. It is thus expected that such a waveguide geometry (half-core) can act as a compromise between the strip-loaded and the nanowire waveguides.

2.3.5 Dispersion characteristics of the optimized waveguides

In order to compare the dispersion characteristics of the three waveguide designs, we performed the frequency sweep, and calculated the dispersion parameter D, defined in equation 2.17. We only provide a summary of the dispersion analysis for the sake of conciseness as this thesis has a broader scope than FWM optimization. Figure 2.21 shows the dispersion coefficient as a function of the wavelength for each optimized waveguide design. As discussed earlier, dispersion engineering is only

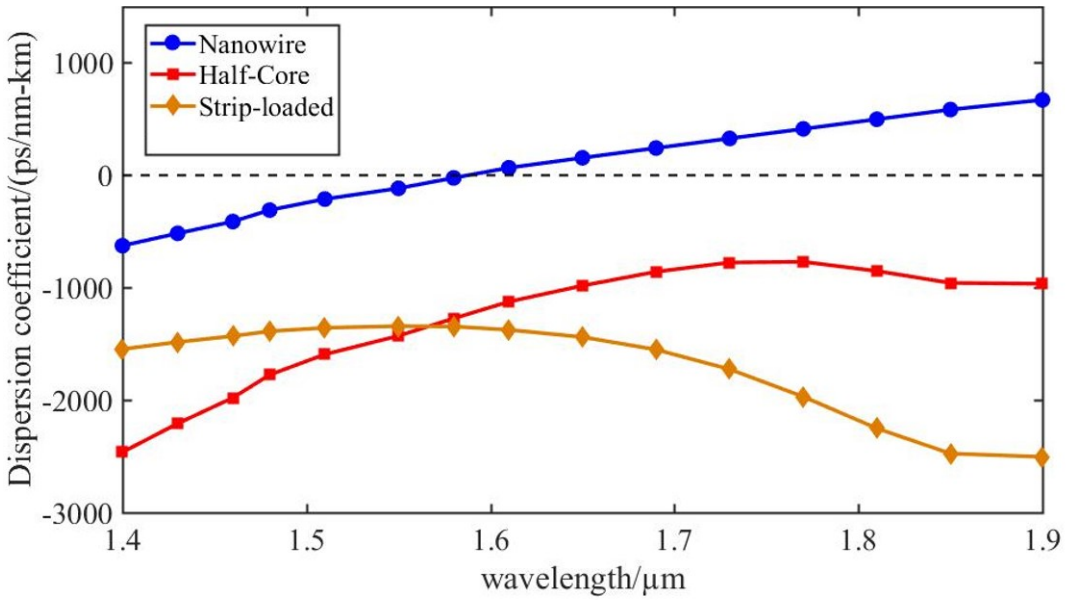

Figure 2.21: Dispersion plots for optimized strip-loaded, nanowire and half-core waveguides. Zero-crossing visible for nanowire waveguide.

possible in nanowire waveguides, leading to a design that has zero dispersion. The half-core waveguide had slightly lower dispersion values compared to those of the strip-loaded waveguide. However, zero-dispersion could not be achieved in either half-core or strip-loaded waveguides.

2.4 Fabrication of AlGaAs waveguides

Fabrication of the optimized designs of the three types of AlGaAs waveguides was then carried out. As a first step, the growth of the designed wafer stacks was performed. Half-core and nanowire waveguides had the same layer stack design, so a single wafer was grown for the two. To avoid oxidation of AlGaAs, a 0.1 μm-thick GaAs capping layer was added at the top of both half-core and strip-loaded wafer stacks, it was also verified by simulations, that addition of this thin layer does not affect the design of the waveguides. The stacks were grown on GaAs substrate, that is lattice-matched to AlGaAs epitaxial layers. Figure 2.22 shows the wafer designs for the strip-loaded and the half-core (same as nanowire) waveguides.

The design and the project proposal was submitted to CMC microsystems' academic design competition, and a partial funding was secured for epitaxial growth of these wafers, after a peer-reviewed proposal approval. These wafers were grown by CMC microsystems, using molecular beam epitaxy (MBE) in a custom V80 system containing a valved cracker source for Arsenic vapor (As_2) and conventional

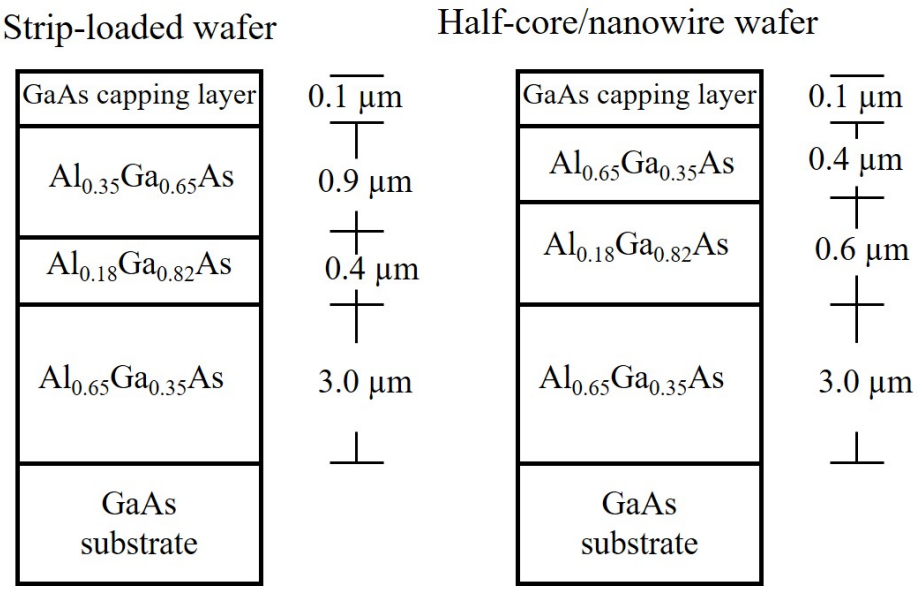

Figure 2.22: Wafer design for strip-loaded waveguide and half-core waveguide (same wafer used for nanowire waveguides)

effusion cells for the group-III elements (aluminum and gallium). The growths were performed on 76 mm-diameter, single-side polished semi-insulating GaAs (100) substrates with a 2° miscut towards the 110-direction.

2.4.1 Fabrication process

We fabricated the designed waveguide structures using standard electron beam lithography followed by dry etching. The steps of the fabrication process are outlined in Figure 2.23. The epitaxially grown AlGaAs wafer was first cleaved into 15 mm x 15 mm chips. Each chip was then cleaned with acetone and isopropanol, and then was blow-dried with nitrogen gas. After that, 200 nm thick layer of Silica (SiO_2) was deposited on top of the wafer by Plasma-Enhanced Chemical Vapor Deposition (PECVD) technique, and then 50 nm of chromium was deposited by sputtering. Following these steps, a 350 nm thick layer of negative-tone E-beam resist maN-2403 was spin coated at a spinning speed of 4000 rpm and ramp of 300 rps, for 1 min, followed by a pre-bake at 90 °C for 1 min. The waveguides were then patterned into maN-2403, using a 100-kV VB6 electron beam lithography system with a dose of 210 $\mu C/cm^2$. In order to make sure that the fabricated structures have the dimensions as per the design, we left some room for fabrication tolerance and errors by defining the waveguides with a range of different values for the waveguide width, for each design, *e.g.*, for strip-loaded waveguides, we patterned waveguides with the widths ranging from 0.7 to 1.1 μm, with an increment of 0.1 μm.

After the E-beam patterning, the E-beam resist was developed in Ma-D 525 developer (from *micro resist technology*) for 40 seconds, then rinsed in de-ionized water. The E-beam-patterned maN-2403 mask was then used to transfer the waveguide pattern into chromium by ICP-RIE. A Trion ICP-RIE system was used for etching the chromium layer with an existing optimized recipe, with the following parameters: 20 sccm of chlorine and 10 sccm of oxygen at the pressure of 10 mT, with the ICP and RIE powers of 500 and 120 W, respectively . The chromium mask was then used

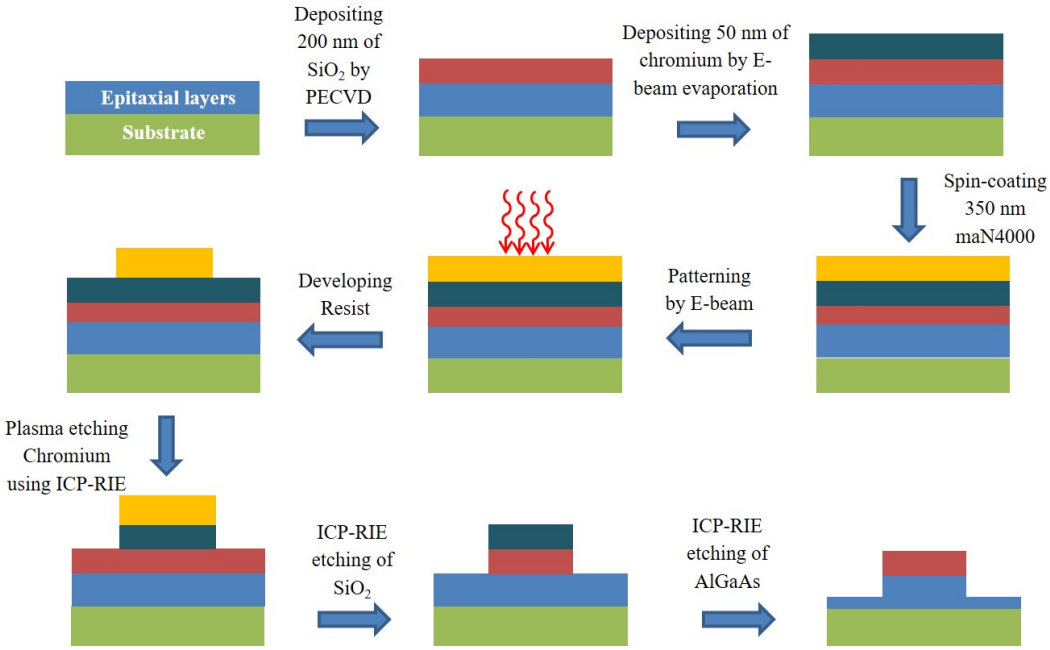

Figure 2.23: Schematic representation of the fabrication process. The PECVD deposition of a 200 nm thick layer of SiO_2 on top of the AlGaAs wafer was followed by the sputtering of a 50 nm thick layer of chromium. After that, a 350-nm-thick layer of maN-2403 was spin-coated and patterned by E-beam lithography. The maN-2403 mask was then used to imprint the waveguide profile into the chromium layer, and the patterned chromium layer was subsequently used as the mask for etching the SiO_2 layer. AlGaAs was finally etched using the SiO_2 mask, with an optimized etching recipe.

to transfer the waveguide pattern into silica with an Oxford 100 ICP-RIE system using 20 sccm of octafluorocyclobutane (C_4F_8) and 10 sccm of oxygen at a chamber pressure of 6 mT, ICP and RIE powers were 1000 W and 300 W, respectively. As a final step, the silica mask was then used to transfer the waveguide pattern into the underlying AlGaAs wafer-chip.

2.4.2 Etching recipe optimization

A variety of etching chemistries have been used in literature for III-V semiconductors; the two most common etching chemistries are based on either chlorine or methane. Methane based etching chemistries provide very smooth etched-profiles, however, they result in a very low etching rate and also can result in polymer deposition on the etched facets (sidewalls of the waveguides, exposed after etching) and chamber walls of the etcher system. Chlorine based etching recipes are popular as they readily react with AlGaAs resulting in volatile gallium chloride compounds ($GaCl_x$), arsenicum chloride compounds ($AsCl_x$) and aluminum chorlide compounds ($AlCl_x$), hence, facilitating the etching of AlGaAs, *i.e.*, resulting in a high etching rate. Silicon tetrachloride ($SiCl_4$), chlorine (Cl_2) and boron trichloride (BCl_3) are commonly used chlorine sources for III-V plasma etching. BCl_3 provides controlled etching rate, not as rapid as Cl_2 and $SiCl_4$, *i.e.* BCl_3 has lower etching rate than both Cl_2 and $SiCl_4$. It also demonstrates low selectivity of etching rate between AlGaAs compositions, with varying aluminum concentration. Since the claddings

and the core layers of our designs have varying aluminum composition, hence, BCl_3 chemistry is best suited for non-selective etching of our structures [66].

Past studies have shown that a small percentage of an inert gas can stabilize the plasma discharges and, hence, can improve repeatability of the etching process [67]. While inert species, such as argon (Ar) or helium (He), do not chemically react with the III-V compounds, they do, however, etching by physically colliding with the substrate and knocking the substrate atoms out of their crystal lattice. For etching AlGaAs waveguides, we added Ar to BCl_3. Ar atoms are ionized in the plasma and are only involved in the physical etching of AlGaAs. If the etching chemistry were considered as a variable, along with all other ICP-RIE etching parameters, we would have required 40 etch test runs for complete optimization of this etching recipe, as shown in table 2.2, generated using *Design Expert 11*, a design of experiment software. Considering material (epitaxially-grown AlGaAs wafers are very expensive), time and funding constraints, the etching chemistry was not varied for the recipe optimization. It was fixed as follows: 15 sccm of BCl_3 and 5 sccm of Ar, based on the previous studies of this etching chemistry for etching AlGaAs [66, 68]. Etching recipe optimization was then carried out for pressure, ICP power and RIE power of the ICP-RIE process.

Scanning electron microscope (SEM) images were used for a characterizing the etched-profile. Cross-sectional SEM images obtained using Zeiss Ultra 55 SEM system, were used to measure vertical etching rate of AlGaAs and SiO_2 mask by measuring the height of the etched structures and the height of the remaining mask. Etching rates were then calculated using the time duration of each etching run. Another parameter that was measured from SEM images was the average sidewall angle with respect to the horizontal. The term average was used here, since, sidewall angle was not constant, some fluctuations were observed from top to bottom. For accuracy, three measurements were made, and then an average value was selected to the nearest degree; considering uncertainty involved. Figure 2.24 shows the convention used for measuring angle on SEM images using image analyzer software: *ImageJ*. Same software was used to measure the vertical height of AlGaAs waveguides as well as the remaining etching mask, after calibration with SEM scale bars. Selectivity is another important etching parameter. Selectivity was calculated using SEM cross-section images and image analyzer software, as

$$Selectivity = \frac{Etching\ rate\ of\ AlGaAs}{Etching\ rate\ of\ SiO_2\ mask}. \tag{2.18}$$

High selectivity is desirable when optimizing a plasma etching recipe; however, the selectivity is, in general, low in dry etching as compared to wet chemical etching due to physical bombardment by ions. Sometimes Cl_2 is added to the BCl_3-Ar etching chemistry to increase the etching rate and, hence, to improve the selectivity [49]. A plasmatherm PT770 ICP-RIE tool was used for etching AlGaAs at CNF (Cornell). The etching variables, such as pressure (P measured in mT), ICP (power in W, controls plasma density) and RIE (power in W, controls plasma accelaration toward the substrate), were varied to obtain the required etching depths with near-vertical sidewalls and smooth etched-profiles. To optimize the etching recipe, we kept a constant etching time duration of 10 min for each etching test run. A systematic study was done to understand the effect of pressure, ICP and RIE on the etching rate, selectivity and sidewall angle of AlGaAs waveguides. The pressure was varied from 10 mT to 25 mT in steps of 5 mT, while other etching variables were kept constant: ICP = 300 W, RIE = 100 W , time = 10 min and etching chemistry of BCl_3 : Ar = (15 : 5) sccm,

Table 2.2: Complete optimization process for AlGaAs etching using ICP-RIE with an Ar-BCl_3 etching chemistry. Values for the flow rates of Ar and BCl_3, P (Pressure), ICP and RIE powers for each etching test run are shown.

Etch test run No.	Ar/sccm	BCl_3/sccm	P/mT	ICP/W	RIE/W
1	10	5	16.75	238.75	148.5
2	5.0454	9.9546	18.25	345	95
3	0	15	16.75	211.25	52
4	0	15	18.25	299.081	150
5	5.03163	9.96837	10	350	150
6	4.96044	10.0396	15.625	100	50
7	5	10	10.3	212.5	95
8	5	10	10.3	212.5	95
9	9.7	5.3	25	100	150
10	10	5	10	192.5	50
11	0	15	10	256.25	150
12	4.87504	10.125	25	100	113.5
13	4.44021	10.5598	25	305	105
14	10	5	25	350	150
15	2.5	12.5	10	175	50
16	10	5	25	100	50
17	10	5	16.75	106.25	95
18	5.12043	9.87957	10	350	50
19	4.90979	10.0902	25	350	150
20	10	5	10	100	150
21	10	5	10	350	112
22	7.39364	7.60636	17.5	225	71.3026
23	0	15	16.75	346.25	105.5
24	5.18324	9.81676	25	256.25	50
25	0.3	14.7	25	350	50
26	3.1385	11.8615	10	336.25	99.5
27	0	15	24.625	212.5	105
28	4.96398	10.036	18.25	212.5	148
29	0	15	10	100	88
30	10	5	24.7	237.5	95
31	4.99618	10.0038	10	100	150
32	4.96398	10.036	18.25	212.5	148
33	5.0454	9.9546	18.25	345	95
34	0	15	19.375	100	150
35	0	15	10	350	50
36	4.96398	10.036	18.25	212.5	148
37	10	5	19.525	350	50
38	0	15	25	350	150
39	4.87504	10.125	25	100	113.5
40	0	15	25	100	50

for each etching test. After cleaving the etching test sample, cross-sectional SEM images were used to measure the etching depth (and, consequently, the etching rate

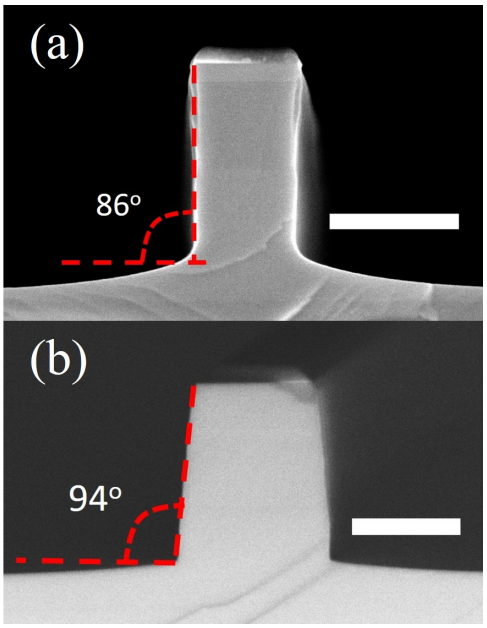

Figure 2.24: Cross-sectional SEM images of AlGaAs waveguides used for measuring sidewall angle: (a) shows an acute angle measured with respect to the horizontal direction along the substrate, whereas (b) shows an obtuse angle measured with respect to the horizontal direction along the substrate.

since the etching time was fixed at 10 min), the selectivity (as defined by equation 2.18) and the sidewall angle (using the convention shown in Figure 2.24). The effect of the variation of the chamber pressure on each of these etching parameters is presented in Figure 2.25.

As the chamber pressure was increased, the collision mean free path of the gas phase species and ions reduces, hence, increasing the proportion of chemically reactive species available for chemical etching and reducing the number of ions available for physical etching [47, 69]. At lower chamber pressure values, physical etching dominates due to the larger mean free paths for the ions. As the pressure was increased, the etch rate initially increased up to the point where the pressure reached 20 mT, and then the etch rate started to reduce with further increase of the pressure. This reduction happens because when the chamber pressure reaches too high values, the collisions and inter-reactions between the reactive species reduces the reactions with the material to be etched (AlGaAs in this case) [47]. It can be seen from figure 2.25 (b) that, as the pressure was increased, chemical etching was enhanced, resulting in higher selectivity. The sidewall angle depends on the balance between the physical and chemical etching as well as how rapidly the etching mask is eroded (Etching of mask results in the mask edges being removed, leading to reduction in the width of the pattern). Low mask erosion results in better verticality of the sidewalls, whereas, increased mask erosion reduces sidewall verticality, hence, not desirable. Since the physical etching dominates at lower chamber pressures, the sidewall angle increases due to the mask erosion, as shown in figure 2.25 (c). A chamber pressure of 15 mT was chosen as the optimum value since it resulted in the selectivity and AlGaAs etching rate values suitable for the required etching depth, as per our waveguide designs, while maintaining a smooth etched-profile and providing nearly vertical sidewalls.

In order to understand the effect of the ICP power on the etching parameters, all

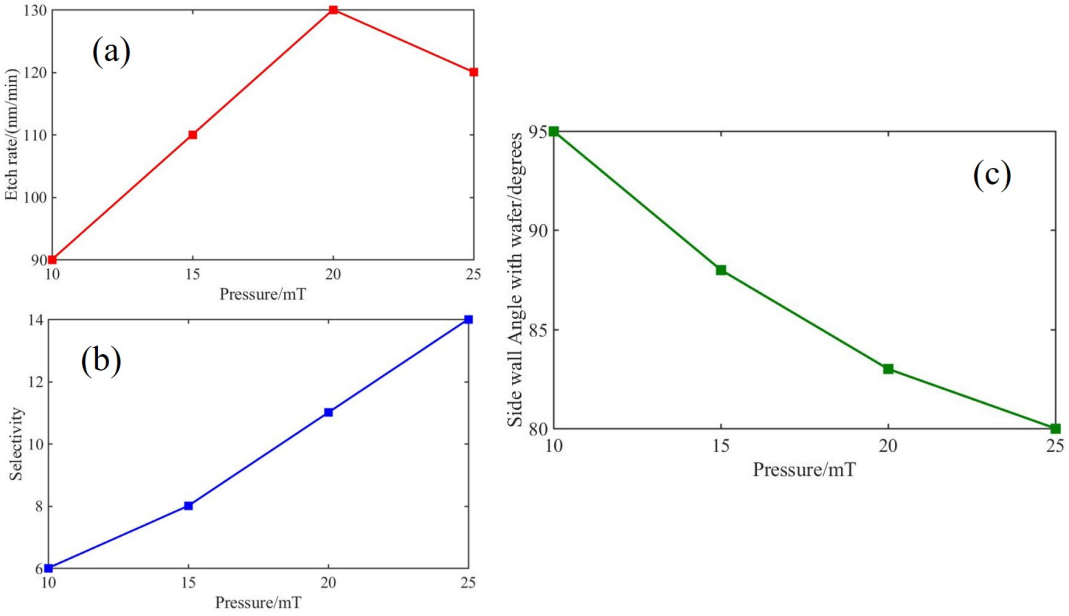

Figure 2.25: The effect of the chamber pressure on the etching parameters, while all other etching variables were kept constant: ICP = 300 W, RIE = 100 W , time = 10 min and etch chemistry of BCl_3 : Ar = (15 : 5) sccm. The effect of varying pressure on: (a) etching rate of AlGaAs, measured in nm/min, (b) selectivity between AlGaAs and SiO_2 mask, and (c) sidewall angle of AlGaAs waveguides is shown. The lines are drawn to guide the eye.

other etching variables were kept constant: P = 15 mT , RIE = 100 W , time = 10 min and the etching chemistry of BCl_3:Ar = (15:5) sccm, while the ICP power was varied from 150 W to 350 W in steps of 50 W. The effect on the etching rate, selectivity and sidewall angle were as shown in figure 2.26. Since the ICP power is responsible for the generation of plasma in the etching chamber, its increase resultes in an increase of the degree of ionization, *i.e.*, more ions become available for physical etching. This results, in turn, in an increased radical production, and, hence, in the enhancement of the chemical etching as well. Thus, an increase in the ICP power has resulted in an increase in the etching rate, as shown in figure 2.26 (a). Similarly, for the effect of the ICP power on the selectivity, as shown in figure 2.26 (b), the selectivity initially increased with an increase of the ICP power due to an enhanced AlGaAs etching thanks to the abundant chlorine and methane radicals. However, as the ICP power was increased further, the selectivity dropped due to an enhanced physical etching, which resulted in a rapid mask erosion due to the increased density of ions. It can be seen from figure 2.26 (c) that the sidewall angle reduced with an increase of the ICP power. This is due to an enhancement of the chemical etching at higher ICP power, resulting in an increase in the undercut of the waveguides, and, hence, in the acute (or decreasing) sidewall angles. An ICP power of 200 W was chosen as the best option, since it resulted in near-vertical waveguide sidewalls with a high etching rate and a high selectivity.

RIE power is another important etching variable as it dictates the proportion of the physical etching in an ICP-RIE etching recipe. To obtain an optimized value for the RIE power for AlGaAs structure, the RIE power was varied from 50 W to 150 W in steps of 25 W, while all other etching parameters were kept fixed: P = 15 mT, ICP = 200 W, time = 10 min and etching chemistry of BCl_3:Ar = (15:5) sccm. The effect of

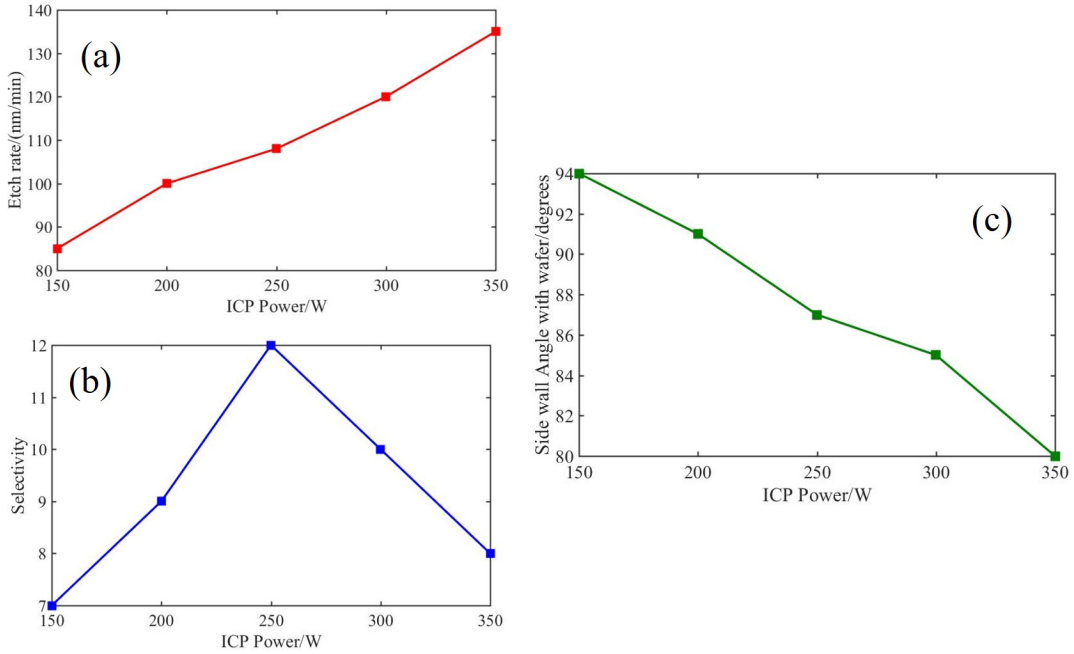

Figure 2.26: Effect of the ICP power on the etching parameters, while all other etching variables were kept constant: P = 15 mT, RIE = 100 W, time = 10 min and etching chemistry BCl_3:Ar = (15:5) sccm. The effect of varying ICP power on (a) the etching rate of AlGaAs, measured in nm/min, (b) the selectivity between AlGaAs and SiO_2 mask, and (c) the sidewall angle of AlGaAs waveguides is shown. The lines are drawn to guide the eye.

the RIE power variation on the etching rate, selectivity and sidewall angle has been studied, and is presented in figure 2.27. The AlGaAs etching rate increased with the increase of the RIE power, due to enhanced physical etching: the ions acquired a higher kinetic energy due to a larger bias between the plasma and the sample. The higher kinetic energy results in higher ion velocities and, hence, in a higher physical etching rate. Similarly, for the effect of the RIE power on the selectivity, figure 2.27 (b) shows that the selectivity dropped significantly as the RIE power increased. This is related to the fact that, as RIE power increases, the physical etching is enhanced, reducing the etching selectivity as it removes both the SiO_2 mask and AlGaAs at the same rate (an example of a purely physical etching process is ion milling, and it has a very low selectivity, if any, between the mask and the material to be etched). The effect of the RIE power on the sidewall angle is displayed in figure 2.27 (c). The sidewall angle increased from an acute to an obtuse angle with the increase of the RIE power (see figure 2.24 for SEM analysis of the sidewall angles). This can be understood as follows: initially, with an increase in the RIE power, the directional (anisotropic) etching is achieved, leading to nearly-vertical sidewalls. However, as the RIE power increases further, the mask erosion leads to larger sidewall angles. Based on these results, 75 W was chosen as the RIE power for etching the final samples as it provides nearly vertical sidewalls with good selectivity and etching rate.

Once an optimized etch recipe for AlGaAs was reached, the etch time required for each type of waveguides was computed, and the final samples were etched. It is important to point out that, due to the non-selective etching of AlGaAs (irrespective of Aluminum concentration) by the BCl_3 etch chemistry, the same etch recipe worked equally well for different wafer compositions. We thus used the same etch

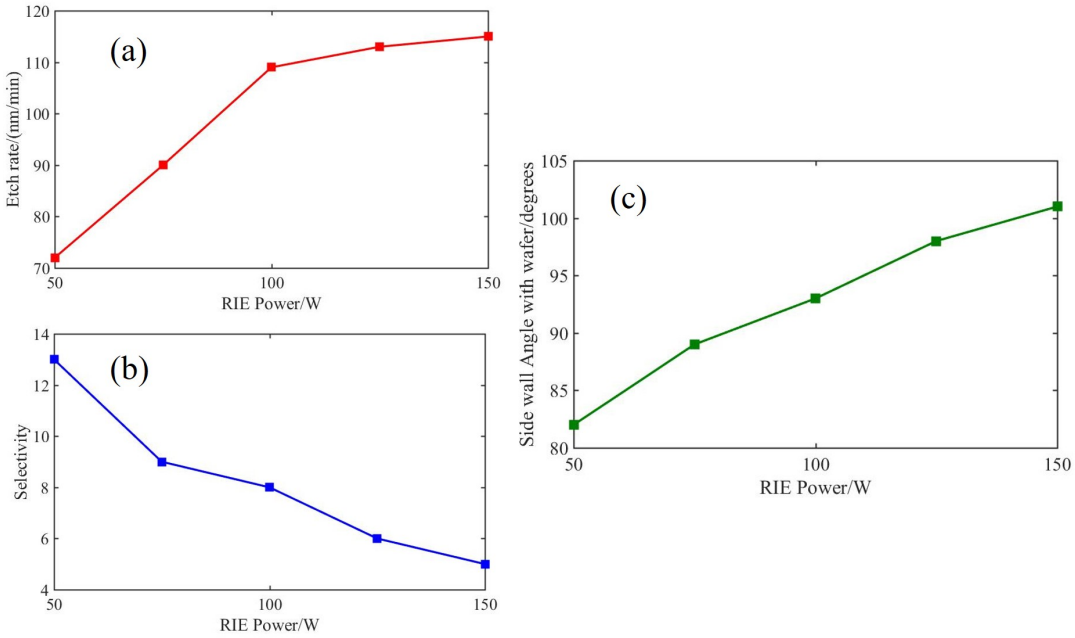

Figure 2.27: Effect of the RIE power on the etching parameters, while all other etching variables are kept constant: P = 15 mT, ICP = 200 W, time = 10 min and etching chemistry of BCl_3:Ar = (15:5) sccm. The effect of the RIE power variation on: (a) the etching rate of AlGaAs, measured in nm/min, (b) the selectivity between AlGaAs and SiO_2 mask, and (c) the sidewall angle of AlGaAs waveguides is shown. The lines are drawn to guide the eye.

recipe for all three types of AlGaAs waveguides, namely: the strip-loaded, half-core and nanowires. It is also important to note that the process of recipe discovery (the term commonly used by process engineers for recipe optimization), as presented here, is more suitable for an etching system with multiple users, working on a variety of materials and etching chemistries. This exposure of the etching-chamber to a variety of materials and etching chemistries (as was the case for the CNF ICP-RIE system, since it was used for a wide variety of III-V semiconductors) results in the etching-chamber conditions (materials deposited on chamber walls) changing over time. This variation is taken care of, as we optimized one etching parameter at a time, resulting in any changes of the etching-chamber being included in the optimization process. Figure 2.28 shows the SEM cross-sectional images of the strip-loaded, the half-core and the nanowire waveguides as etched by the optimized recipe, with the following etching parameters:

$$BCl_3 : Ar = (15 : 5)\ \text{sccm},\ P = 15\ \text{mT}\ ,\ ICP = 200\ \text{W and RIE} = 75\ \text{W}$$

2.4.3 Sample preparation for optical characterization

The fabricated AlGaAs waveguide samples had 12-mm-long waveguides, with at least 3-mm-long, 2-μm-wide coupling regions followed by tapers connecting the coupling waveguides to the actual waveguides (with the designed width). The coupling regions were required, due to the fact that, it is challenging to couple light into a waveguide with the width smaller than 1 μm, which is the case for some of our waveguides. The schematic layout of each waveguide is shown in figure 2.29 (a), and the cross-sectional SEM image is shown in figure 2.29 (b).

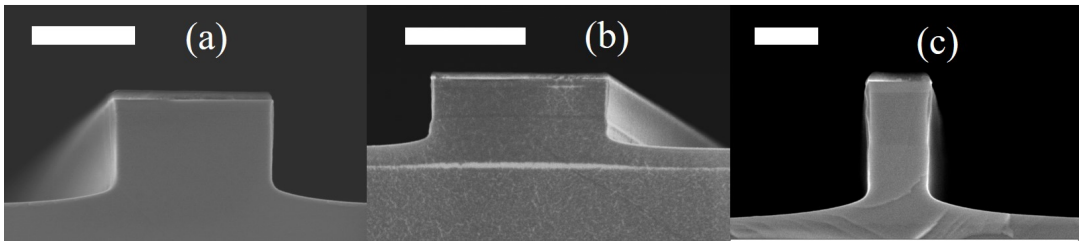

Figure 2.28: Cross-sectional SEM image of: (a) AlGaAs strip-loaded waveguide, (b) AlGaAs half-core waveguide and (c) AlGaAs nanowire waveguide. All scale bars represent 500 nm.

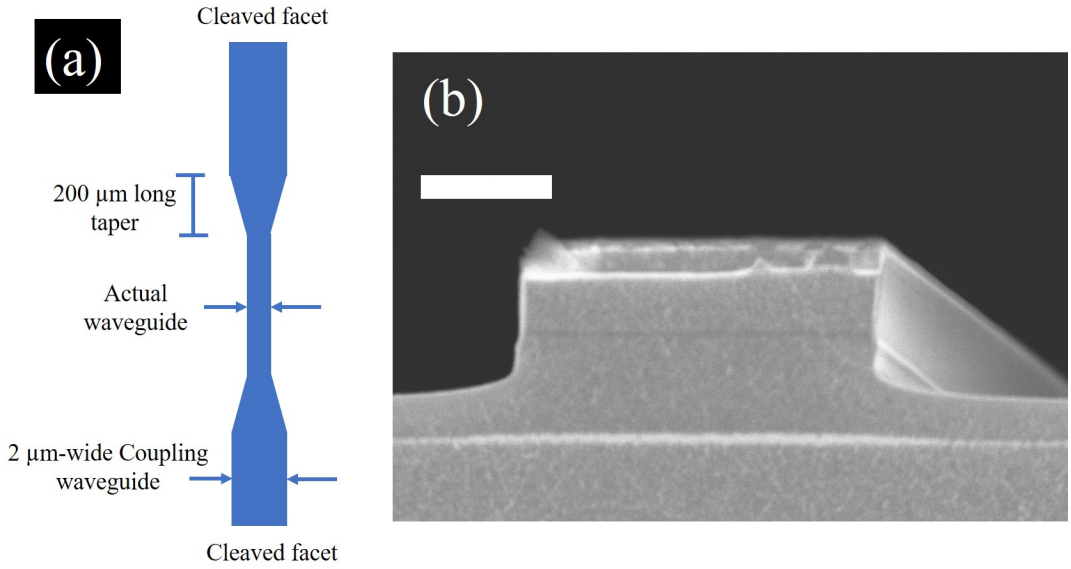

Figure 2.29: (a) The top-view of the layout for each waveguide on the sample, showing coupling waveguides, tapers, actual waveguide and end-facets after cleaving. (b) Cross-sectional SEM image of the end facet of a half-core waveguide; the scale bar represents 500 nm.

We used edge-coupling for the optical characterization of the fabricated waveguide samples. In order to perform an edge-coupling, the waveguides need to be well cleaved to be exposed to a focused laser beam. Cleaving is the process of breaking a semiconductor piece into smaller pieces in a controlled way by a small scribe made with a diamond-edged cleaver. The lattice-matched III-V stacks were cleaved along their crystal planes. Therefore, the outcome of such a cleaving process is well cleaved waveguide structures with atomic-level-smooth facets, which is highly desirable for the edge coupling of light. Hence, no post-cleaving edge polishing was required for obtaining quality facets.

2.5 Optical characterization

To experimentally prove that half-core waveguides can provide advantages of both nanowire and strip-loaded waveguides, linear optical propagation losses of the fabricated AlGaAs waveguides were measured using Fabry-Perot method [70].

2.5.1 Fabry-Perot method

In Fabry-Perot method of propagation loss measurement, it is assumed that each waveguide acts as a Fabry-Perot cavity for the light propagating back and forth and getting reflected at each waveguide's facet interface with the air. Therefore the same procedure used in resonators is followed in order to calculate the propagation loss.

The overall loss in these waveguides comprised of the propagation loss L_{prop}, the coupling loss due to the mode size and shape mismatch between the free-space focused laser beam and waveguide mode L_{coupl}, and the Fresnel reflection loss L_{ref}:

$$L_{\text{t}} = L_{\text{coupl}} + 2L_{\text{ref}} + L_{\text{prop}}L, \tag{2.19}$$

where L represents the overall length of the waveguide, and the propagation loss was measured using the Fabry-Perot loss measurement technique, which will be discussed further.

On our waveguide samples, we had a variety of waveguide structures, to facilitate the propagation loss measurement. The different waveguide structures included on each sample are schematically presented in figure 2.30. The reference waveguide,

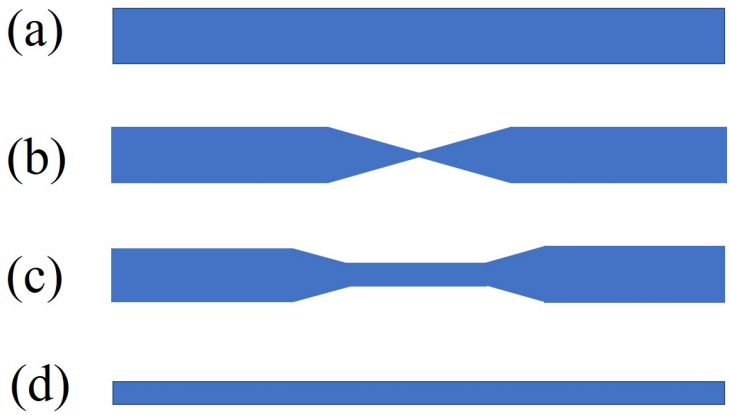

Figure 2.30: Schematic representing different types of waveguide structures for each waveguide width, fabricated on all samples: (a) Reference waveguide, which is a 2 μm-wide straight waveguide, (b) taper-to-taper waveguide, the 2 μm-wide coupling waveguide is tapered down to a desired width and then tapered up to 2 μm immediately (for the measurement of the loss due to the tapered regions), (c) tapered waveguide where the coupling region tapered down to the width of the designed waveguide which now has some non-zero length, and then there is an inverse taper back to the coupling waveguide width, and (d) non-tapered waveguide, which is a straight waveguide with the designed width.

shown in figure 2.30 (a), was a 2 μm wide coupling waveguide (needed to facilitate light coupling into waveguides less than 1 μm wide). The 2 μm coupling waveguide was tapered into the actual waveguide width (as per design), via a 200 μm long taper. To measure the taper losses, taper-to-taper waveguides were included for each waveguide width, as shown in figure 2.30 (b). The actual waveguides, as per designed waveguide widths, were included in two forms: firstly with a coupling region [shown in figure 2.30 (c)], and then, as a straight waveguide [non-tapered waveguide, as shown in figure 2.30 (d)].

The Fabry-Perot measurements were performed on the transmission data obtained using the optical setup (presented later). Figure 2.31 shows the Fabry-Perot resonances, observed for 2 μm wide reference waveguides, of the strip-loaded waveguide sample. Propagation losses were calculated using Fabry-Perot analysis, by first

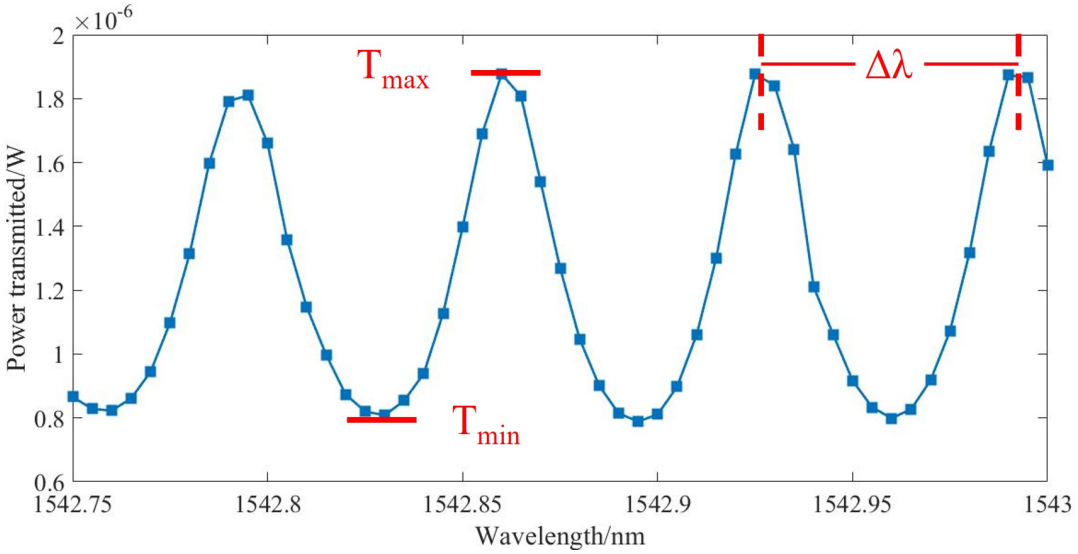

Figure 2.31: Measured transmission power, as a function of wavelength for 2 μm-wide reference waveguide on strip-loaded sample. T_{max}, T_{min} and $\Delta\lambda$ calculated using these plots for Fabry-Perot calculations.

measuring the length of the waveguide (L), using a vernier caliper. $\Delta\lambda$—the free spectral range of the fabry-perot cavity (straight waveguides, in this case)—is then determined experimentally, from the transmission measurements, as labeled on Figure 2.31. The effective refractive index (n_{eff}) is then calculated using free spectral range relation

$$\Delta\lambda = \frac{\lambda^2}{2n_{\text{eff}}L}. \tag{2.20}$$

The linear loss coefficient (α), is defined as

$$\alpha = \frac{1}{L} ln(\frac{1-\sqrt{1-K^2}}{RK}), \tag{2.21}$$

where, the facet reflectivity (R) is defined as

$$R = (\frac{n_{\text{eff}}-1}{n_{\text{eff}}+1})^2, \tag{2.22}$$

and, the peak-to-peak transmission coefficient (K), is defined as

$$K = \frac{T_{\text{max}} - T_{\text{min}}}{T_{\text{max}} + T_{\text{min}}} \tag{2.23}$$

[70]. The maximum and minimum transmission (T_{max} and T_{min}, respectively), were experimentally determined, as shown on Figure 2.31. Experimental values of K, R and L, are then substituted into equation 2.21, to obtain the propagation loss coefficient, α.

2.5.2 Optical setup

Propagation losses were measured for both TE and TM polarizations. In order to perform the loss measurement, we have excited the fundamental TE and TM modes in our waveguides. Figure 2.32 shows the optical setup used for measuring the required parameters. A tunable cw semiconductor laser, Santec TSL 710, was used

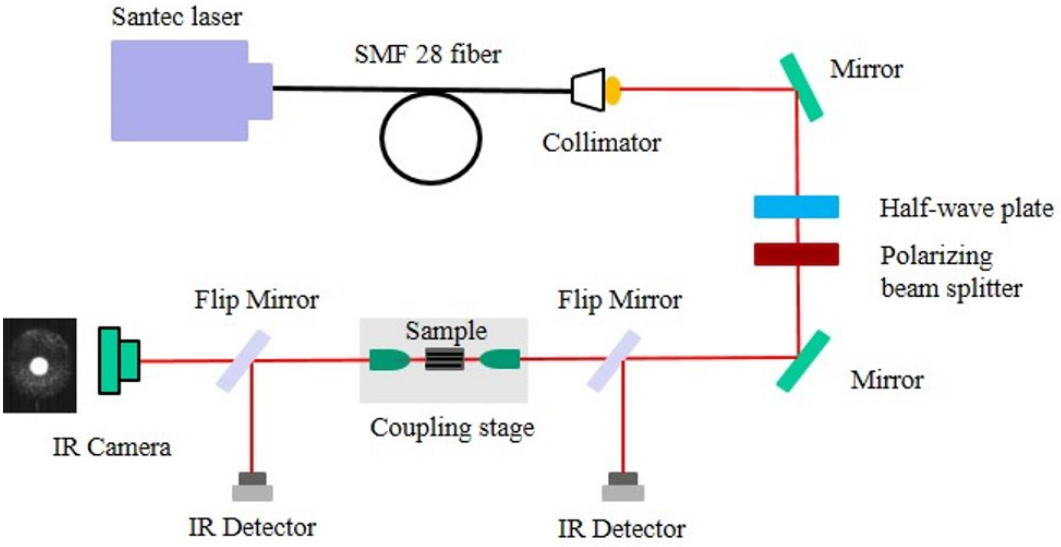

Figure 2.32: Schematic of the optical characterization setup, used for measuring the propagation loss by Fabry-Perot method. The inset displays the image of a guided mode as seen on the IR camera.

as the light source for the Fabry-Perot loss measurement in the wavelength range around 1550 nm. The light from the laser source was first coupled into a single-mode SMF28 fiber, and then collimated for free-space coupling into the waveguides. The collimated laser beam was then polarized (TE or TM) using a half-wave plate and a polarizing beam splitter. The polarized light was then butt-coupled into the waveguide using a 40× microscopic objective mounted on a 3-axis micrometer coupling stage. The light was then coupled out of the waveguide with a 20× microscopic objective. An IR photodetector was used to measure the optical power at the waveguide output, as the function of wavelength. Fabry-Perot loss analysis was then performed for each type of waveguide [70].

2.5.3 Experimentally determined propagation loss

The Fabry-perot method, described in Section 2.5.1 , and the optical setup as shown in figure 2.32 were used to experimentally determine propagation loss for strip-loaded, nanowire and half-core waveguides. Waveguides with a variety of widths were characterized for both TE and TM polarizations. Since Fabry-perot method is more accurate than using taper-based calculations (using coupling waveguides and equation 2.19, hence, only straight (non-taper) waveguides were used for the loss measurements. Table 2.3 summarizes the results of the loss measurement for each type of waveguide. We were not able to measure the optical losses for 0.7 μm-wide nanowire waveguides as we were unable to couple light into those, due to the fact that these devices had very high propagation losses (which is typical of the smaller-width nanowire waveguides).

Table 2.3: Measured propagation loss α in dB/cm for each type of AlGaAs waveguides for different waveguide widths. Losses are measured for both TE and TM polarizations.

Type of waveguide	waveguide width in μm	α_{TE} in dB/cm	α_{TM} in dB/cm
Strip-loaded	0.9	1.25	1.30
	1.0	1.18	1.22
	1.1	1.10	1.20
	1.2	1.12	1.21
Nanowire	0.7	-	-
	0.8	12.95	12.26
	0.9	11.0	10.60
	1.0	11.2	10.70
Half-core	0.8	2.10	1.85
	0.9	1.70	1.65
	1.0	1.63	1.47
	1.1	1.64	1.44

2.6 Conclusion and future work

Figure 2.33 shows the picture summary of this work, using SEM images of the fabricated waveguides, along with the values of the effective mode area obtained from the simulations, and the experimentally measured propagation loss values for TE polarization of the optimized design of each type of AlGaAs waveguide. These re-

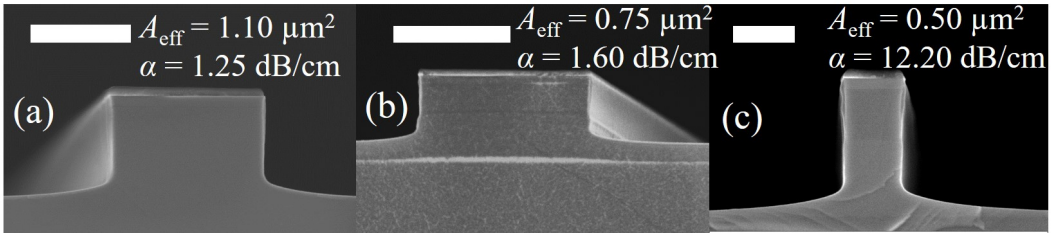

Figure 2.33: Cross-sectional SEM image of AlGaAs (a) strip-loaded waveguide, (b) half-core waveguide and (c) nanowire. Each bar represents 0.5 μm. The values of the effective mode area and experimentally measured propagation losses are also shown for each waveguide design.

sults prove our hypothesis that half-core etched waveguide can provide good confinement (as compared to strip-loaded waveguides) with lower propagation loss (as compared to nanowire waveguides). We thus conclude that such waveguides can be suitable for all-optical wavelength conversion applications. However, since half-core waveguides cannot be dispersion-engineered, such waveguides are only suitable for the applications that require small frequency conversion range, such as telecommunications. For the applications that require wide tuning range (above 100 nm), AlGaAs nanowire waveguides are the best option.

Our intended future work on AlGaAs waveguides for integrated nonlinear optics, includes, developing post-processing wet chemical techniques—for reduction

of propagation losses—and chemical passivation—to make the samples less susceptible to aluminum oxidation. Furthermore, the difficulty faced in deep plasma etching of these structures, and the low refractive index contrast between the guiding layers and the cladding layers of our wafer design, shows that this multilayer arrangement is not the best approach for achieving compact and efficient integrated AlGaAs waveguides, with enhanced nonlinear optical effects. Instead, an alternative approach of using 'AlGaAs on insulator', arrangement can work better, as shown by Pu, *et al.* [71]. Such an approach, is feasible from the fabrication point of view, due to shallow etching requirement, and results in compact waveguides with low effective modal areas, and possibility of dispersion engineering. We plan on testing such AlGaAs-on-insulator waveguides in near-future. Our simulations show an effective mode area, as small as 0.12 μm^2 for the TE mode of the waveguide structure shown in figure 2.34. Since the core layer is only 300 nm thick, so the required etching depth is also 300 nm—as compared to the required etching depth of 1400 nm, for the layered nanowire structure.

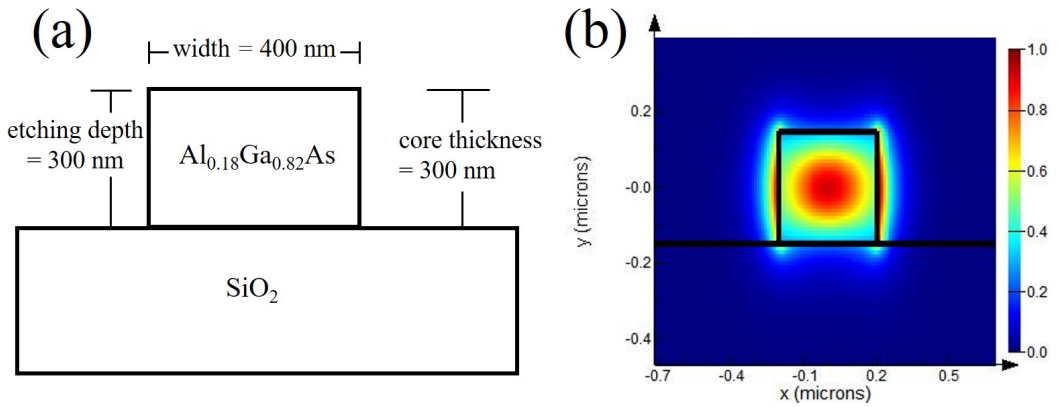

Figure 2.34: AlGaAs on insulator waveguide design (a) schematic showing the dimensions of the waveguide design, (b) Simulated intensity distribution for the waveguide dimensions shown in (a), at wavelength 1550 nm.

Chapter 3

Fabrication of GaAs-AlGaAs photonic crystals

3.1 Photonic crystals: Semiconductors of light

The concept of photonic crystals was in itself a revolution introduced by Yablonovitch in his seminal paper [72], where he also coined the term semiconductors of light. Yablonovitch pointed that the refractive index of the material should alternate periodically between high and low values, on a distance scale of the order of half of the wavelength of light in the composite medium, to enable strong Bragg reflection effects. He further stated that such periodic dielectric structures can inhibit the propagation of light through the composite medium to such an extent that it would become, in principle, impossible for light—within a designed wavelength range—to propagate in any direction within the composite material [72, 73]. This omnidirectional stop-band behavior of light in such composite materials could be best understood as being analogous to the behavior of electrons in single-crystal semiconductors, hence the term photonic crystals (PC). It must be emphasized here that the behavior of light under these circumstances is a wave-propagation phenomenon in the form of generalized Bragg diffraction, rather than a form of photon (i.e. particle-like) behavior [72, 73].

The wavelength range covered by these stop-bands depends on the choice of direction with respect to the defining axes of the photonic crystal and selection of the periodicity scale. When the periodic refractive index variation is sufficiently large, full photonic bandgap (PBG) phenomena can be observed. Due to the analogy of PCs with semiconductors, the behavior of light is characterized by band structure. Furthermore, concepts from solid-state theory such as densities of states are also adaptede in describing the optical properties of PCs [73].

After Yablonovitch's break through paper, another important early work about PCs was published by Sajeev John [74]. It discussed the possibility of localized states by introducing defect within PCs, hence foretelling later demonstrations of photonic crystal waveguides and cavities in PC structures. This work was of large importance as it explained how the propagation of light is determined by periodic structuring of a medium and how light propagation can be radically modified by the introduction of defect states in this periodic bulk PC [74].

3.1.1 2D photonic crystals

The most general case of a PC structure was observed in "3-space", i.e., a lattice with a three-dimensional periodicity. However, a large fraction of the effects associated with PCs can be understood by examining the effect of periodicity in a

two-dimensionally periodic structure (2D PCs), thereby neglecting the third dimension for simplicity, and also making it realizable, from the device fabrication point of view [73, 75]. Figure 3.1, reproduced from Joannopoulos, shows schematics of 1D, 2D and 3D PCs [76]. 3D PC structures, operating at optical wavelengths, have

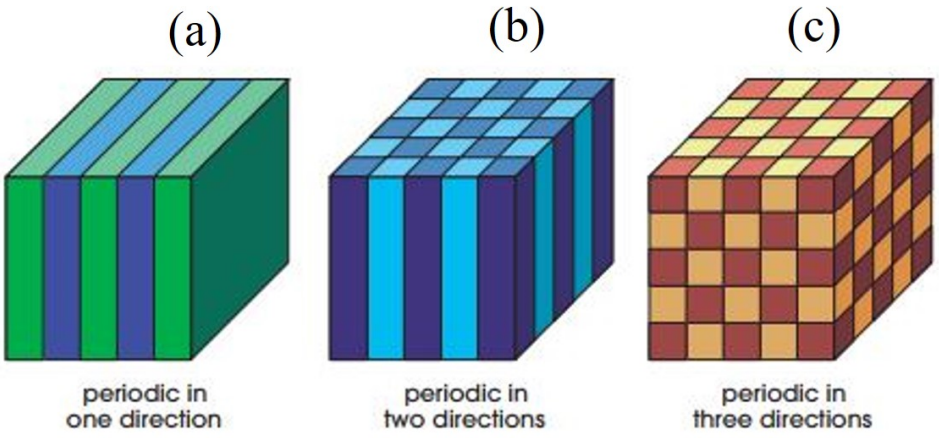

Figure 3.1: Schematic representations of photonic crystal lattices with (a) 1D, (b) 2D and (c) 3D periodicities [76].

been fabricated [77, 78]; however, they lack reproducibility and require highly complicated fabrication process. Most importantly, 3D PCs lack design versatility required to implement functional devices [75, 79]. Furthermore, such a fabrication approach is not suitable for mass production of PC-based devices. On the other hand, 2D PC structures are more suitable for controlled fabrication using existing mature nanofabrication techniques (especially since the advent of electron beam lithography and deep-ultraviolet photolithography). This made 2D PCs more attractive for both applications, as well as fundamental studies, as compared to their 3D counterparts [75, 79].

2D PCs in semiconductor media have been studied extensively. They are commonly known as PC slabs. They consist of a 2D periodic array of structural features, made from an otherwise uniform thin layer (hence the term slab) of a dielectric material (semiconductors and polymers are commonly used). Light is laterally confined due to the structural properties of PC (PBG effect), whereas in the direction perpendicular to the propagation of light, the confinement is achieved by total internal reflection (refractive index contrast, or simply waveguiding effect). Therefore, the dielectric layer from which the PC is made, must have a higher refractive index (RI) than the surrounding material [79]. The two most commonly used structural arrangements of 2D slab PCs are: a periodic lattice of high-RI pillars in a low-RI background material, and a periodic lattice of low-RI holes within a high-RI slab (semiconductor material in case of our study). The schematics of these two geometries are shown in figure 3.2, reproduced from [79].

3.1.2 Defect modes in PC slabs

2D PCs take advantage of their photonic band gap and the engineering of defect modes within it, to form low-loss nanophotonic components that can control spectral and spatial properties of light [80, 81]. These nanophotonic components include,

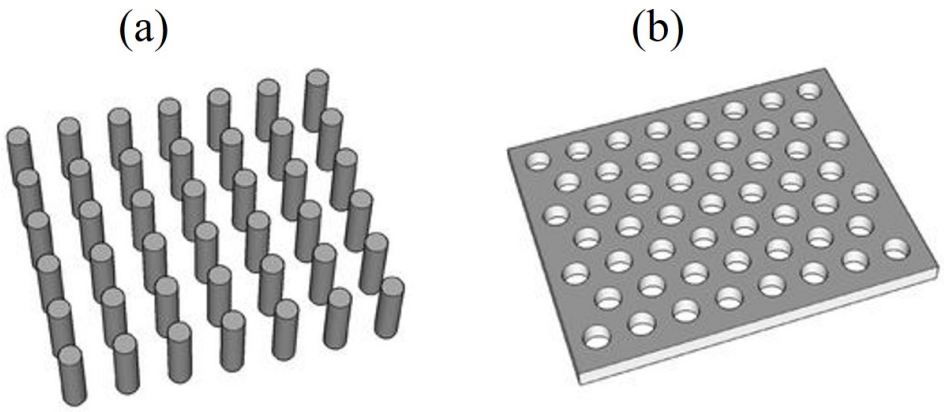

Figure 3.2: Schematics of 2D PC slab geometries, representing: (a) a square lattice of high-RI pillars in low-RI air, and (b) a triangular lattice of low-RI holes in a high-RI dielectric layer [79].

optical resonators with large quality factors (high-Q) and sub-wavelength mode volumes, and high-confinement slow-light waveguides (with precise control over dispersion properties) [80–86]. Significant amount of work has been done on the development of the fabrication processes that faithfully reproduce the PC designs.

Bulk PCs can be used for guiding light, through a line defect. The simplest PC waveguide consists of a bulk PC with one row of holes missing. This row of missing holes, represents a defect from the standpoint of the periodicity of the PC structure, and can guide light. The light is bounded by the PBG on either side of this defect. Figure 3.3 (a) shows SEM top-view image of bulk silicon PC, whereas Figure 3.3 (b) shows a line-defect resulting in a PC waveguide. The SEM images are taken from our

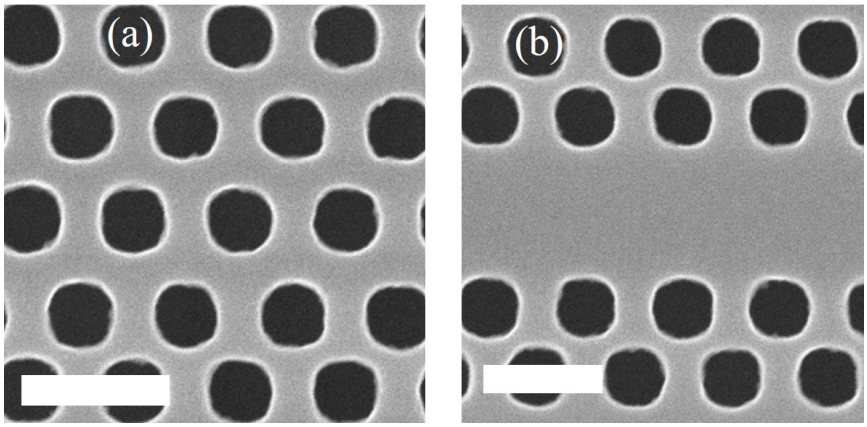

Figure 3.3: Top-view SEM images of (a) bulk silicon PC, (b) line-defect, resulting in silicon PC waveguide. All scale bars represent 500 nm.

work on slow-light in silicon PC waveguides [48]. Similarly, one can confine light in all directions, effectively creating a cavity. The simplest cavity in case of a slab PC is H1 nanocavity, where one hole is missing in the bulk PC. Once light is coupled to this point-defect, it is trapped due to the PBG and by total internal reflection, hence resulting in high-Q nanocavities. Other popular and useful PC nanocavities include, the L3 (3 missing holes form the cavity) and the H0 (none of the holes are

missing, instead, the defect is created by changing periodicity of a cluster of holes) PC nanocavity.

3.2 Polariton quantum blockade in a photonic dot

Numerous PC nanocavity designs have been demonstrated, including the aforementioned; H1, H0 and L3 nanocavities [81, 83]. The density of states has a peak at the defect in the bulk PC for such nanocavities, where, the defect mode cannot propagate through the rest of the crystal, since its frequency lies within the PBG [76]. One can intuitively consider the crystal boundary as a highly reflective mirror. Once a mode is excited in the defect, light can be trapped there for an extended time (many number of field oscillation cycles). This results in very high values of the quality factors of PC nanocavities, and, at the same time, in a very small mode volume. It must be noted here, that high quality factors can only be achieved, if the fabrication of the PC nanocavities results in high fidelity to the design, *i.e.*, homogeneous bulk PC as per the designed dimensions, with vertical sidewalls and smooth etched facets.

PC nanocavities are ultra-compact and frequency-selective, hence, they have been proposed as optical devices whose function is to selectively drop (or add) photons with various energies from (or to) optical communication traffic. They can facilitate the development of all-optical circuits incorporating a variety of nanophotonic components, including photonic bandgap waveguides and resonators [81]. PC nanocavities also provide possibility of strong light-matter interaction, due to high intensities building up within a very small cavity volume. This makes them an ideal system to study light-matter interaction, and also a platform for applications dependent on strong light-matter interaction, such as creation of polaritons.

3.2.1 Polaritons

An exciton is an optically active dipole that results from the Coulomb interaction between an electron in the conduction band and a hole in the valence band. Quantum wells embedded in PC nanocavities operating in the strong coupling regime of the light–matter interaction can give rise to new eigenmodes, called polaritons, generated due to the interaction of excitons and photons, as shown in Figure 3.4 reproduced from Kasprzak, *et al.* [87]. Recent advances in nanofabrication techniques have enabled the fabrication of high-quality photonic dots that can confine photon without spoiling the strong coupling with the quantum well exciton. This way, polaritons are produced that are confined in all three dimensions, with a large vacuum Rabi splitting [87, 88].

It has been theoretically shown, by Verger, *et al.* [87, 88], that if the photonic confinement volume (of a cavity with an embedded quantum well) is small enough, the presence of just one polariton can block the resonant injection of a second polariton, as the polariton-polariton interaction shifts the resonance frequency by an amount on the order of the linewidth of the nanocavity or by even more. The emitted light is, therefore, strongly anti-bunched. With a pulsed laser as an excitation source, such a system (nanocavity with resonant embedded quantum well) can be used as a single-photon light emitter, with a radiative emission time on the order of a few ps, hence making it highly attractive for high-speed quantum computing and communications [88].

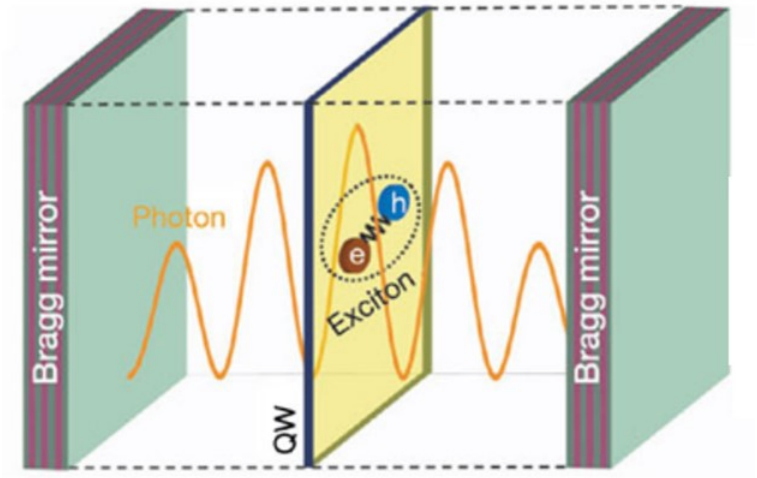

Figure 3.4: Schematic representation of the creation of polaritons in an optical cavity. It shows a Fabry–Perot resonator with two Bragg mirrors at resonance with the excitons in the quantum well, resulting in the generation of polaritons [87].

3.2.2 Proposed device

We propose to experimentally demonstrate the predictions made by Verger, *et al.* [88]. Since a quantum well is a primary requirement for the generation of excitons and, subsequently, polaritons, we decided to use III-V semiconductors-based PC nanocavities. Furthermore, for having high refractive index contrast, an air-slab was required, *i.e.*, a material system was needed that can easily be undercut selectively (etching underlying layer without etching the slab). since we require a high-Q nanocavity, we had to select a semiconductor material system that has well-established fabrication process (resulting in low defects, hence, lower losses and higher Q). Among III-V semiconductors, GaAs fits these requirements very well. Hence, GaAs was selected as the material for the slab, with embedded $In_{0.03}Ga_{0.97}As$ quantum well and a sacrificial layer consisting of $Al_{0.80}Ga_{0.20}As$, which can selectively be etched for creating GaAs air-bridge. Figure 3.5 shows the schematic of our proposed wafer stack design for a polariton blockade device.

This work is a collaborative effort of five research groups. Prof. Savona's group at EPFL (Switzerland) worked on the design of the PC nanocavities. H0, H1 and L3 PC nanocavities were designed using a genetic algorithm. The design goal was to have a reasonably high-Q while keeping a mode profile without spoiling strong coupling between the confined photon and the quantum-well exciton [89]. The wafer stack was grown via MBE technique by Prof. Imamoglu's group at ETHZ (Switzerland). The initial characterization of quantum wells performed to measure the quantum well band-gap was also carried out at ETHZ. Prof. Antonio Badolato, Prof. Dolgaleva and Prof. Boyd's research groups collaborated on the fabrication of the nanocavities at CNF (Cornell). The ultimate optical characterization is to be carried out by Prof. Badolato's group.

Since the work is still in progress, we cannot provide the actual design parameters in this thesis. The designs were created using genetic algorithm, similar to the H1 cavity design shown in Figure 3.6 reproduced from Prof. Savona's work [89]. The hole translations (as compared to standard H1 cavity) were optimized using a

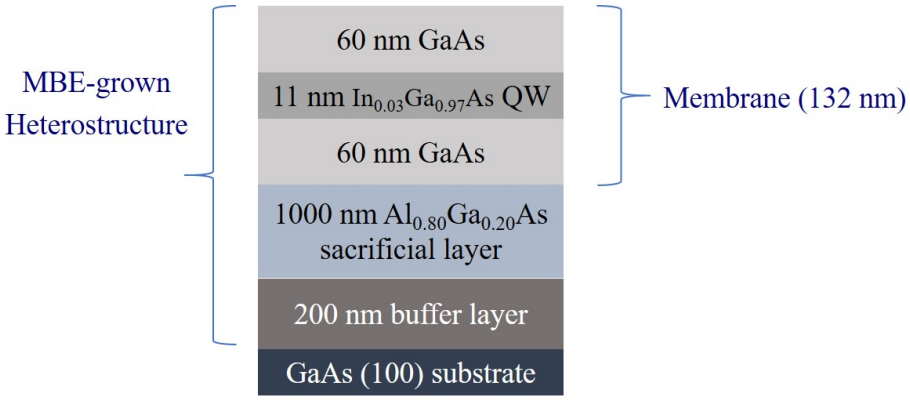

Figure 3.5: Schematic representation of the designed wafer stack for the polariton blockade device. $In_{0.03}Ga_{0.97}As$ quantum wells are embedded within GaAs slab, whereas $Al_{0.80}Ga_{0.20}As$ is used as the sacrificial layer.

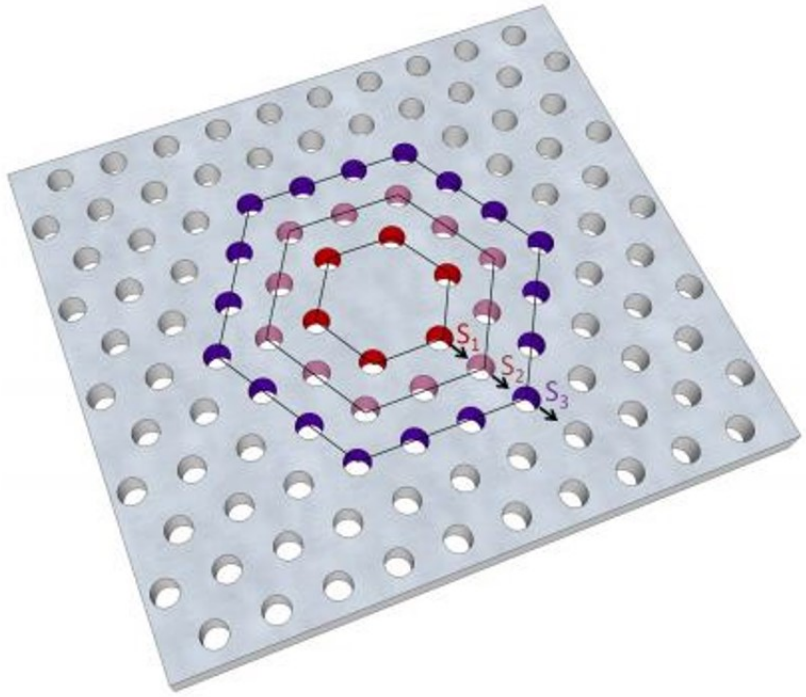

Figure 3.6: Schematic representation of the design variables S_1, S_2 and S_3 that were optimized for the final PC H1 nanocavity design. A similar optimization was carried out for H0 and L3 nanocavities [89].

genetic algorithm, similar design optimizations were performed for H0 and L3 cavities.

3.3 Fabrication of GaAs-AlGaAs photonic crystal nanocavities

Due to sub-100 nm dimensions and the requirement of near-vertical and smooth-etched facets, the fabrication process was expected to be challenging, requiring many

test samples. At the same time, Molecular Beam Epitaxial growth of III-V epitaxial layers with embedded quantum wells is also time consuming and requires highly skilled personnel. To avoid added cost of using these embedded quantum well samples for the optimization of the fabrication process, growth of similar wafer stack (as shown in figure 3.5), without the quantum well, was carried out at EPFL (Switzerland) using MBE system of Prof. Imamoglu. The wafer growth was performed by Prof. Antonio Badolato. These samples were then used for optimization of the E-beam lithography, plasma etching recipe and the post-processing.

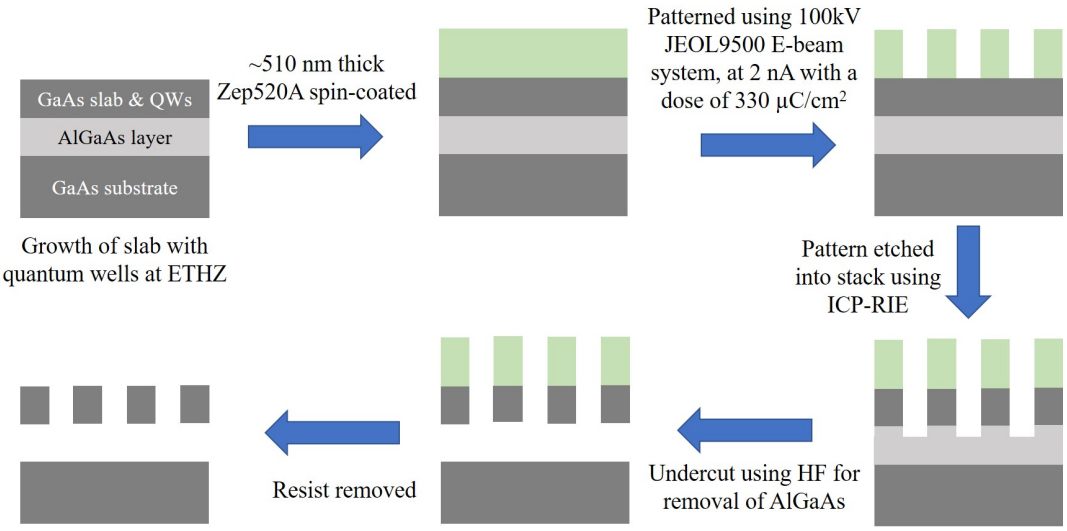

Figure 3.7: Schematic representation of the process flow used for the fabrication of III-V nanocavities. Samples were first coated with around 500 nm of Zep520a resist. The resist was then patterned by E-beam lithography and developed. The pattern was then transferred into GaAs layer by plasma etching. An undercut of $Al_{0.80}Ga_{0.20}As$ was then carried out using Hydrofluoric acid. The remaining resist was then removed, leaving behind the air-bridge nanocavity.

Figure 3.7 shows the overall fabrication process flow. MBE-grown wafer was diced into chips of roughly 1×1 cm. After cleaning the samples with acetone, IPA, and blow-drying them with nitrogen, the spin-coating with Zep520a—a positive-tone E-beam resist—was performed. Patterning was then done using E-beam lithography, followed by mask development and then ICP-RIE etching of GaAs-AlGaAs. After the etching was completed, the sacrificial layer of AlGaAs was removed using hydrofluoric acid (HF), for creating an air bridge. Finally the remaining resist was removed. The details of recipe discovery at each fabrication step are presented below.

3.3.1 Optimizing E-beam lithography recipe

The first step in the fabrication process was to develop an E-beam lithography recipe for the designed PC nanocavities. Our target hole radii ranged from 40 to 50 nm for different designs. It is very important to ensure the uniformity of the hole radii across the photonic crystal; furthermore, the circularity of the patterned holes also affects the nanocavity mode. In short, the aim of the E-beam lithography step is to pattern the resist with circular holes (cylinders, if considered in 3D) of uniform radii (as per the design). The uniformity of dimensions and how accurately a circle can be

patterned at such small scales (sub-100 nm) depends on the capability and stability of the E-beam lithography system. For this reason, we chose CNF nanofabrication facility for the fabrication of these devices with one of the best E-beam lithography tools in North America, a 100-kV Jeol 9500 system.

The photonic crystal patterns consist of holes etched into the slab, so, a positive E-beam resist was most suitable. Zep520a was chosen as it is considered one of the best E-beam resists for its high resolution, high sensitivity, dry-etch resistance, ease of development and reliability [90]. It is also known that Zep520a does not deteriorate after spinning and also after development, hence, the time between the spin-coating and exposure, as well as time between exposure and development, and the time between the development and etching become noncritical. Having said that, repeatability is imperative for any fabrication process, and it can only be achieved by following exactly the same procedure for each fabrication run. Hence, over the course of the fabrication process development in this work, the samples were spun, baked, exposed and developed without any long time delays, on the same day. Once the resist is developed, it becomes stable and can be used for etching when needed.

For E-beam lithography recipe development, once a resist has been selected, the next step is to decide the required resist thickness. The required GaAs etching depth was 140 nm, with the hole radii ranging from 40 to 50 nm, so, a suitable Zep520a thickness that can last the time required to etch these structures was established. We chose Zep520a thickness of around 500 nm. To achieve this resist thickness, a spinning recipe development was carried out. Test samples of 1 cm x 1 cm were first cleaned using acetone and IPA, followed by drying using nitrogen. Spin trials were then carried out on these samples, by varying the spin speed and then measuring the resist film thickness. The film thickness was measured using filmetrics F20 system (based on the principle of thin-film interference). The spinning recipe specified below has resulted in approximately 510-nm-thick Zep layer:

Spin-coating at 2200 rpm for 60 sec with a ramp of 300 rps, and baked at 170°C for 2 min.

Once the resist thickness and spinning recipe are finalized, the next step in E-beam lithography recipe development is the required clearing dose—the minimum electron energy required for clearing the E-beam resist for a given development time and feature size—is to be determined. To find the clearing dose for our patterns, we first had to fix the resist development process. The development of E-beam resist refers to the process in which the polymer is removed from regions that are not needed (for the case of a positive resist, from the exposed region). We used the commercial Zep520a developer, Zed50, which is an n-amyl acetate solution. Trials were performed to find the required time to completely remove the exposed areas. To remove the debris of the resist, MIBK-IPA (Methyl isobutyl ketone-Isopropyl Alcohol) mixture was used. The application of the mixture was followed by a rinse of the sample in IPA and by blow-drying it with nitrogen. The final development recipe used was as stated below:

45 sec in Zed50, 30 sec in MIBK:IPA = 1:3, and 30 sec in IPA, then blow-drying with N_2.

Once the development process was finalized, the dose test was then carried out, by sweeping the E-beam dose over a wide range (centered around the clearing dose numbers provided by the resist manufacturer). E-beam dose was varied from 200 to 400 $\mu C/cm^2$ in steps of 10 $\mu C/cm^2$. Cross-sectional SEM imaging was used to inspect the test samples and to determine the minimum dose value for which all

of the resist was cleared. Figure 3.8 shows three cross-sectional SEM images for determining the clearing dose. It can be seen that the dose values used for figure 3.8

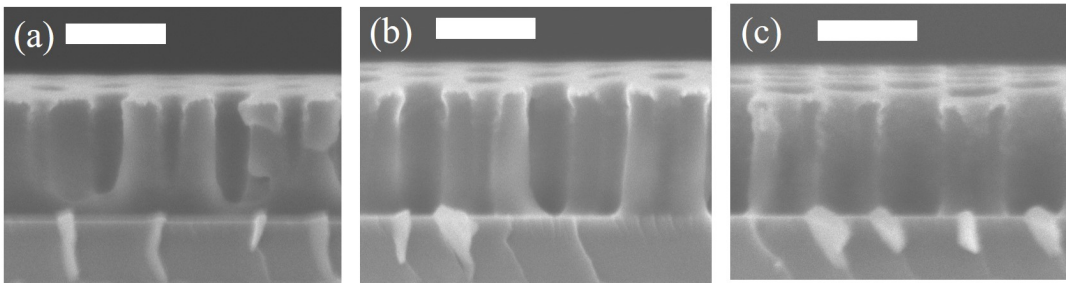

Figure 3.8: Cross-sectional SEM images showing the process adopted for determining the clearing dose for E-beam lithography. (a) and (b) are underexposed, hence, the resist is not completely removed, whereas (c) represents the case of clearing dose, as it is the minimum dose required to completely remove the resist. All scale bars represent 100 nm.

(a) and figure 3.8 (b) do not completely clear the resist; however, the dose used for the case of figure 3.8 (c) clears the resist completely. The dose tests have shown that the clearing dose was 330 $\mu C/cm^2$ for 510-nm-thick Zep520a, developed as stated above, for the feature sizes of our designs.

A Proximity Effect Correction (PEC) is another important aspect to be considered for E-beam lithography recipe development. PEC originates due to the forward-scattering of electrons in the E-beam lithography resist and backscattering of the electrons from the underlying substrate. The electron scattering leads to undesired exposure of regions, which otherwise, were not supposed to be exposed. This undesired exposure occurs in regions adjacent to those exposed by E-beam lithography (as per the intended design), leading to changes in the dissolution rate of the resist, and subsequently, changes the pattern from the intended design [91, 92]. This leads to a deviation of the shape as well as size of the pattern from the intended design and, therefore, it is not acceptable, especially for demanding patterns such as the ones required for this project. Periodic structures at close proximity suffer the most from the Proximity Effect.

The scattering of electrons, resulting in the proximity effect, has been shown to be a convolution of the E-beam dose distribution of a pattern with a proximity function [92, 93]. The proximity function—also commonly referred to as point spread function (PSF)—is radially symmetric and predicts how the electron energy is distributed throughout the E-beam resist, when a single point is exposed. Once this effect is modeled, it can be reduced or corrected by appropriate measures, including physical and/or software-based techniques [94]. For this work we modeled the PSF for our wafer stack and resist thickness using the commercially available software *Tracer*. The results were then applied as a correction, called PEC, to the original dose pattern using E-beam lithography file generator software *Beamer*. We did not observe any measurable difference between the patterns with and without PEC, as was inspected using SEM. This is primarily due to the fact that high voltage acceleration E-beam lithography systems (like the 100-kV system that was used in our studies) yield negligible scattering within the resist [94]. Nevertheless, PEC was used for the rest of the E-beam exposure in this project.

The finalized E-beam patterning recipe was then used for patterning PC nanocavity designs. Top-view SEM imaging was used to inspect the variation in the hole

radii and also circularity of the patterned holes. Images (such as the one shown in figure 3.9) were analyzed using scripts developed in *ImageJ* software, for statistical analysis of patterned samples. Table 3.1 shows the values of the patterned holes, as

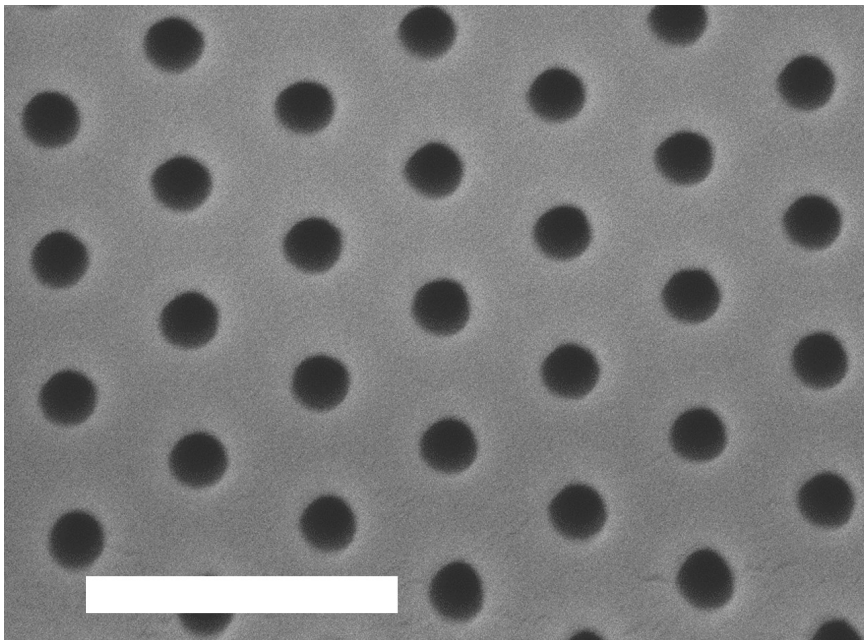

Figure 3.9: Top-view SEM image, representing one of the sample images used for analysis of hole-radii uniformity and circularity. Scale bar represents 500 nm.

observed using top-view SEM imaging. It can be seen that the actual hole size is larger than the target size (As designed in the E-beam CAD files). The variation in the hole radii was modest, with a standard deviation of 1.2 nm. It must be noted here that the target hole size is to be calibrated again, once an etching recipe is finalized, since etching further increases hole radii. This process of quantifying the required calibration is commonly called radius reduction test, by the photonic crystal experimentalists' community.

Table 3.1: The target radius as defined in the E-beam pattern CAD file, the measured radius after the development, as seen from the SEM top-view images, and the standard deviation (σ) of the statistical analysis of the hole radii using *ImageJ* script analysis on the top-view SEM images.

Target hole radius/(nm)	SEM top view mean radius/(nm)	σ/(nm)
44.0	49.5	1.3
46.0	54.5	1.2
48.0	63.4	1.2

3.3.2 Optimizing plasma etching recipe

Plasma etching for this project was extremely challenging, due to the small dimensions, three different materials within the wafer stack (GaAs, InGaAs and AlGaAs) and the etching depth requirement of minimum 140 nm with such small hole sizes. It

is important to recognize that small gaps result in very low etching rate and, hence, low selectivity. As an example of this reduced etching rate for small gaps, figure 3.10 shows the cross-sectional SEM image of an AlGaAs slot waveguide, that we etched in a single step. It can be seen from figure 3.10, that the etching rate is many times higher for the waveguides as compared to the small gap. Apart from this chal-

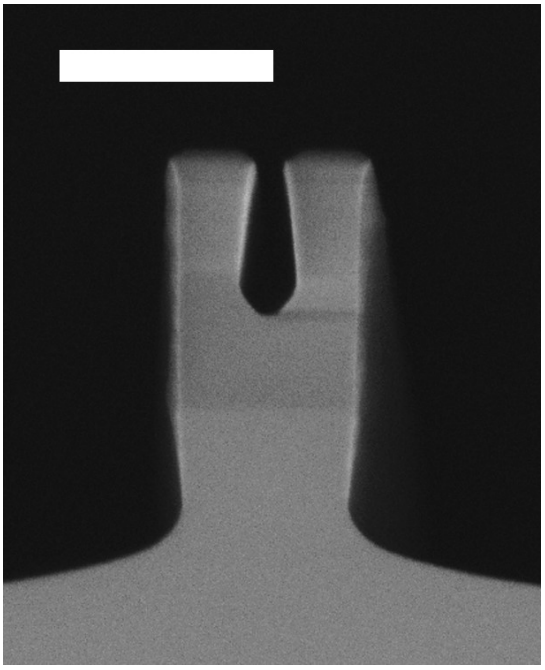

Figure 3.10: Cross-sectional SEM image of the plasma etching of an AlGaAs slot waveguide. The etching rate within the small gap is very low, compared to the etching rate of the larger waveguides. Scale bar represents 1 μm.

lenge of etching small gaps, this project was further complicated by the requirement of smooth and vertical sidewalls. To achieve such precise plasma etching, several etching test runs were required, for optimizing the process.

The etching recipe development was carried out at CNF (Cornell), using a PT770, ICP-RIE system. This tool was heavily used for a variety of III-V materials. This variation in materials results in variations in the chamber condition, leading to non-repeatability of developed recipes. a 10-minute Oxygen clean, followed by 10-minute conditioning, was a routine used before running the etching test. This was done to minimize chamber-condition variations. However, due to the requirement of a high-precision etching, we still observed that the recipes developed were not repeatable from day to day. To counter this problem further, the facility operators were requested for allocating blocks of time for developing this recipe, during which no other user had access to the system. As the recipe parameters were tuned, the chamber-condition did not vary, thus facilitating making the recipes as repeatable as possible.

One factor, overlooked by many plasma etching process developers (in an academic research setting), is the thermal effect on the etching rate and the recipe. We used small pieces of semiconductor chips for the etching tests, however, etching systems are built for wafer-scale etching. A 4-inch sapphire wafer was used for mounting these small chips using ultrahigh vacuum thermal gel. This gel helps in transferring heat from the chip to the underlying sapphire wafer, which is, in turn, cooled by the backing helium flow. The amount of gel, the size of the sample and its

position on the mounting wafer affect the heat transfer, which, in turn, leads to the variation in the chemical etching rate. There is no easy solution to this problem; the best thing that can be done is to use roughly the same-size pieces of semiconductor for the etching tests and the final samples. Furthermore, placing the samples at approximately the same location on the mounting wafer and using similar amount of gel for each etching run, can also help in keeping the thermal transfer consistent for all the etching runs, hence making the recipes as repeatable as possible.

During the etching recipe optimization, the etching chemistry was fixed as BCl_3:Cl_2 = (3:4) sccm, where chlorine was added to the recipe in order to achieve a higher etching rate and to improve the selectivity. Recipe discovery was done in a similar manner, as detailed in section 2.4.2, *i.e.*, while keeping all the parameters constant and observing the effect of the variation of one parameter at a time on the etching rate, the sidewall angle and roughness. Figure 3.11 shows SEM cross-sectional images of four different etching runs, carried out during the recipe optimization. The

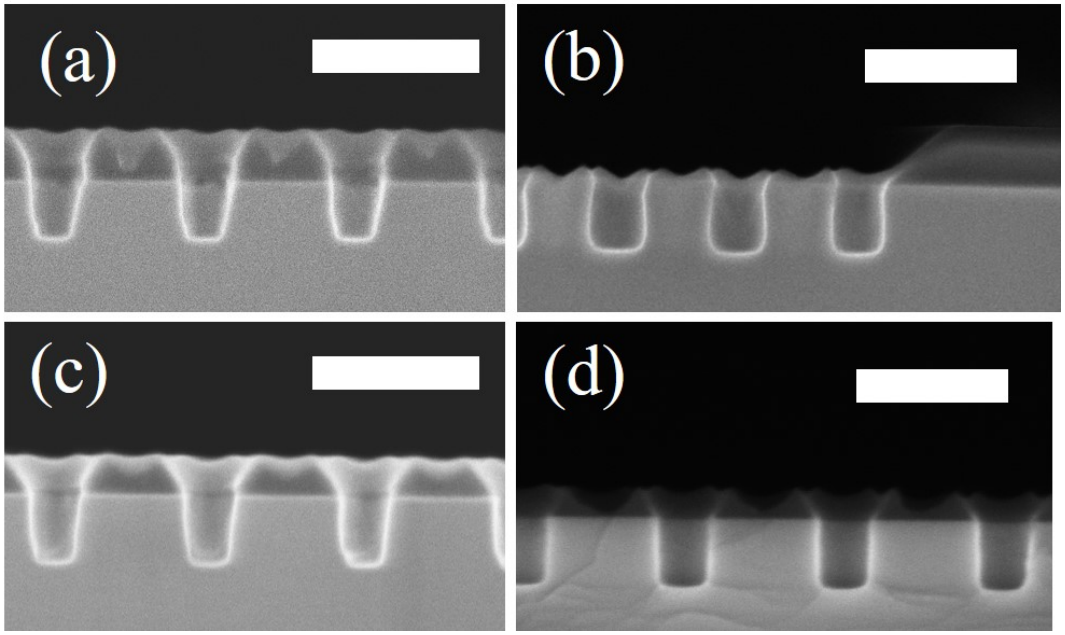

Figure 3.11: Cross-sectional SEM images of four different etching test runs. The examples illustrate the following situations: (a) Angled sidewalls, (b) some undercut, resulting in rounded profile at the base of the holes, (c) improved but still not nearly-vertical sidewall angle, (d) nearly-vertical smooth sidewalls and successful achievement of the minimum required etching depth of 140 nm. All scale bars represent 200 nm.

etching recipe used to obtain the result shown in Figure 3.11 (d) resulted in required etching depth, nearly-vertical and smooth sidewalls. This recipe was used for etching final samples, ICP-RIE parameters are as shown below:

BCl_3:Cl_2 = (3:4) sccm, ICP = 200 W, RIE = 100 W, P = 15 mT, time = 80 sec.

3.3.3 Post-processing

In order to produce the air bridge, undercut is to be performed as the post-processing step after the dry etching. The undercut results in the removal of the sacrificial layer, which is $Al_{0.80}Ga_{0.20}As$. Hydroflouric acid selectively attacks AlGaAs, removing it

from the GaAs substrate. This process is especially efficient when a high proportion of aluminum is present. Time trials were performed to determine the required time for completely removing sacrificial layer in a controlled manner. To have a controlled etching, a 10% HF solution in water was used. We determined from our trials that 90 seconds were sufficient in order to completely remove the 1-μm-thick $Al_{0.80}Ga_{0.20}As$ layer. A few earlier studies report that rinsing the sample with potassium hydroxide (KOH), after HF undercut, smoothens the undersurface of the slab and also removes any leftover debris. After multiple attempts to follow this suggestion we concluded in our finding that KOH does not improve the undercut profile. It rather worsens the smoothness of the underside of the GaAs slab. Figure 3.12 (a) shows the tilted cross-sectional SEM image of the GaAs slab after the undercut, whereas Figure 3.12 (b) shows the effect of treating it with KOH. It can clearly be observed that KOH post-treatment has resulted in some debris build up beneath the slab. Hence, KOH post-treatment was not used for the final samples.

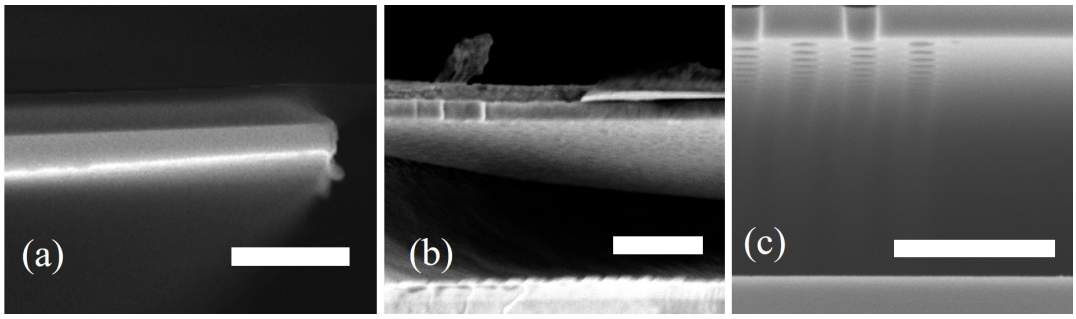

Figure 3.12: Tilted cross-sectional SEM images of the GaAs slab: (a) after HF undercut, (b) after post-undercut KOH treatment, and (c) after post-undercut resist removal

After the undercut has been performed, the slab is ready for optical characterization. However, in order to have air on both sides of the slab, we need to strip any remaining resist. In order to remove the developed Zep520a, we used 1165 Remover from *microposit*. It consists of a variety of organic solvents including N-methyl-2-pyrrolidine. As the final step of the fabrication process, the samples were kept in 1165 heated at 90 °C for 10 minutes. Figure 3.12 (c) shows the tilted SEM cross-sectional image of the GaAs slab after the resist removal. No leftover debris was observed, either on the top or on the bottom of the slab, hence, a pre-ashing or post-ashing (oxygen plasma etching, commonly used to remove resist debris) was not deemed necessary. To verify that ashing was not required indeed, ashing trials were carried out in order to observe whether there is any noticeable effect of ashing using SEM imaging. No difference was observed, hence, ashing was not used for the final samples.

3.4 Conclusion and further work

In this work we engineered a repeatable fabrication process—comprising E-beam lithography, plasma etching and wet-chemical post-processing—for GaAs PC nanocavities. Figure 3.13 (a) summarizes the final fabrication process used for the fabrication of GaAs PC nanocavities, and the final H1 and L3 fabricated samples, are shown in Figure 3.13 (b) and Figure 3.13 (c), respectively. The fabrication process was engineered from scratch and demonstrates etching profiles that are smooth and vertical, matching the required design dimensions. The optical characterization of these

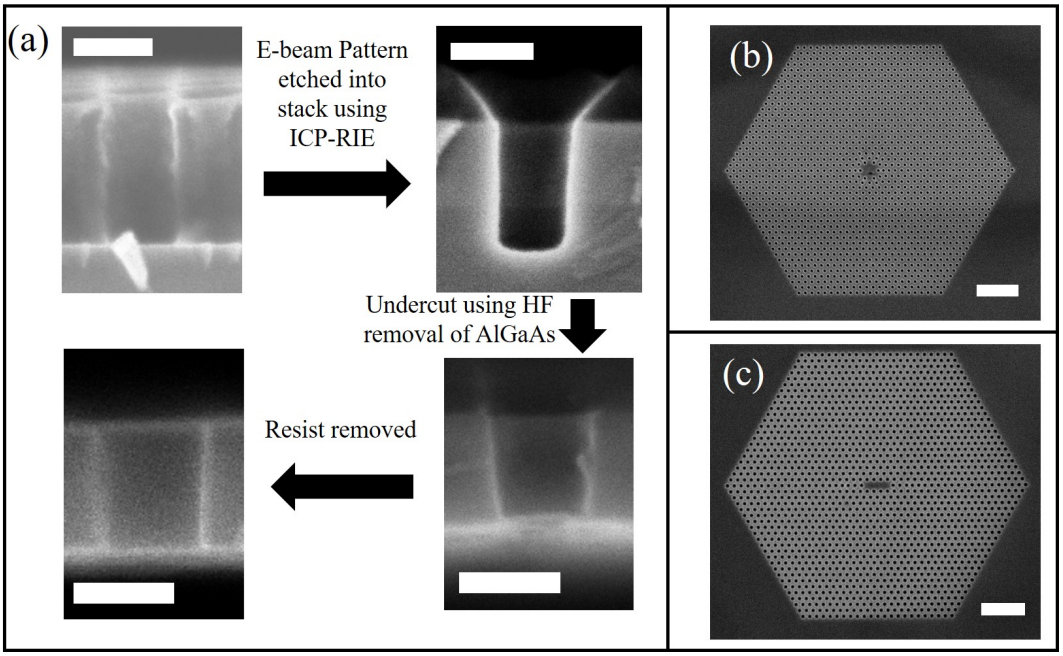

Figure 3.13: Summary of the overall fabrication process development. (a) Process flow summary with cross-sectional SEM images for each step. The scale bars represent 100 nm. (b) Top-view SEM image of the final fabricated H1 PC nanocavity, and (c) Top-view SEM image of the final fabricated L3 PC nanocavity. Scale bars for (b) and (c) represent 1 μm.

samples is currently in progress in Prof. Antonio Badolato's laboratory. This initial characterization will be helpful for optimizing the design and fabrication process before we repeat it for the wafer with embedded quantum well, leading to an on-chip polariton-blockade device.

Chapter 4

InGaAsP/InP waveguides for integrated nonlinear optics

Quaternary III-V semiconductor materials have been widely used for laser sources and detectors. However, their nonlinear optical properties remain largely unexplored, while the materials definitely hold promise for nonlinear photonics on-a-chip, owing to their exceptional properties: CMOS compatibility, strong nonlinearity and possibility of combining light sources, passive components and detectors on the same chip. In this work we experimentally study Indium Gallium Arsenide Phosphide (InGaAsP), for applications in integrated nonlinear optics—as a representative of quaternary III-V semiconductor materials.

In this project, I collaborated with Shayan Seidi and Lilian Sirbu, to design InGaAsP/InP strip-loaded waveguides for enhanced Kerr nonlinearity. The designed waveguides were then fabricated, with a detailed study of plasma etching of Indium-based III-V semiconductor compounds. The fabricated devices were then optically characterized, for the experimental demonstration of their nonlinear optical properties, in collaboration with Shayan Saeidi, Payman Rasekh and Alperen Tüğen.

4.1 InGaAsP: A quaternary III-V semiconductor

$In_xGa_{1-x}As_yP_{1-y}$ has the binary compounds GaP, GaAs, InAs, and InP in the basis. The parameters x and y represent molar fractions of In, Ga, As, and P. The relative concentrations of the pairs of elements represented by x and $1-x$, and by y and $1-y$, add up to 1. One can change the material compositions of the quaternary compounds through mutually adjusting the concentrations of the pairs of elements represented by x and $1-x$, and by y and $1-y$. One can clearly see that such a material has two degrees of freedom in x and y, and, hence, more flexibility in adjusting the optical characteristics as compared to ternary III-V semiconductors such as AlGaAs. The dependencies of the lattice constant and energy gap on the material compositions of ternary and quaternary semiconductor compounds can be found from Vegard's law [59], as detailed in subsection 2.2.3 earlier, using equation 2.11. Figure 4.1, reproduced from a 1981 paper by A. G. Foyt, shows the lattice constants and band-gap energies of $In_xGa_{1-x}As_yP_{1-y}$ [95]. The points represent the values of the lattice constants and band-gap energies of the binary semiconductors (as marked on the diagram), and the lines represent the interpolation of the corresponding parameters for ternary compounds, extracted using Vegard's law [59]. The areas bounded by the lines represent the corresponding parameter space for the quaternary compound, in this case $In_xGa_{1-x}As_yP_{1-y}$. The solid and dashed lines indicate direct and indirect band-gap compounds. The complete methodology used for optimized Kerr

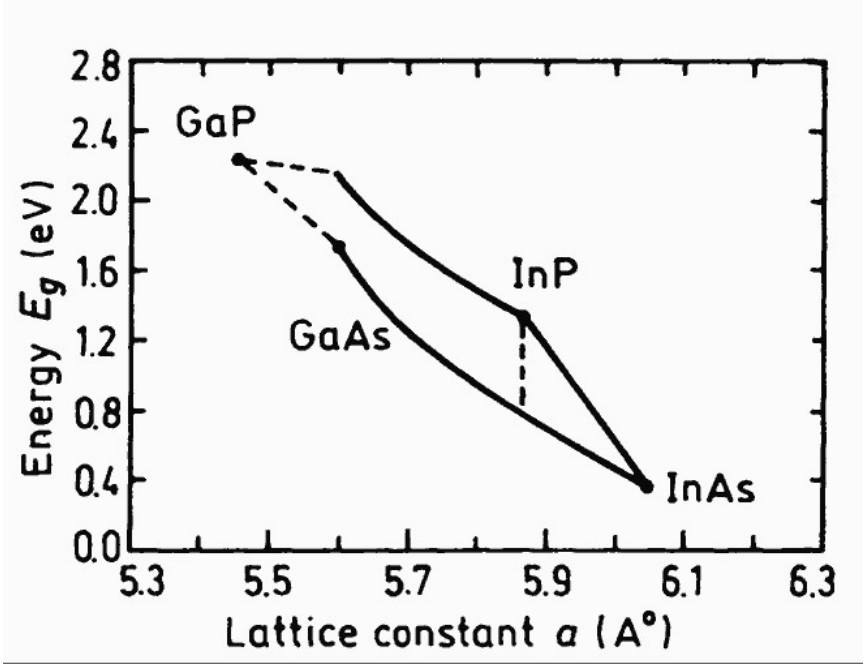

Figure 4.1: Lattice constants and band-gap energies of $In_xGa_{1-x}As_yP_{1-y}$ and constituent binary compounds [95].

nonlinearity in passive III-V quaternary waveguides can be found in our recently published design paper [33].

4.2 Waveguide designs

The first step of designing an integrated optical waveguide based on a III-V semiconductor is to define a layered arrangement that would include upper and lower claddings, and a guiding layer. The overall approach is similar to that outlined earlier, for the case of AlGaAs waveguides in Chapter 2. The wafer stack, comprised of the lower cladding, the guiding layer and the upper cladding, can be grown epitaxially, nearly defect-free, on top of an appropriate binary substrate that can be lattice-matched with the compositions of the layers. The lattice mismatch between different layers of a semiconductor structure could result in a poor-quality epitaxial growth, leading to a high defect density. The lattice mismatch $\Delta a/a$ of 0.06% (where a is the lattice constant and Δa is the difference between the lattice constants of the epilayers) for the growth of $In_{0.53}Ga_{0.47}As$ on InP substrate using liquid phase epitaxy (LPE) has been reported by Kuphal, *et al.* [96]. Similarly, Feng, *et al.* reported the lattice mismatch $\Delta a/a \simeq 0.4\%$ for the epitaxial growth of InGaAsP on InP substrate by supercooling technique study [97]. These evidences prove experimentally that InGaAsP can be grown on InP substrate, with a negligible lattice mismatch.

In order to identify the options for a substrate and lattice-matched layered arrangement, one can refer to the diagram in figure 4.1. One can select a specific binary substrate on which a quaternary compound will be grown; InP was selected as the substrate for InGaAsP strip-loaded waveguides. By selecting the substrate, we fixed the value of the lattice constant that the layers of our quaternary compound should match. The corresponding material compositions that are lattice-matched to the substrate, lie on the vertical line traced parallel to Y-axis of the graph through the point representing the selected substrate material in figure 4.1.

Table 4.1: Material parameters of InGaAsP wafer for strip-loaded waveguides

InGaAsP waveguides	Composition	E_g (eV)	λ_g (nm)	n
Upper cladding	InP	1.34	925	3.17
Guiding layer	$In_{0.63}Ga_{0.37}As_{0.8}P_{0.2}$	0.85	1459	3.58
Lower cladding	InP	1.34	925	3.17
Substrate	InP	1.34	925	3.17

Once the desired substrate material is selected, the next step is to identify the material compositions of the guiding layer and claddings for future wafer growth. A core layer with a composition $In_{0.63}Ga_{0.37}As_{0.8}P_{0.2}$ was selected to minimize two-photon absorption at longer wavelengths, and to ensure lattice matching with InP substrate. For increasing the refractive index contrast, we select InP as the lower and upper cladding material. Table 4.1 presents the material composition, refractive indices and band-gap of each layer of the designed wafer for InGaAsP/InP strip-loaded waveguides. Table 4.1 makes it clear that InGaAsP is not suitable for passive devices at the Telecom wavelengths; however, InGaAsP passive nonlinear waveguides can be used in combination with integrated InGaAsP lasers to extend their range of operation to longer wavelengths (2000 nm and beyond). Such sources can be of interest in spectroscopy and environmental sensing [98, 99], this was the main motivation of this study on the nonlinear optical properties of InGaAsP.

Once the wafer layer stack was finalized, waveguide simulations were carried out, using a design methodology similar to that outlined earlier in section 2.3 for the case of AlGaAs waveguides. Lumerical mode solutions was used to obtain waveguide parameters resulting in low A_{eff} and a single-mode operation in the wavelength range from 1.55 to 2.75 μm. Design iterations resulted in the waveguide dimensions as shown in Figure 4.2 (a). The mode evolution as we increased the wavelength from 1.55 to 2.75 μm is shown in Figure 4.2 (b).

4.3 Fabrication

As the first step in the fabrication process, the designed wafer layer stack was first commercially grown using Metalorganic Chemical Vapor Deposition (MOCVD). For the lithography part of the top-down fabrication process, the standard E-beam lithography was adopted. Initial attempts were made using 200-nm-thick hydrogen silsesquioxane (HSQ) as the mask; however, the mask was completely eroded before the required etching depth was achieved. A 500-nm-thick layer of Zep520a was then tested as an etching mask; however, that test failed as well due to running out of Zep520a mask before the required etching depth was achieved. These initial tests have shown that the etching recipe for InP has low selectivity. Hence, the required mask needs to be more etch-resistant than the aforementioned E-beam resists. Such etch-resistant masks are commonly known as hard masks. Silica was selected as the hard mask for this project, since it is etch-resistant to chlorine based etching recipes and also has higher melting (re-flow) point compared to polymer-based optical or E-beam resists. The further process was developed to pattern a hard mask using E-beam lithography.

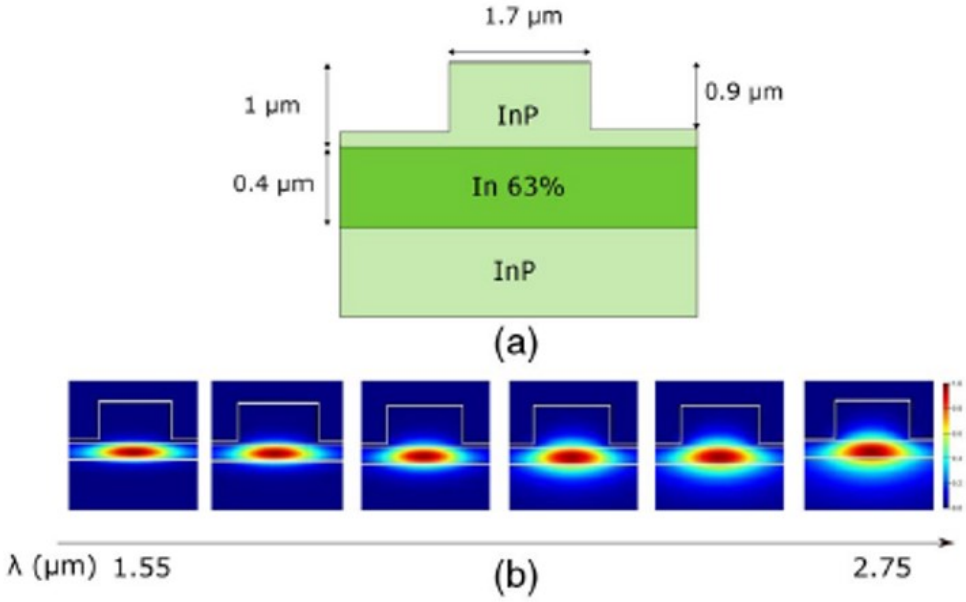

Figure 4.2: (a) Schematic of the designed InGaAsP strip-loaded waveguide with InP claddings and the composition of the guiding layer $In_{0.63}Ga_{0.37}As_{0.8}P_{0.2}$, (b) Intensity distributions of the fundamental TE mode of an InGaAsP strip-loaded waveguide with the width of $w = 1700$ nm at different wavelengths. The evolution of the fundamental TE mode is shown as the wavelength increases from 1550 to 2750 nm.

4.3.1 E-beam lithography for hard mask

HSQ—a negative-tone E-beam resist—was used for patterning the waveguides. As a first step, 1 cm $\times$ 1 cm chips were diced from the InGaAsP/InP wafer. They were then cleaned using acetone and IPA, and then were blow-dried using nitrogen. The chips were then coated with 300 nm of silica using an existing Plasma-Enhanced Chemical Vapor Deposition (PECVD) recipe. A 40-nm-thick layer of chromium was deposited on top of the silica layer by electron beam evaporation. XR-1541 (commercially available HSQ solution) was then spun coated at 1000 rpm for 60 seconds, with an acceleration of 60 rps, resulting in a 180-nm-thick resist layer.

The patterning of the coated wafer with waveguides was performed with a 100-kV Jeol 9500 electron beam lithography system, at CNF (Cornell). Based on the simulation results, the target waveguide width was 1.7 μm. However, in practice, it is very difficult to achieve the exact targeted waveguide dimensions in fabrication due to a variety of fabrication errors. That is why, waveguide patterns with the widths ranging from 1.1 to 2.1 μm, with a step size of 0.1 μm were used in order to ensure that there is at least one width that corresponds to the design. In addition, operating with a range of waveguide widths can help one to experimentally verify that 1.7-μm-wide waveguide has, indeed, the best experimental performance. HSQ was exposed using an E-beam dose of 950 $\mu C/cm^2$. The resist was then developed for 10 min in MIF 300 solution (2% solution of Tetramethylammonium hydroxide in water developed by *Merck*). The development was followed by a rinse in running de-ionized water, then by blow-drying with nitrogen gas. Once developed, the HSQ mask was cured at 170 °C for 1 hour, to enhance its etch resistance. HSQ mask was then used to transfer the waveguide pattern into underlying chromium layer using ICP-RIE process. Next, the etching of the chromium and then silica layers was

performed, and the waveguide pattern was transferred into the silica layer. Finally, the silica mask was used to transfer the waveguide pattern into InP layer. Etching test samples were patterned using this process, as summarized in figure 4.3, to optimize ICP-RIE process for InP. Once the etching test samples were patterned, ICP-RIE process was then developed for InP.

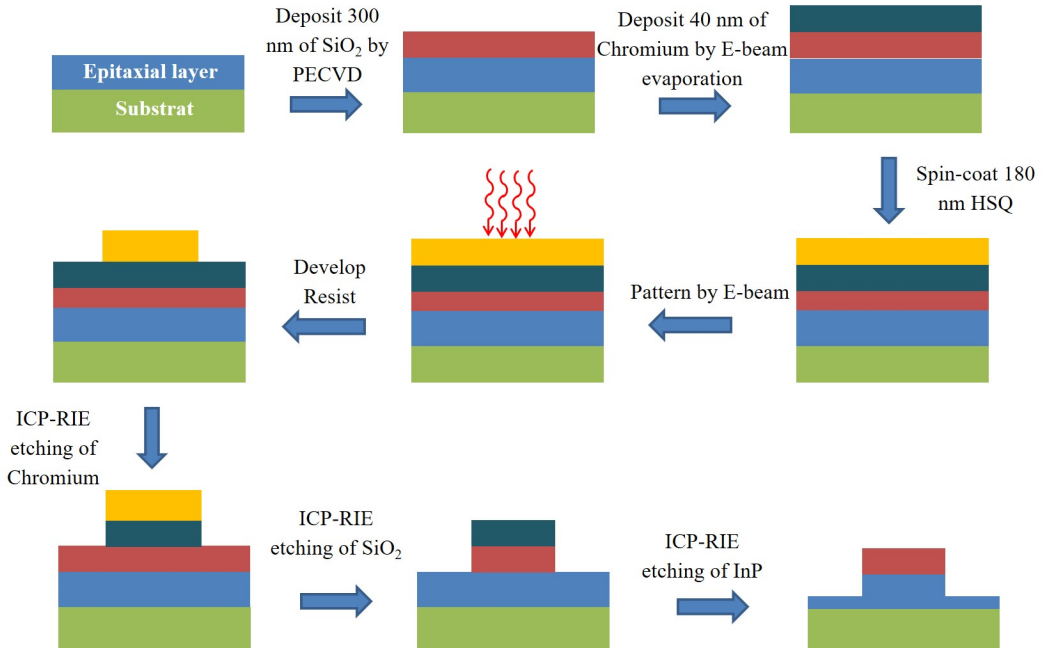

Figure 4.3: The developed fabrication process flow for strip-loaded InGaAsP/InP waveguides.

4.3.2 Low-temperature etching of InGaAsP/InP

Plasma etching of semiconductors containing indium is known to be challenging [100, 101]. The majority of the reported studies on InP plasma etching used high temperatures of the substrate—ranging from 120 °C to over 200 °C—to achieve high etching rate and sidewall verticality of InP [100, 101]. However, the ICP-RIE system for III-V semiconductors at CNF (where the devices for other projects were fabricated) does not have the capability of substrate heating. A more detailed literature survey has brought up a study reporting room-temperature etching of InP using Methan-Hydrogen-Chlorine (CH_4-H_2-Cl_2) etching chemistry for the etch rates close to 1 μm/min [102]. Plasmatherm770 ICP-RIE system at CNF had all the required gases, so, the etching trials were performed, starting with the same etching parameters as outlined in the earlier study [102]. The total of 15 etching trials were carried out with the etching parameters varying in a broad range; however, for all the parameter sets the etching rate was very low, unlike what was reported in the earlier study [102]. The reason has been discussed profoundly in other literature sources, linking low etching rate of Indium-based semiconductors at low temperatures to the fact that the etching by-product, $InCl_x$, is not volatile unless the substrate is heated to 150 °C.

4.3.3 Plasma-heated etching of InGaAsP/InP

Since the CNF III-V etcher has no heating capability for substrates, we attempted to elevate the substrate temperature using plasma heating [103]. An etching test sample was placed on a sapphire mounting wafer, but no ultrahigh vacuum thermal gel was placed between the sample and the backing wafer. This has resulted in the reduction of heat dissipation from the sample; hence, in a temperature increase and enhanced $InCl_x$ removal. We did observe an increase in the etching rate, owing to the plasma-heating of InP, however, the results were not repeatable, and the achieved etching depth was still lower than the targeted value 0.9 μm. Therefore, this method was deemed inappropriate for the final sample. Figure 4.4 (a) shows the SEM cross-sectional image of one of the etching trials performed at room temperature with CH_4-H_2-Cl_2 etching chemistry, whereas Figure 4.4 (b) shows the SEM cross-sectional image of the etching performed at an elevated temperature using plasma heating.

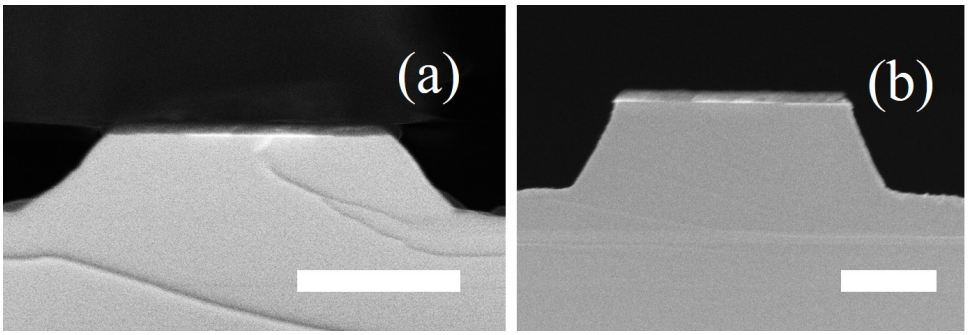

Figure 4.4: Cross-sectional SEM images of etching tests using CH_4-H_2-Cl_2 chemistry: (a) Etching done at room temperature, and (b) Etching at elevated temperature, using plasma-heating. All scale bars represent 500 nm.

Searching for an alternative fabrication facility that could provide heating option for etching, we came across Quantum Nano Centre (QNC), Waterloo. QNC has an oxford plasma ICP-RIE system, capable of heating the substrate up to 60 °C. Furthermore, the helium cooling of the mounted substrate can be turned off, allowing further increase in the substrate temperature. The etching trials were then carried out at QNC using this plasma heated etching strategy. Twelve etching trials were carried out while tuning the etching parameters in a similar manner as described in earlier chapters. An acceptable etching recipe was then fine-tuned and used for the final InGaAsP/InP strip-loaded waveguide sample. Figure 4.5 shows SEM cross-sectional images and atomic force microscopy (AFM) scans of two of those etching trials. An improvement in the sidewall angle and in the roughness of the etched profile can clearly be seen from the two AFM scans. A detailed analysis of the ICP-RIE parameter sweep is not presented here, since we are planning to publish it first, as we are not aware of any systematic study of plasma-heated etching of InP in literature. After etching the final sample, the sample was cleaved in preparation for the optical characterization. The final sample containing InGaAsP/InP strip-loaded waveguides was etched using ICP-RIE recipe as shown below:

CH_4:H_2:Cl_2 = (4:7:8) sccm, ICP = 2000 W, RIE = 65 W, P = 4 mT, time = 82 sec.

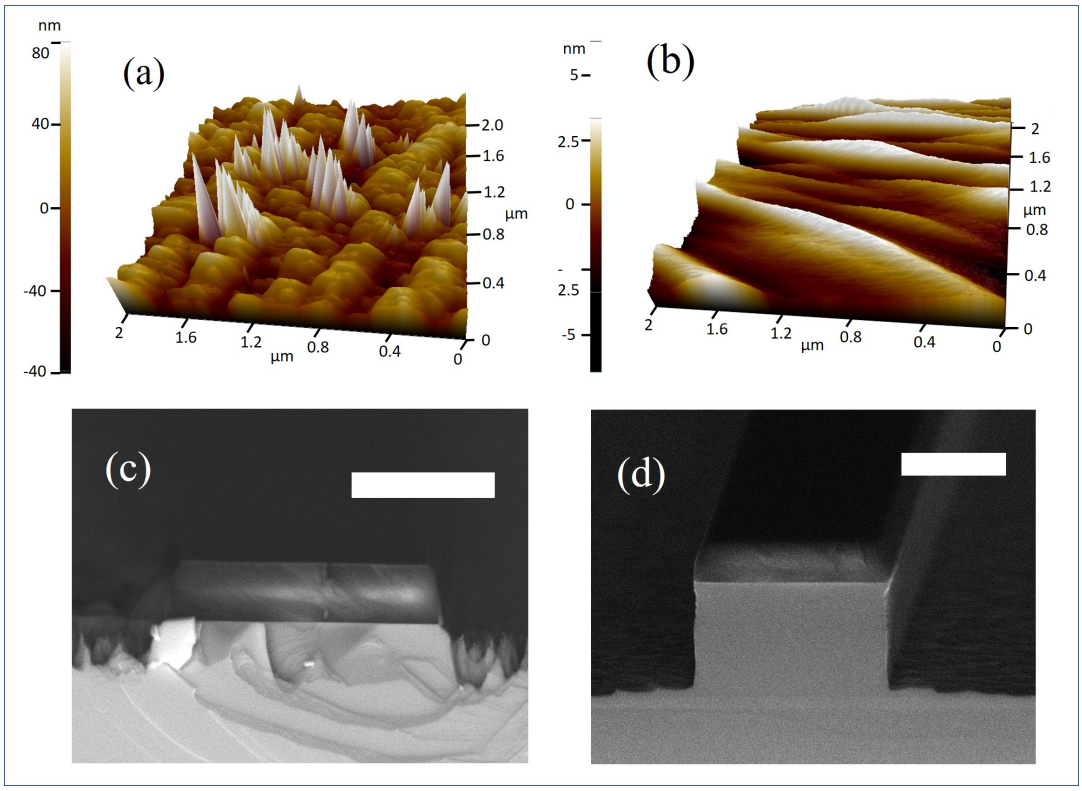

Figure 4.5: Cross-sectional SEM images of the etching tests with CH_4-H_2-Cl_2 chemistry: (a) AFM scan of the initial etching trial of InP, showing a high surface roughness induced by the etching. Its cross-sectional SEM image is shown in (c). (b) AFM scan of an etching trial of InP after parameter improvement, showing significantly reduced surface roughness. Its cross-sectional SEM image is shown in (d). All scale bars represent 500 nm.

4.4 Optical characterization

Fabrication of InGaAsP/InP strip-loaded waveguides was followed by their optical characterization. Propagation loss was measured first, and then nonlinear optical characterization was performed. Two-photon absorption measurements, self-phase modulation and four-wave mixing results are presented in this thesis.

4.4.1 Optical propagation loss measurement

The first step in assessing the performance of an integrated optical device is the propagation loss measurement. Overall optical loss can be obtained by taking a ratio between the measured optical power at the output and at the input to the waveguide. The overall loss—comprised of the propagation loss L_{prop}, the coupling loss due to the mode size and shape mismatch between the free-space focused laser beam and waveguide mode L_{coupl}, and the Fresnel reflection loss L_{ref}—was measured to be around 18 dB. The propagation loss was measured using the Fabry-Perot loss measurement technique, as described in detail in section 2.5 [70]. The corresponding measurement setup is shown in Figure 2.32. The measured values of the propagation loss were around 2.7 dB/cm for the fundamental TE mode, and 2.4 dB/cm for the fundamental TM mode of a 1.7-μm-wide waveguide.

4.4.2 Two-photon absorption measurements

The nonlinear optical characterization was carried out in collaboration with Payman Rasekh and Shayan Saeidi. The schematic of the experimental setup used to carry out nonlinear optical characterization of InGaAsP/InP waveguides is shown in Figure 4.6. The four-wave mixing (FWM) experiments require two laser sources:

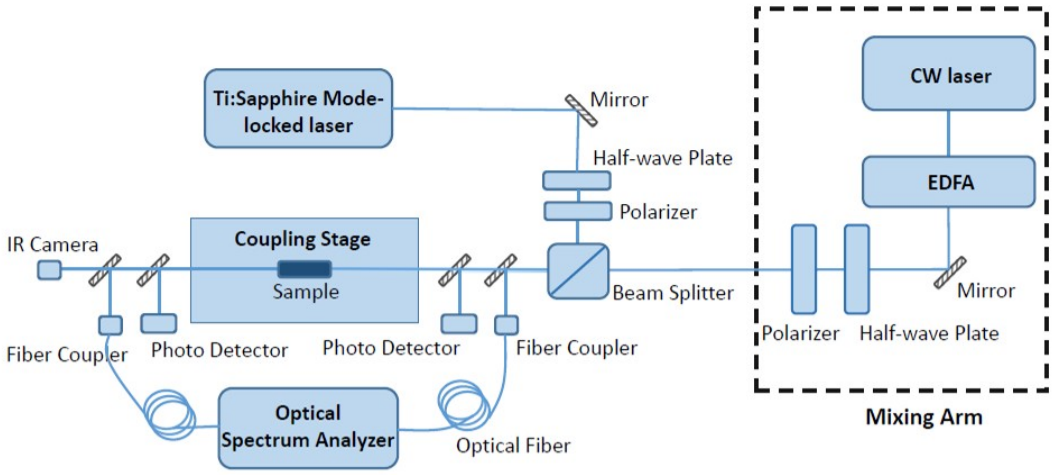

Figure 4.6: Experimental setup used for the nonlinear optical characterization of InGaAsP/InP waveguides. The whole setup, as displayed here, was used for FWM experiments, while TPA and SPM measurements were performed without the optical arm highlighted by the dashed box (the "Mixing Arm", that contains cw laser).

a pulsed pump laser and a cw signal laser. Self-Phase modulation (SPM) and Two-Photon absorption (TPA) measurements require only a pulsed laser, so, the cw laser arm, as shown in the setup schematic with a dashed box, was not used for TPA and SPM. The nonlinear optical setup is further described below.

We used two laser sources in our FWM experiments: a high-peak-power pulsed pump and an amplified tunable cw signal. The pump was obtained from the optical parametric oscillator (OPO), pumped by a mode-locked Ti:Sapphire laser with a repetition rate of 76 MHz. The system produced a pulsed output at 1570 nm with the pulse duration of 3 ps. The cw signal was obtained from a combination of a tunable low-power cw laser and a high-power (up to 2 W) erbium-doped fiber amplifier (EDFA), operating in the wavelength range between 1535 and 1565 nm. In each of the pump and the signal optical arms, a combination of a half-wave plate and a linear polarizer was used to independently control their polarizations. The pump and signal beams were combined at a 50% non-polarizing beam splitter, and were coupled into the waveguide using butt-coupling with a 40× microscopic objective. We used a Xenics infrared camera to observe the mode profile at the output of the waveguide. The optical power was measured by the detectors with power meters, and the spectra at the input and output of the waveguide were recorded using a Yokogawa AQ6370 optical spectrum analyzer.

In order to measure the two-photon absorption coefficient of the InGaAsP/InP waveguide, we used the nonlinear transmission (NLT) method, also known as nonlinear absorption experiment [104]. Following that method, the power transmitted by the waveguide was measured as a function of the optical power at the waveguide's input. The results are shown in Figure 4.7 (a), where we plot the transmitted power as a function of the average power launched into the waveguide for both

TE (asterisks) and TM (triangles) polarizations. The characteristics at higher input

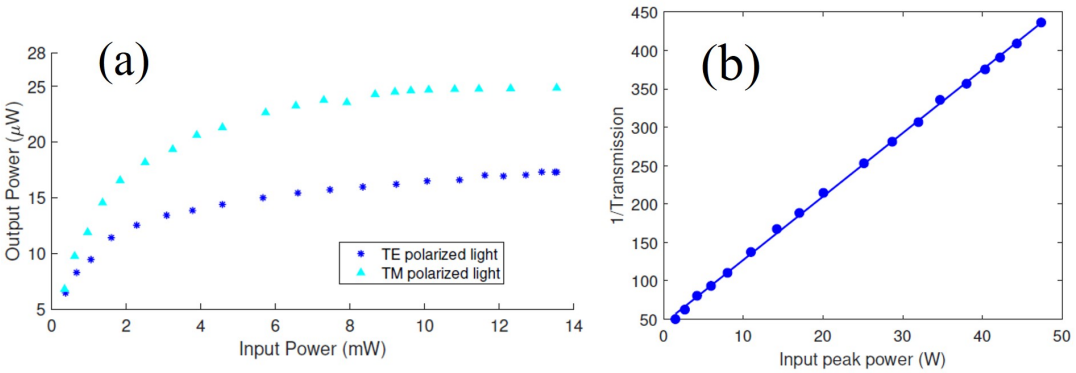

Figure 4.7: (a) Output vs. input power for TE and TM polarized light. One can see the saturation behavior due to nonlinear absorption. (b) The TPA coefficient α_2 can be obtained by the best line fit to the experimental data (Gradient of the line fitted to experimental data points.

powers are largely nonlinear, which indicates the presence of nonlinear absorption. Since we have been operating above half-band-gap (the wavelength 1568 nm falls within the region of strong two-photon absorption because the value of the band-gap wavelength corresponds to 1450 nm), this observation is intuitive.

In order to extract the value of the TPA coefficient α_2 from our measurements, we start with the equation for the intensity evolution in a medium with TPA [105]

$$-\frac{dI}{dz} = \alpha I + \alpha_2 I^2. \tag{4.1}$$

Here α represents the linear absorption coefficient, and I denotes the intensity. This equation is satisfied by

$$\frac{1}{T} = e^{(\alpha L)} \left(\frac{L_{\text{eff}}}{A_{\text{eff}}} \alpha_2 P_{\text{in}} + 1 \right), \tag{4.2}$$

where T refers to the power transmission ratio ($P_{\text{out}}/P_{\text{in}}$), $L_{\text{eff}} = [1 - \exp(-\alpha L)]/\alpha$ is the effective length, L is the length of the sample, and A_{eff} is the effective mode area defined as

$$A_{\text{eff}} = \frac{\left[\int_{-\infty}^{\infty} \int_{-\infty}^{\infty} |E(x, y|^2 \, dx \, dy \right]^2}{\int_{-\infty}^{\infty} \int_{-\infty}^{\infty} |E(x, y|^4 \, dx \, dy} \tag{4.3}$$

in terms of the electric field $E(x, y)$ for the third-order nonlinear optical interactions [106]. The values of the effective mode area were obtained from the modal analysis performed with *Lumerical Mode Solutions* and correspond to $A_{\text{eff}} = 1.64\ \mu\text{m}^2$ for the fundamental TE mode and $A_{\text{eff}} = 1.10\ \mu\text{m}^2$ for the fundamental TM mode at the wavelength 1568 nm. The TPA coefficient can be obtained by measuring the power transmission ratio for different values of the input power and fitting it with equation 4.2. In Figure 4.7 (b), we plot the reciprocal transmission as a function of the coupled-in peak power (the peak power right at the entrance to the waveguide). The experimental data are shown in Figure 4.7 (b) with points, while the line represents the best linear fit to the data. The gradient of the line fitted to the experimental data points is proportional to α_2. The calculated value of the TPA coefficient is $\sim$ 15 cm/GW, which is approximately one quarter of the corresponding value reported for InGaAsP/InP multi-quantum-well waveguides [107]. This discrepancy

can be attributed to the fact that the density of states in quantum wells near the band edges is larger compared to that of a bulk semiconductor material. Moreover, due to the difference in the material compositions in the two studies, one cannot expect TPA coefficients with exactly the same values from the two measurements.

4.4.3 Self-phase modulation

After TPA, self-phase modulation experiments were carried out. The objective was to achieve a large nonlinear phase shift. For this experiment, we used the pulsed laser source only. We have performed the measurements of the spectra collected at the output of the waveguide at different levels of the incident power as shown in Figure 4.8. The legend in the figure shows the values of the coupled-in peak power

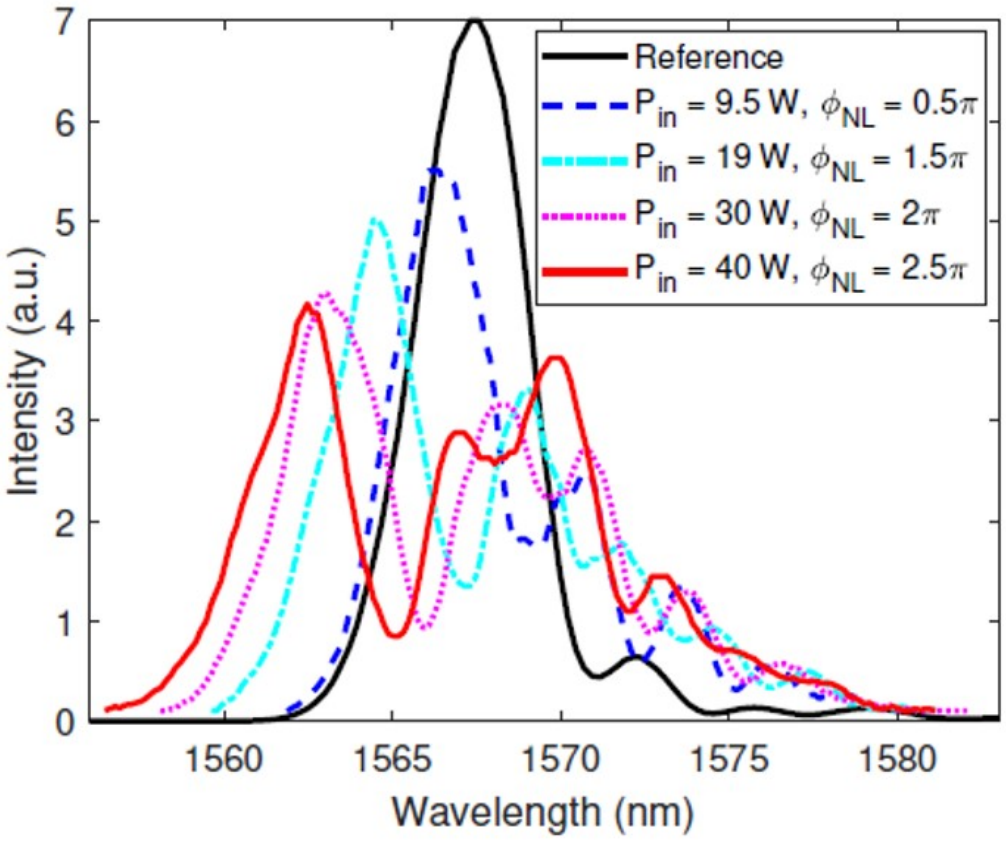

Figure 4.8: Spectral broadening and the nonlinear phase shift acquired by the beam propagated through the waveguide due to self-phase modulation. The legend shows the coupled-in power values and the estimated values of the nonlinear phase shift ϕ_{NL} next to the curves representing the corresponding spectra.

and estimated nonlinear phase shift next to the lines representing the corresponding spectra [108]. The spectral broadening with the increase of the incident power, that represents the manifestation of SPM, can be clearly observed from the graph. The maximum nonlinear phase shift that we were able to observe at 40 W of the coupled-in peak power was $\phi_{\mathrm{NL}} = 2.5\pi$, as estimated from the observed spectral characteristics at the output of the waveguide [108]. Despite the strong TPA, nonlinear phase shift is significant and indicates the presence of strong Kerr nonlinearity.

Indeed, based on our estimates of the phase shift, and using

$$\phi_{\mathrm{NL}} = n_2 k_0 L I \tag{4.4}$$

that relates the nonlinear phase shift ϕ_{NL} and the Kerr coefficient n_2 for SPM, we obtain the value $n_2 \approx 10^{-13}$ cm^2/W for our waveguide [50]. This compares well with the reported values $n_2 = 1.5 \times 10^{-13}$ cm^2/W for $Al_{0.18}Ga_{0.82}As$ [106], which has been proved to be an efficient material for nonlinear photonics, and silicon $n_2 = 4.2 \times 10^{-14}$cm^2/W at the telecom wavelength [109].

We now have sufficient information in order to characterize the nonlinear optical performance of the InGaAsP/InP strip-loaded waveguides in terms of the figure of merit F, expressed as [61]

$$F = \frac{n_2}{\lambda_0 \alpha_2}, \tag{4.5}$$

and the nonlinear coefficient γ, defined as

$$\gamma = \frac{2\pi\, n_2}{\lambda_0\, A_{\mathrm{eff}}}. \tag{4.6}$$

The figure of merit characterizes the potentials of the material itself for the nonlinear optics at the specific wavelength λ_0, while the nonlinear coefficient describes the performance of the nonlinear optical waveguide characterized by its effective mode area A_{eff} at the wavelength λ_0. The nonlinear optical performance of a waveguide is best when both the parameters are maximized, which can be achieved by a proper selection of the material (for the figure of merit), and by a proper design of the waveguide (for the nonlinear coefficient). For a nonlinear material to be considered efficient, the condition $F > 1$ must be satisfied. Based on the measured and estimated values of n_2 and α_2 in our experimental study, InGaAsP has $F \approx 0.043$, which is consistent with the fact that the operation wavelengths 1530–1570 nm fall within the range of strong two-photon absorption. The nonlinear coefficient $\gamma \approx 36.85$ m^{-1}W^{-1}, characterizing the performance of the InGaAsP/InP waveguides as nonlinear devices, is almost three times larger than that of similar devices based on AlGaAs [51]. This can be attributed to the fact that we have designed our InGaAsP/InP waveguides in a way that their effective mode area is minimized to the level of under 2 μm^2, compared to the values over 4 μm^2 reported in [51]. It is thus possible to exploit the full potential of such waveguides by a proper selection of the operation wavelength which, in our case, should be close to 2 μm.

4.4.4 Four-wave mixing

As the final step in our nonlinear optical characterizations, we have performed FWM experiments with our InGaAsP/InP waveguides. In this experiment, the whole setup as shown in Figure 4.6, including both laser sources, was used. The pulsed pump and amplified cw beams were mixed at the beam splitter, and then were free-space-coupled into the waveguide. The values of the coupled-in power at the waveguide's entrance were estimated to be 9 W for the peak power of the pump, and 0.5 W for the average power of the cw signal. The pump laser wavelength in our experiment was centered around 1568 nm, while the cw signal, amplified with an EDFA, was tuned in the range between 1545 and 1560 nm.The spectrum at the output of the waveguide had an extra frequency component generated by the process of four-wave mixing where two pump photons with the frequency ω_{p} and one

signal photon with the frequency ω_s interacted with the nonlinear optical medium to give rise to a single idler photon with the frequency ω_i: $2\omega_p - \omega_s = \omega_i$.

In Figure Figure 4.9, we show the results of the spectral measurements for different wavelength combinations of the pump and the signal. The generated idler peaks

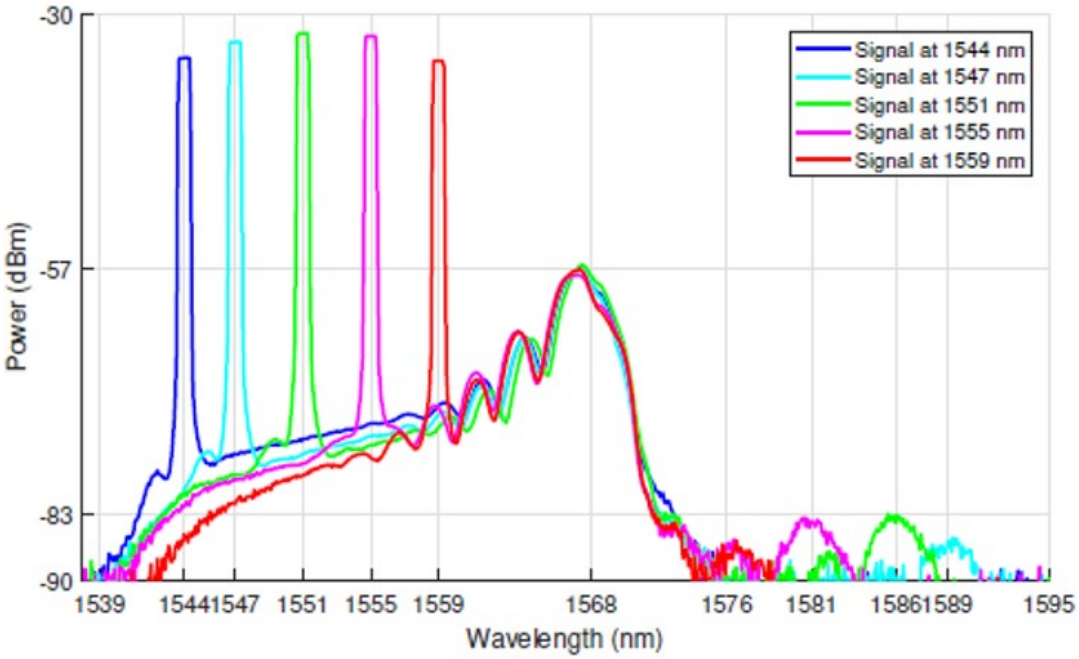

Figure 4.9: Wavelength conversion by FWM for pump wavelength fixed at 1568 nm and different cw signal wavelengths (narrow peaks on the left side). The generated idlers, corresponding to cw peaks, can be seen on the right side (at longer wavelengths). For the signal at 1551 nm (green), one gets the strongest idler. As the signal goes far from this wavelength, the conversion efficiency decreases.

corresponding to different cw signal peaks can be seen on the longer-wavelength side with respect to the pump. The results displayed in Figure 4.9 were obtained for the fundamental TM modes (for both pump and signal beams): similar effect has been observed for the fundamental TE mode, but the FWM efficiency was lower in this case due to the fact that the TE mode has a larger effective mode area and, hence, exhibits a smaller nonlinear coefficient.

The characteristics that we have observed in our experiment are comparable to those demonstrated with AlGaAs waveguides of similar geometry [51]. The overall conversion range (the difference in wavelength between the maximally separated signal and idler spectral components) was $\lambda_i - \lambda_s = 45$ nm, limited by the material dispersion which is the dominant dispersion mechanism in strip-loaded waveguides [51]. Indeed, the material dispersion of InGaAsP in the vicinity of 1568 nm is $D_{mat} = -19500$ ps/nm/km, while the simulated overall dispersion with the waveguide contribution taken into account is around $D_{tot} = -17200$ ps/nm/km. The latter value is only slightly offset with respect to the very high value of the material dispersion and lends to the characteristic dispersion length, defined as

$$L_D = \frac{T_0}{D_{tot}\,\Delta\lambda_{max}} \tag{4.7}$$

in terms of the pulse duration T_0 and maximum wavelength separation between the

pump and signal $\Delta\lambda_{max} \approx 22$ nm, comparable with the length of the waveguide. The waveguides have the length $L = 5$ mm, while $L_D \approx 8$ mm. The lack of dispersion management in our devices thus contributes to the very low efficiency and limited tuning range of the FWM process.

We next estimate the FWM conversion efficiency obtained in our experiment. Here we define the conversion efficiency as the ratio between the generated idler power and the output cw signal power, estimated from the spectral measurements. Here, the maximum conversion efficiency of ~ -50 dB was achieved. As a comparison, the value of -38 dB has been reported for AlGaAs nanowires with engineered dispersion, ultracompact mode with $A_{eff} < 1\ \mu m^2$, and managed two-photon absorption [34].

4.5 InGaAsP/InP nanowire waveguide fabrication

As discussed extensively in Chapter 2, nanowire waveguides enhance nonlinear Kerr effect due to the higher intensity of light (arising from lower A_{eff}). Furthermore, nanowire waveguides can be dispersion-engineered, leading to enhanced FWM due to better phase-matching. Nanowire waveguides were designed and patterned using the fabrication process described in figure 4.3. Fabrication tests were recently carried out, using in-house SAMCO ICP-RIE system at CRPuO (uOttawa). This etching system had an added feature of substrate heating. Initial trials were done at varying temperatures and etching parameters. Figure 4.10 (a) shows the schematic of the design of InGaAsP/InP nanowires, whereas Figure 4.10 (b) and (c) show two etching trials performed at different temperatures using the following etching recipe:

Cl_2:BCl_3:Ar = (1:2.5:1) sccm, ICP = 60 W, RIE = 20 W, P = 0.20 Pa, time = 4 min.

It can be clearly seen from Figure 4.10 that heating the substrate results in reduction of etching-induced roughness, as well as improves the selectivity and etching rate of InP. More trials are presently being performed to optimize the process further, and to fabricate the final InGaAsP/InP nanowire samples for optical characterization.

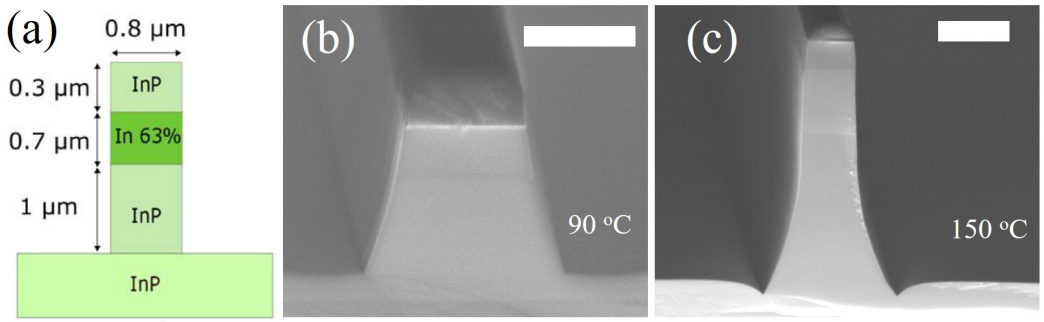

Figure 4.10: (a) Schematic representation of the designed InGaAsP/InP nanowire waveguide. Cross-sectional SEM image of etching trial for InGaAsP/InP nanowire waveguides carried out at a temperature of (b) 90 °C, and (c) 150 °C. All scale bars represent 500 nm.

4.6 Conclusion and future work

In conclusion, this was an exhaustive study encompassing design, fabrication and optical characterization of InGaAsP/InP waveguides. Figure 4.11 provides a picture summary of the fabrication process, showing the hard mask patterning followed by three different approaches for InP plasma etching, explored in this work. we report

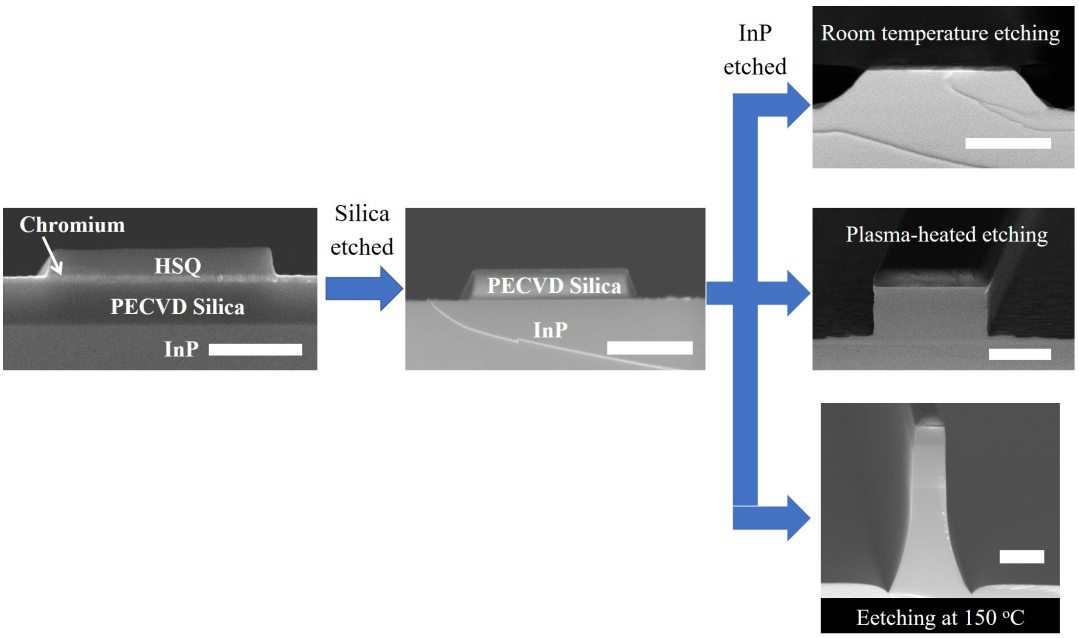

Figure 4.11: Summary of the fabrication processes developed for InGaAsP/InP waveguides. All scale bars on the cross-sectional SEM images represent 500 nm.

on the first measurements of the nonlinear absorption coefficient, self-phase modulation and four-wave mixing in InGaAsP/InP strip-loaded waveguides. We have observed the nonlinear phase shift of 2.5π in our SPM experiments, and the overall FWM conversion range of 45 nm, limited by the material dispersion and strong two-photon absorption. The TPA coefficient value was measured to be 15 cm/GW. Despite the presence of this loss mechanism, the nonlinear optical performance of our devices was comparable to that of the better-studied AlGaAs waveguides with a similar geometry [51]. This study represents the first set of proof-of-principle experiments aiming at demonstrating the pontentials of InGaAsP for nonlinear photonics on-a-chip. The next step would be the follow-up study performed at longer wavelengths such that the effect of TPA can be mitigated. This would allow one to exploit the full potential of InGaAsP for passive nonlinear optical waveguides capable of demonstrating wavelength conversion in the frequency range beyond 2 μm.

As a future goal, we are working on the optimization of the nanowire plasma etching process, for fabrication of InGaAsP nanowire waveguides, and, subsequently, intend to optically characterize InGaAsP integrated optical waveguides with engineered dispersion in order to expand the FWM wavelength conversion window [33]. Such waveguides, combined with integrated InGaAsP lasers, can open new spectral windows for all-optical signal processing and on-chip spectroscopy applications.

To conclude, the reported study has confirmed that III-V semiconductors are well suited for nonlinear photonics. The abundance of different kinds of III-V semiconductors indicate that these materials can constitute a bank of excellent nonlinear

optical platforms covering the entire spectral window between UV and IR.

Chapter 5

GaN waveguides on (-201)-oriented β-Ga_2O_3 substrate

5.1 GaN: a wide band-gap semiconductor

Gallium Nitride (GaN), a wide-band-gap (band-gap energy of 3.4 eV for Wurtzite GaN) semiconductor with high electron velocity and chemical and thermal stability [110], has attracted immense research interests for its many commercial applications, such as solid-state lighting, high-power and high-frequency electronics, and blue semiconductor lasers [2, 111–113]. Similar to other III-V semiconductor platforms [34, 42, 43], high-optical-quality GaN is also expected to become a suitable candidate for integrated nonlinear photonic circuits for a wide range of applications spanning from all-optical signal processing to quantum computing. Integrated nonlinear optical waveguides based on GaN can exhibit correlated photon pair generation through spontaneous nonlinear optical processes, thus representing potentials for on-chip quantum sources in the visible and telecommunication spectral ranges. Despite the commercial production of GaN devices, this material still lacks a suitable substrate that would allow for a reduction of structural defects, such as high densities of threading dislocations (TDs) and grain boundaries [114–116]. These defects act as non-radiative recombination centers [117], thus deteriorating the optical quality of the epitaxially grown GaN layer. Recent studies have shown that GaN grown on (-201) $\beta - Ga_2O_3$ has a much lower lattice mismatch of 4.7% as compared to 14% for GaN grown on Sapphire (Al_2O_3) [118, 119].

This chapter details the realization of integrated optical waveguides based on GaN on (-201) $\beta - Ga_2O_3$. Using the parameters of the grown GaN wafer, the design of rib waveguides for the C-band telecommunication wavelength range centered around 1550 nm was performed with *Lumerical Mode solutions*. The design served as the guideline for the subsequent waveguide fabrication, followed by the wet-etching post-processing and experimental measurement of the propagation loss. This is the first, to the best of our knowledge, report on the realization of GaN integrated optical waveguides on Ga_2O_3 substrate. Passive optical waveguides represent key building blocks of integrated photonic circuits, and this work can act as a stepping stone in the realization of integrated optical devices based on GaN on $\beta - Ga_2O_3$ for nonlinear photonics and optoelectronics applications.

5.2 GaN growth on (-201)-oriented $\beta - Ga_2O_3$

The wafer growth was carried out by our collaborator Prof. Iman Roqan from King Abdullah Unuiversity f Science and Technology (KAUST), Saudi Arabia. GaN was epitaxially grown on (-201) $\beta - Ga_2O_3$ with the use of triethylgallium and ammonia

as source gases at 400 mbar in a Metalorganic Chemical Vapor Deposition (MOCVD) chamber. An approximately 9-nm-thick GaN buffer layer was first grown on top of a (-201) $\beta - Ga_2O_3$ (we will further use the notation Ga_2O_3 for the sake of brevity) at the temperature of 500 °C. On top of the buffer layer, the growth of a 3.5-μm-thick GaN epitaxial layer of higher optical quality has been performed at 1100 °C.

A detailed comparison of the material properties of the resulting wafer and commercially available GaN grown on Al_2O_3 (Sapphire) has been reported in [118]. The XRD rocking curve (RC) showed a superior GaN quality with a small full width at half maximum (FWHM = 330 arcsec), which is a typical FWHM value of high-quality GaN wafer [119]. XRD RC results indicated low threading dislocation density (TDD), dominated by screw and mixed type dislocations [118]. The TDD and the type of dislocations were confirmed by atomic force microscopy (AFM) and transmission electron microscopy (TEM) analysis (TDD was on the order of 108 cm^2 [118, 119]). To the best of our knowledge, this is the best RC FWHM value for GaN obtained for materials grown on a Ga_2O_3 substrate. X-ray diffraction measurements have shown a much lower value of the lattice mismatch (only 4.7%) between Ga_2O_3 and the GaN film, compared to the 14% of lattice mismatch between Al_2O_3 and GaN [118]. The photoluminescence study reported in [118] has confirmed that the GaN on Ga_2O_3 wafer has higher photoluminescence yield than GaN grown on Al_2O_3. AFM measurements have shown the root mean square (RMS) surface roughness as low as $\sim$ 0.3 nm over 400 μm^2, and $\sim$ 0.17 nm over 25 μm^2, indicating a significantly smoother surface compared to that of the commercial state-of the-art GaN grown on sapphire [118, 119]. The XRD, TEM and AFM results indicated that the (-201) $\beta - Ga_2O_3$ is the best orientation for GaN growth. We used the GaN on Ga_2O_3 wafer, characterized in [119], in our experimental studies reported hereafter.

5.3 Design of strip-loaded GaN waveguides

The first step in determining the suitability of GaN grown on Ga_2O_3 for integrated photonic applications is to attempt the realization of waveguides in such a wafer. Using *Lumerical Mode Solutions*, rib waveguides were designed with the material parameters corresponding to those of the grown GaN on Ga_2O_3 wafer and the target operation wavelength 1550 nm. The effect of chromatic dispersion was taken into account by using the reported chromatic dispersion characteristics of GaN [120] and Ga_2O_3 [121]. Figure 5.1 shows the dimensions of the designed waveguide along with the simulated intensity distribution of the fundamental TE mode for the waveguide width of 1.5 μm. We obtained from the simulations the values of the effective refractive index, $n_{\text{eff}} = 1.964$, and effective mode area, $A_{\text{eff}} = 3.80$ μm^2, for the fundamental TE mode of the waveguide shown in Figure 5.1.

5.4 Fabrication of strip-loaded GaN waveguides

The designed waveguide structures were fabricated using standard E-beam lithography followed by dry etching and post-processing. The steps of the fabrication process are outlined in Figure 5.2. The patterning process is similar to the one used for InGaAsP waveguides, as described in chapter 4, however, the thicknesses of the silica and chromium layers were increased. An increased thickness leads to a thicker final mask, which was required as GaN is known to be an etch-resistant material, resulting in low etching selectivity.

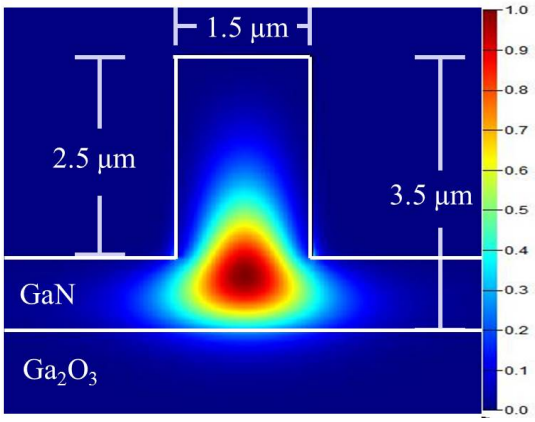

Figure 5.1: Intensity distribution of the fundamental TE mode in the designed GaN-on-Ga_2O_3 waveguide

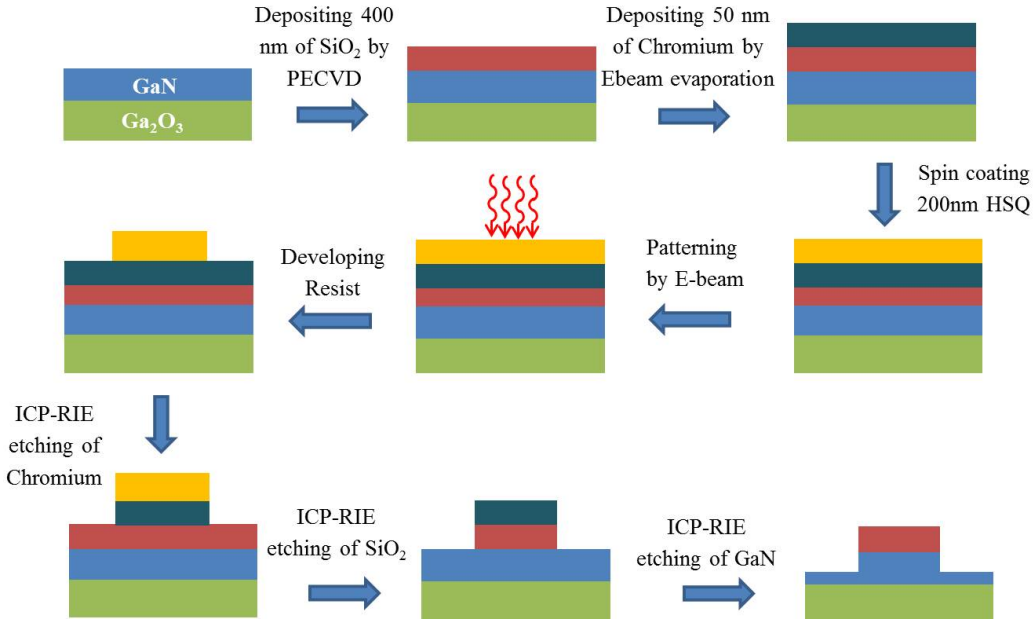

Figure 5.2: Schematic representation of the fabrication process. The PECVD deposition of a 400-nm-thick layer of SiO_2 on top of the GaN wafer was followed by an E-beam evaporation deposition of a 50-nm-thick layer of Chromium. After that, a 200-nm-thick layer of HSQ was spin-coated and patterned by E-beam lithography. The HSQ mask was then used to imprint the waveguide profile into Chromium, and the chromium was then used as a mask for etching the SiO_2 layer. GaN was finally etched through the SiO_2 mask.

5.4.1 Lithography and plasma etching

The GaN on Ga_2O_3 wafer was first diced into 1 cm x 1 cm chips. These chips were then cleaned with acetone and isopropanol, and then blow-dried with Nitrogen gas. After that, a 400-nm-thick layer of Silica (SiO_2) was deposited on top of the wafer by Plasma-Enhanced Chemical Vapor Deposition (PECVD) technique, and then 50 nm of chromium was deposited by E-beam evaporation. Following these steps, a 200-nm-thick layer of HSQ E-beam resist was spin-coated and pre-baked at 170 °C. The waveguides were then patterned using 100-kV Jeol 9500 E-beam lithography system with a dose of 950 $\mu C/cm^2$. In order to make sure that the fabricated structures

have the dimensions as per the design (the waveguide width around 1.5 μm), and to leave some room for fabrication errors, the waveguides were patterned with slightly different widths within the range of the desired value, from 1.3 to 1.7 μm, with the increment of 0.1 μm. After the E-beam patterning, the E-beam resist was developed in MIF 300 (2% tetramethylaemmonium hydroxide) for 10 min, then rinsed in de-ionized water, and cured on a hot plate at 170 °C for 1 hour. The E-beam-patterned HSQ mask was then used to transfer the waveguide pattern into chromium by ICP-RIE. A Trion etcher was used for etching the chromium layer with an optimized recipe with the following parameters: 20 sccm of chlorine and 10 sccm of argon at the pressure of 50 mT, with the ICP and RIE powers of 200 and 80 W, respectively. The chromium mask was then used to transfer the waveguide pattern into silica with an Oxford 100 ICP-RIE system using 20 sccm of difluoromethane (CH_2F_2) and 80 sccm of helium at the pressure of 4 mT, 3000-W ICP and 60-W RIE powers. The silica mask was finally used to transfer pattern into GaN.

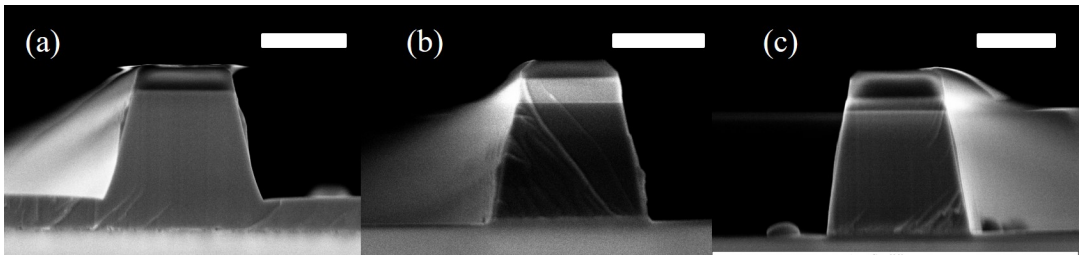

Figure 5.3: SEM images of three GaN ICP-RIE experimental trials. Each scale bar represents 1 μm. The etching recipes and parameters for each of the trials are summarized in Table 5.1.

The GaN was etched with Plasmatherm PT770 ICP-RIE system at CNF (Cornell). In order to optimize the etching recipe, a systematic parameter sweep, as described in detail earlier in chapter 2, has been performed. The swip involves varying one etching parameter at a time, while keeping the rest of the parameters unchanged, which resulted in the optimization of the parameter values. Figure 5.3 shows scanning electron microscope (SEM) images of the outcomes of three etching trials with different parameters, as outlined in Table 5.1. A Zeiss Ultra 55 SEM was used with an

Table 5.1: Etching parameters and properties of the etched-profile, namely, the etching rate, selectivity compared to silica, and side wall angle, presented for the three trial etching recipes with the resulting SEM images shown in Figure 5.3.

Trial	Etching parameters	Etching rate of GaN (nm/min)	Selectivity to silica	Side wall angle (deg)
(a)	Ar:BCl_3:Cl_2 = 5:8:20 sccm, P= 5 mT, RIE = 25 W, ICP = 400 W	150	5:1	75
(b)	Ar:BCl_3:Cl_2 = 5:8:20 sccm, P= 5 mT, RIE = 80 W, ICP = 400 W	275	4:1	79
(c)	Ar:BCl_3:Cl_2 = 5:8:20 sccm, P= 5 mT, RIE = 80 W, ICP = 250 W	250	8:1	79

accelaration voltage of 3 keV for cross-section imaging of the cleaved GaN waveguides. The etching rate of GaN, the selectivity (defined as the ratio of the etching rates of GaN and silica), and side wall verticality (defined as the sidewall angle with

respect to the normal to the substrate's surface) were measured using SEM imaging of the resulting waveguide cross-sections.

As the RIE power was increased from 25 W [trial (a) in table 5.1 to 80 W [trial (b) in table 5.1], the sidewall verticality has been improved from 75 to 79°, and the etching rate increased from 150 to 275 nm/min. On the other hand, the selectivity reduced from 5:1 to 4:1 due to the increased influence of the physical (non-selective) etching mechanism because of the higher DC bias between the generated plasma and GaN surface [**17**]. As the next step in adjusting the etching recipe, ICP power was reduced from 400 W [trial (b)] to 250 W [trial (c)], which resulted in a slight reduction of the etching rate, but improved the selectivity from 4:1 to 8:1 due to the reduced plasma density [47]. The final optimized etching recipe has the following parameters:

$$BCl_3{:}Cl_2{:}Ar = (8{:}20{:}5)\ \text{sccm, ICP} = 250\ \text{W, RIE} = 80\ \text{W, P} = 5\ \text{mT}$$

These parameters yielded the GaN etching rate of 250 nm/min, selectivity 8:1 compared to PECVD Silica, and the sidewall verticality of 79°.

The SEM images reveal some bump-like structures on the front surface of the waveguides [see Figure 5.3 (a) and Figure 5.3 (b)]. These are an artifact of SEM, arising, most probably, from charging. Another possible reason of some of these features is imperfections associated with cleaving the GaN sample, when preparing for SEM imaging.

It has been reported in multiple studies that plasma etching induces roughness on the etched surface due to the physical bombardment of the surface caused by the accelerated ions [46, 48]. Wet-chemical etching does not involve any ion bombardment, and hence there is no plasma-induced surface roughness expected from this process. A wet-chemical post-processing step involving chemical etching of plasma-damaged top surface of GaN waveguide can reduce the ICP-caused roughness, and hence the light scattering as it propagates through the waveguide. The optical propagation losses are thus expected to be lower in the post-processed samples. These arguments served as the motivation for the wet-chemical post-processing of our GaN waveguides.

5.4.2 Wet-chemical post-processing and surface roughness measurements

In this study two well-known wet etchants suitable for GaN, potassium hydroxide (KOH) [122] and tetramethylammonium hydroxide (TMAH) [123], were used. TMAH has shown more reduction in the waveguide sidewall roughness as compared to that observed with KOH. ICP-RIE-etched GaN waveguide samples were wet-etched in 25% solution of TMAH at 80 °C for 5 min, and then were rinsed in de-ionized water. Anisotropic etching property of the TMAH solution improves surface morphology by preferentially etching the side slopes until the slopes are removed entirely, resulting in a smooth and vertical surface [123]. For our GaN samples, Ga-polar (0001) plane was nearly unaffected by the etchant, whereas N-face plane was etched rapidly, which resulted in nearly vertical etched-facet. After the wet etching, the remaining silica mask was stripped by treating the sample with 10% hydroflouric acid (HF) for 3 min and rinsing it with de-ionized water. Figure 5.4 summarizes the overall fabrication process showing SEM cross-sectional images of (a) etched silica mask, (b) GaN waveguide after plasma etching, (c) GaN waveguide after post-processing using TMAH, and (d) the final GaN waveguide after stripping silica mask.

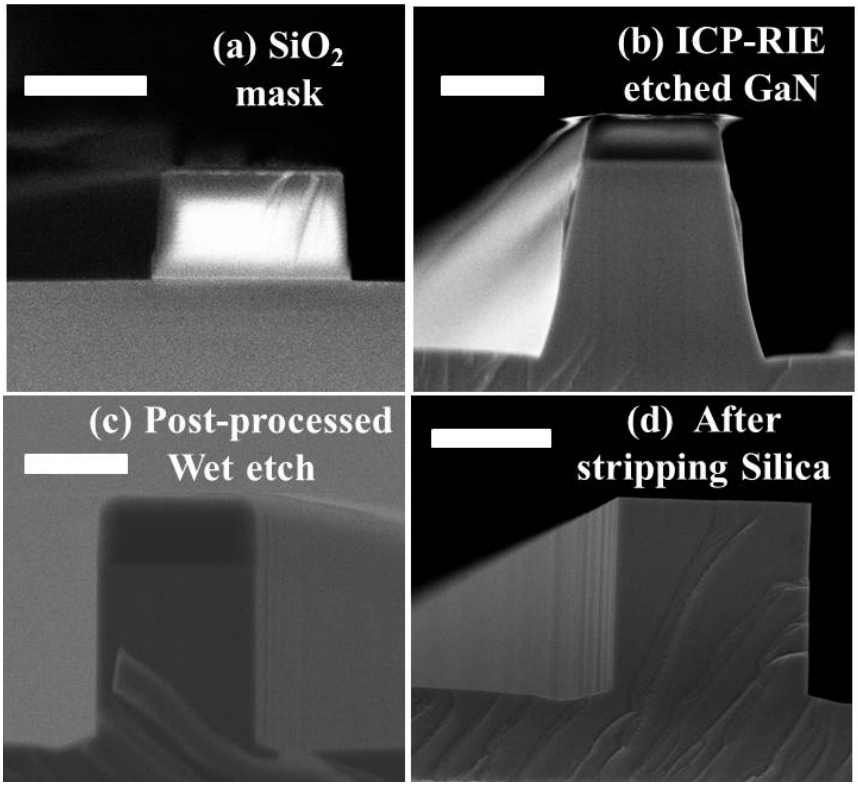

Figure 5.4: Cross-sectional SEM images of (a) silica mask after E-beam lithography and plasma etching of chromium and silica, (b) GaN waveguide etched using the optimized etching recipe, (c) GaN waveguide after TMAH post-processing (the side wall of the etched waveguide became nearly vertical), and (d) the waveguide after stripping the silica mask with hydrofluoric acid. Each scale bar represents 1 μm.

In order to confirm the reduction in the sidewall roughness of the post-processed etched waveguide surface, atomic force microscopy (AFM) analysis of the GaN waverguide sidewall before and after the post-processing was performed, using a Park NX10 AFM to quantify the impact of the wet-etching process on the surface roughness of the GaN waveguides. Figure 5.5 shows the 3D AFM plots of the etched GaN sample before [Figure 5.5 (a)] and after [Figure 5.5 (b)] the post-processing. To simplify the comparison, we used the same Y-axis scale for both the plots. It is obvious from the figure that there is a dramatic reduction in GaN surface roughness as the consequence of the chemical post-processing. The AFM data demonstrate the reduction of the root-mean-square roughness more than 4 times after the post-processing: the characteristic size of the sidewall imperfections had reduced from 1.13 to 0.23 nm.

5.5 Optical characterization

The fabricated GaN sample was cleaved on both ends and lap-polished for butt-coupling the light into and out of the waveguides. The Fabry-Perot loss measurement technique—as described in detail in section 2.5 along with the measurement setup shown in Figure 2.32 [70]—was used to quantify propagation loss . We measured the propagation loss of around 7.5 dB/cm for the fundamental TE mode in

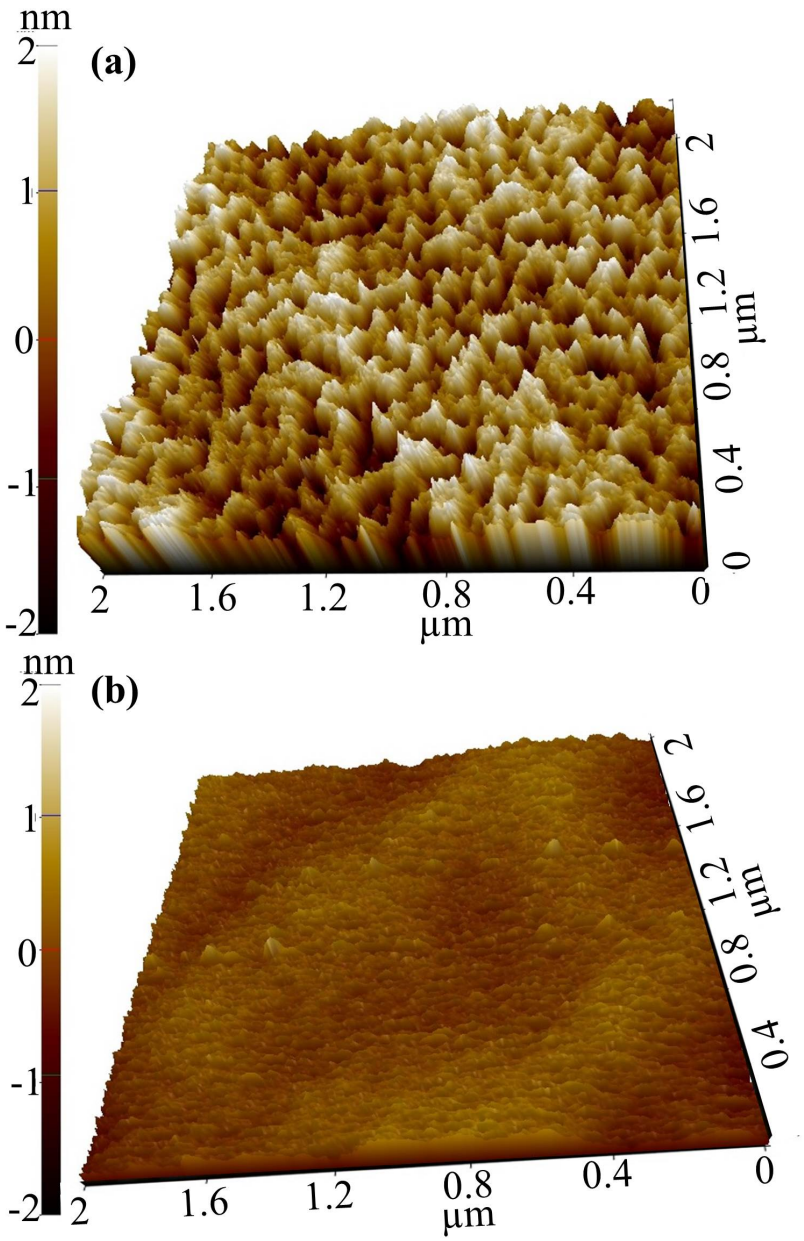

Figure 5.5: 3D AFM plots of a 2 ¯m × 2 ¯m region of GaN surface: (a) before the post-processing, (b) after the post-processing.

a 1.5-μm-wide GaN waveguide on Ga_2O_3. We were unable to observe any light guidance in the waveguides not treated with the chemical post-processing due to their higher propagation loss. This further confirms that the post-processing has improved the quality of the structures.

Experimental studies on GaN slab waveguides have shown a relatively low propagation loss ranging from 0.6 dB/cm to 3 dB/cm [124, 125]. However, a limited number of experimental studies, performed with GaN channel waveguides, have shown the measured values of the propagation loss at 1550 nm ranging from 18 dB/cm to 34.4 dB/cm [21, 126, 127] for a variety of substrate materials, such as sapphire, silicon, and aluminum nitride. There is a single study reporting the propagation loss as low as 1 dB/cm for a GaN ridge waveguide on sapphire [128]. However, the

reported waveguide structure was largely multimode with the waveguide width of 10 μm, as opposed to the 1.5 μm used in the present study. Our measured propagation loss value of 7.5 dB/cm compares well to these published studies, which confirms that Ga_2O_3 substrate holds promise for the growth of GaN with improved optical quality.

Futile attempts were made to observe SPM in these waveguides. We attribute this to high propagation loss and large A_{eff}, resulting in a reduction of the efficiency of the Kerr nonlinearrity, making it indistinguishable in spectrum analysis.

5.6 Conclusion and future work

In this work, we report on the design and fabrication of GaN waveguides on Ga_2O_3 substrate, presenting the growth of the wafer, the design and the fabrication of the GaN strip-loaded waveguides, and their subsequent wet-chemical post-processing resulting in the reduction of the surface roughness. The fabricated post-processed waveguide displayed the propagation loss of 7.5 dB/cm which compares well with other available studies. To the best of our knowledge, there are no reports on the realization of GaN waveguides on Ga_2O_3 substrate. Our experimental effort has confirmed that this substrate material holds a lot of promise for integrated photonic devices based on GaN. The future improvements to the fabrication process can lower the defect density and propagation loss, thus making it possible to exploit valuable properties of GaN in a variety of integrated photonics applications.

We intend to carry this work further by the growth and fabrication of optimized nanowire designs for GaN waveguides on Ga_2O_3 substrate. These compact waveguides can be utilized for integrated nonlinear optics over a broad spectral range, enabling applications ranging from quantum computing to all-optical signal processing.

Chapter 6

Miscellaneous projects

This chapter contains a brief description of projects associated with materials other than III-V semiconductors, that were undertaken during the course of this doctoral thesis work. The first of these, is the work on slow light tuning and applications of silicon photonic crystal waveguides (SPCW) [48, 129]. This work was performed together with Dr. Sebastian Schulz and Dr. Jeremy Upham. The second stream of projects is nanofabrication of plasmonic structures and metasurfaces. Plasmonic nanoantennas and metasurfaces were designed to experimentally observe a variety of optical effects. Only the fabrication aspect of these plasmonic devices will be discussed here.

6.1 Slow-light in silicon photonic crystal waveguides

Two-dimensional photonic crystals (PC) take advantage of their photonic band-gap and the engineering of defect modes within it to form low-loss nanophotonic components [72, 74, 80–83, 130–133]. These components include optical resonators with large quality factors and sub-wavelength cubed modal volumes [82, 134], high-confinement slow-light waveguides [84], and precise control over dispersion [85, 135, 136]. Significant efforts [137–139] have gone into the development of fabrication processes that faithfully reproduce the PC designs. Particular attention has been paid to refinements of the E-beam lithography processes [140] and plasma etching [138] steps, to limit both the offsets and random variations of the hole size, shape, and position, as well as sidewall roughness. Despite such efforts, certain deviations from the design are inevitable in fabricated samples, such as variation in substrate thickness and run-to-run differences during the fabrication, leading to systematic hole radii deviations, that result in a shift of the operating wavelength [141]. These variations necessitate a broad range of lithography doses, hole sizes, and lattice constants to be written on each sample to ensure that even a single device can be optically characterized at the intended wavelengths. Obtaining a device at the correct operation wavelength is particularly important for slow-light PC waveguides because dispersion engineering to increase the slow-down factor of a waveguide will consequently decrease the bandwidth over which slow-light can be observed [135].

This work investigates the use of inexpensive wet etching steps as a post-processing technique to tune the operating wavelength of slow-light PC waveguides in a silicon substrate. Similar post-processing approaches have been applied to devices made of III–V semiconductors [142], as well as in silicon PC nanocavities [143]. Our work demonstrates that this approach can predictably blue-shift the inherently narrow bandwidth of silicon slow-light PC waveguides to a desired operating wavelength. Tuning to the desired operating wavelength through optical characterization and post-processing significantly reduces the necessary size of parameter sweeps and

shortening expensive write times. It could also help accelerating the device development, such as delay lines or four-wave mixing waveguides for optical signal processing. Most importantly, post-processing can increase the yield of devices with slow-light waveguides per process run.

6.1.1 Fabrication of devices

To experimentally test this approach, we fabricated slow-light PC waveguides in Si, based on a W1 dispersion engineered waveguide with a lattice constant $a = 416$ nm, a typical air hole radius of 123.6 nm ($0.297a$), and shifting of the nearest and next-nearest hole rows to the line defect waveguide along the direction of the line defect by -40 nm ($-0.096a$) and 8 nm ($0.019a$), respectively. The PC waveguides were fabricated on a SOITEC silicon-on-insulator wafer comprising a 210-nm thick Si layer on 2 μm of silica. The pattern was exposed on Zep520A electron beam resist using a 30-keV RAITH E-Beam lithography system and subsequently was transferred into the silicon layer using electron cyclotron resonance (ECR) etching with a fluorine-based chemistry. Freestanding PC waveguides were created by removing the buried silica beneath the photonic crystal using HF. Figure 6.1 summarizes the fabrication steps. Subsequently, post-processing was carried out as detailed below.

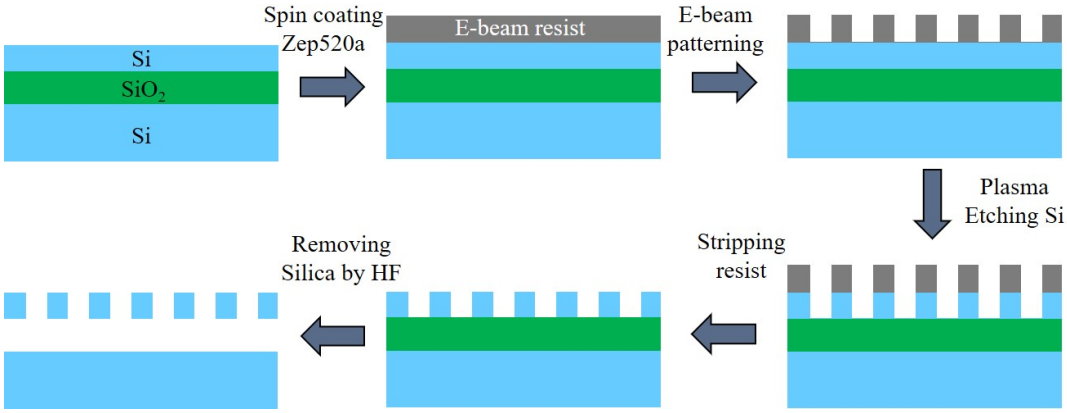

Figure 6.1: Schematic of the process flow used for the fabrication of silicon photonic crystal waveguides. The E-beam resist Zep520a spin-coated and subsequently patterned by E-beam lithography. Silicon was then etched using ECR system. The remaining E-beam resist was stripped and, finally, the undercut was performed, where silica was removed using HF.

6.1.2 Post-process wavelength tuning of silicon photonic crystal slow-light waveguides

The post-processing method used for controlled removal of Si layers from the surfaces of the PC device provides a consistent reduction of the slab thickness and enlargement of air holes. Both these modifications contribute to a blue shift of the slow-light region. The process is based on previous work by Song, *et al.* [143] on PC nanocavities. As the first step, the outer layer of Si is oxidized, resulting in the formation of thin SiO_2 layer that is subsequently removed by a selective wet etching. Oxidation is performed by an immersion of the PC sample in a solution of 1 part 30% hydrogen peroxide (H_2O_2) and 8 parts water (20 °C) for 60 s. After that, the sample is rinsed in deionized water (20 °C) for 60 s and dried with nitrogen. To selectively

etch the oxidized surface of the device, *i.e.*, the SiO_2, the device is placed in dilute hydrofluoric acid (1% HF, 20 °C) for 180 s, then rinsed in deionized water and dried with nitrogen as before. Figure 6.2 shows a schematic of a single post-processing H_2O_2-HF cycle. A repetition of the whole cycle removes additional Si layers and results in further blue shift of the slow-light region.

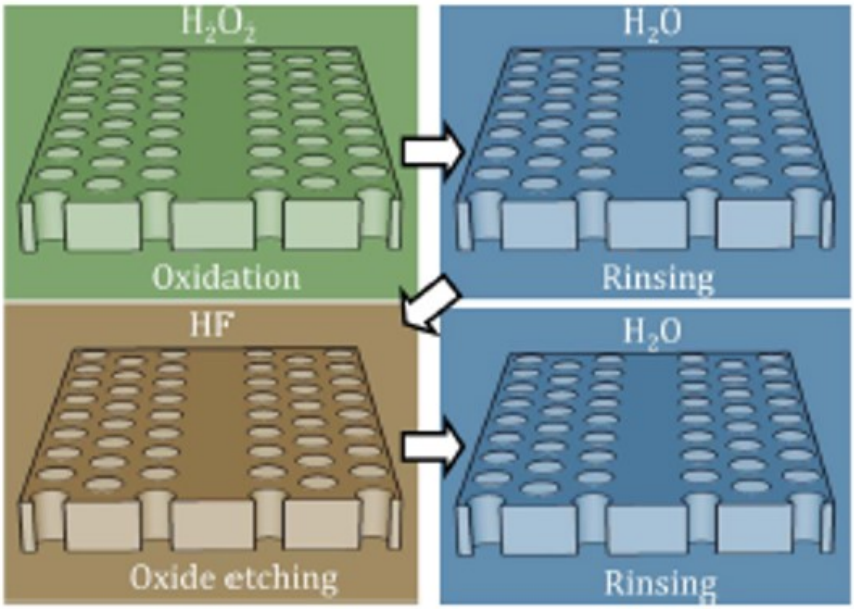

Figure 6.2: Schematic of the post-processing steps on a PC waveguide. Oxidation is performed using H_2O_2, followed by a water rinse. To etch the oxidized layer, a diluted HF was used. This step was followed by a second water rinse.

6.1.3 Measurements

We characterize this change in hole radii by inspecting approximately 250 holes with a scanning electron microscope (SEM) before and after 7 post-processing cycles. Figure 6.3 shows exemplary SEM images of the PC air holes before the post-processing and after 7 cycles of the process, along with the statistical hole-radii analysis. This analysis confirms the removal of silicon due to our H_2O_2-HF process as the average hole-radius increases from 102 to 110 nm after 7 H_2O_2-HF cycles. This increase is significantly larger than the variation of radii for each set of SEM images (the standard deviation of radii is 3.00 nm and 1.56 nm for 0 and 7 cycles, respectively). The reduction in the standard deviation after 7 cycles suggest an improvement in the uniformity of the air holes.

Group index measurements for these devices were performed via Fourier transform spectral interferometry (FTSI). A schematic of the characterisation setup is shown in Figure 6.4 (a), which consists of a Mach–Zehnder interferometer with the slow-light PC in one arm. The transmitted light is resolved using an optical spectrum analyzer (OSA) [144]. Figure 6.4 (b) shows group index measurements for the same PC waveguide device after 0, 2, 5, and 7 H_2O_2-HF cycles. Each cycle blueshifts the operating wavelength by 1.6 $\pm$ 0.1 nm, except for the first cycle, which results in a more pronounced shift. The first cycle also removes residues from the resists, any native oxide that has grown during the wafer storage, and other impurities, hence, leading to a larger shift of 4.9 $\pm$ 0.2 nm. The group index spectrum

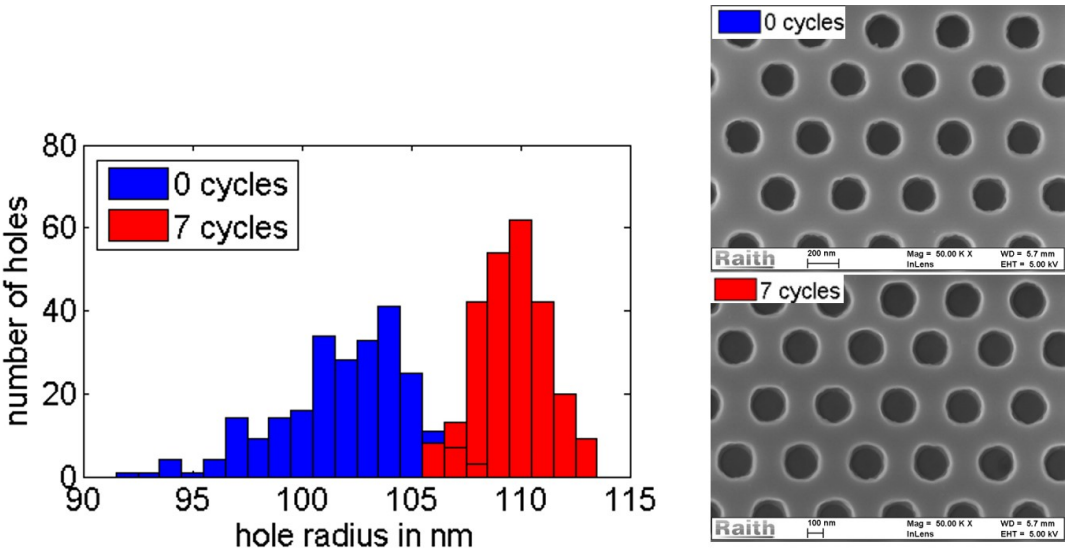

Figure 6.3: (a) Scanning electron microscope (SEM) images of PC holes before and after 7 post-processing cycles. Both images were taken at the magnification of 5,000. (b) A comparison of the hole radii from such images suggests an increased hole radius after the wet chemical etching, which is supported by a statistical analysis across multiple such images.

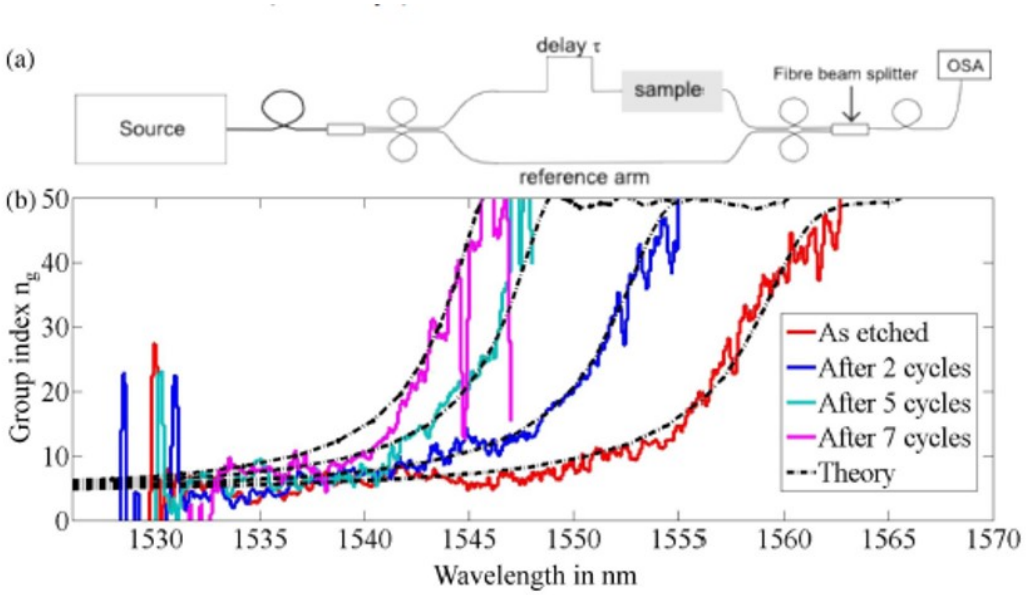

Figure 6.4: Experimental confirmation of the operation wavelength shift. (a) Schematic of the characterization set-up. (b) A comparison of theoretical (dashed lines) and experimental (solid lines) group index curves for a slow-light photonic crystal waveguide after 0, 2, 5, and 7 H_2O_2-HF cycles. The slab thickness and hole-radius were varied correspondingly, starting from the as-fabricated design, to obtain the theoretical curves for 2, 5, and 7 cycles, while all other parameters were held constant. This confirms that this process can be used to tune the operating wavelength as per the requirements by varying the number of cycles.

after 7 cycles shows some increase in the noise level as the grating couplers used to couple light from the optical fiber into the waveguides showed a reduction in the transmission power since they were blue-shifted by the post-processing. Such a reduction in transmission could be resolved by selecting the starting grating coupler design to target the intended operating wavelength, as they have a bandwidth of at least 35 nm [145]. It is also evident from Figure 6.4 (b) that post-processing cycles increase the slope of the dispersion curve. To understand this further, modeling of the characterized PC waveguides was carried out using the MIT plane wave band solver *MPB* [146].

The photonic band-gap simulations for each case were performed in 3 dimensions using MPB. For the initial, "as etched" case, the hole radius was set to 123.6 nm and the slab thickness to 210 nm, consistent with the design of the fabricated device. The dashed line overlapping the "as etched" experimental curve in Figure 6.4 (b) shows that the theoretical and experimental data match, without any free parameters. To model the device response after 2 cycles of the post-processing, the hole radius was increased by 1.5 nm, and the slab thickness was reduced by 3 nm. For all subsequent cases, the hole radius was increased by 0.25 nm, and the slab thickness was reduced by 0.5 nm per cycle. Again, no free fitting parameters were required to match the simulated group index curves to the measured results shown in Figure 6.4 (b). The simulations accurately reproduce both the shift in the operating wavelength and changes in the shape of the group index curves, suggesting that, except for the first cycle, each H_2O_2-HF cycle removed on average 0.25 nm from all exposed surfaces of the silicon PC. Given that the lattice constant of crystalline silicon is 0.54 nm and the nearest neighbor separation between silicon atoms is 0.23 nm [147], this suggests that, on average, a monolayer of silicon is being removed per cycle.

We demonstrate that a simple wet chemical process consisting of controlled oxidation and subsequent oxide removal can be used to stepwise tune the operating wavelength of slow-light PC waveguides after device fabrication and initial optical characterization. Repeat cycles of this post-processing procedure can be used to achieve precise control of the final operating wavelength of PC waveguides since each cycle blue shifts the operating wavelength by 1.6 ± 0.1 nm, excluding the first cycle. Such a blue shift is consistent with the removal of silicon during the chemical etching, and our theoretical modeling confirms this behavior. The excellent agreement between the theoretical and experimental data indicates that it is possible to predetermine the number of processing cycles required to shift a device to the desired wavelength. In principle, cycles could be repeated until the suspended structure collapses. Of course, as with dose sweeps, shifting of the operational bandwidth by this post-processing will slightly change the performance of the device. However, because the silicon removal process is uniform across all surfaces, this change is utterly predictable and can be incorporated into the design so that the device operation is not compromised while shifting the operational bandwidth. This simple method reduces the impact of variations in the slab thickness or systematic deviations of the hole-radius during fabrication, hence increasing the yield of slow-light PC waveguide fabrication. Initial evidence shows an improvement in the hole uniformity, suggesting that further investigation may be able to quantify the influence of different disorder sources (*e.g.*, surface roughness versus hole size disorder) on propagation loss in slow-light PC waveguides [148–153].

6.1.4 Enhanced spectral sensitivity of a chip-scale photonic-crystal slow-light interferometer

We collaborated with Prof. Robert Boyd's University of Rochester group members, Omar S. Magaña-Loaiza and Boshen Gao, to experimentally demonstrate that the spectral sensitivity of a Mach–Zehnder (MZ) interferometer can be enhanced through structural slow-light. We observe a 20-fold resolution enhancement by placing a dispersion-engineered, slow-light, photonic-crystal waveguide in one arm of a fiber-based MZ interferometer. The spectral sensitivity of the interferometer increases roughly linearly with the group index, and we have quantified the resolution in terms of the spectral density of interference fringes. These results show promise of the use of slow-light methods for developing novel tools for optical metrology and, specifically, for compact high-resolution spectrometers. Slow-light PC waveguides were designed, fabricated and characterized in a similar manner as outlined above. A detailed discussion and analysis can be found in our published work [129].

6.2 Fabrication of plasmonic nanostructures

The electromagnetic properties of metal/dielectric interfaces have attracted a huge amount of research interest, since the pioneering work of Mie (for small particles) and, later, Ritchie (for flat interfaces) [154, 155]. The ability of plasmonic structures to sustain coherent electron oscillations, also known as surface plasmon polaritons (SPPs), results in a high confinement of electromagnetic fields to the metallic surface. This has been intensively studied, both in light of the fundamental physics involved and for applications such as surface-enhanced spectroscopy and enhancement of nonlinear light generation [156–159]. The electric-field enhancement around metal nanostructures was found to be crucial for a variety of applications, such as, *e.g.*, spectroscopy, biosensing, data storage and solar cells [158, 160].

Recent developments in the field of nanofabrication, most notably, E-beam lithography and ion-beam milling, together with modern nanocharacterization techniques and the emergence of quantitative electromagnetic simulation tools, led to a renewed interest in the field of SPPs. This interest was further enhanced due to potential application of SPPs in sub-wavelength optical devices that can enable miniaturization of optical components, on a similar dimension scale as electronic components, *i.e*, to the sub-100 nm scale [161]. The basic physical processes that enable light localization and guidance in such structures are the aforementioned SPP excitations, and this subfield of optics is commonly referred to as plasmonics [159].

Currently, there are a number of plasmonics research projects being pursued under the supervision of Prof. Dolgaleva and Prof. Boyd. The primary interest is in the study and applications of the strong light-matter interactions that exist in plasmonic structures (single nano-particles, arrays and meta-surfaces). Some of these projects required fabrication of 20-nm-thick gold nano-particles, arrays and meta-surfaces on silica (without addition of any adhesion layer). We developed a lift-off process for the fabrication of these structures, which will be explained further; however, since the design work for these structures is beyond the scope of this thesis work, it is not included herein.

6.2.1 Bilayer lift-off process

Metal nanopatterning is commonly done using either a pattern-etching process, or a pattern-lift-off process. Pattern-etching processes are the ones used for all the structures that have been discussed thus far in this thesis work. When it comes to metals, plasma etching can induce roughness and defects. Hence, it is not suitable for defect-sensitive devices, such as plamonic nano-antennas. In the case of lift-off, the desired pattern is first written on an E-beam resist, followed by the development of the pattern. Metal thin-film is then deposited (commonly used thin-film deposition techniques for metals are thermal evaporation, E-beam evaporation and sputtering) on this E-beam mask. As a final step, the E-beam mask is removed (commonly used fabrication terminology is "stripped") using suitable wet-chemical process. This process of resist removal removes all the metal from the sample, other than what is deposited within the gaps of the E-beam mask (patterned as per the design). Two most commonly used lift-off techniques are single-layer lift-off and bi-layer lift-off. As the names suggest, the difference between these two methods is the number of resist layers that are used. For high-resolution patterns, bi-layer is known to work much more efficiently as compared to single-layer lift-off. Polymethyl methacrylate (PMMA) is a commonly used E-beam resist for the lift-off processes. It is preferred due to its superior resolution, wide range of solution concentrations (*e.g.*, 2% PMMA solution results in thinner resist layer, as compared to 4% PMMA solution), range of molecular weights and ease of stripping (typically performed using acetone). Figure 6.5(a) shows the schematic of a single-PMMA-layer lift-off process, whereas Figure 6.5(b) presents a schematic of bi-PMMA-layer lift-off process. The creation of the lip, due to the difference in the thicknesses of first and second PMMA layer, makes the bi-layer process more suitable for plasmonic nanostructures, hence, this process was chosen for the fabrication of our plasmonic samples.

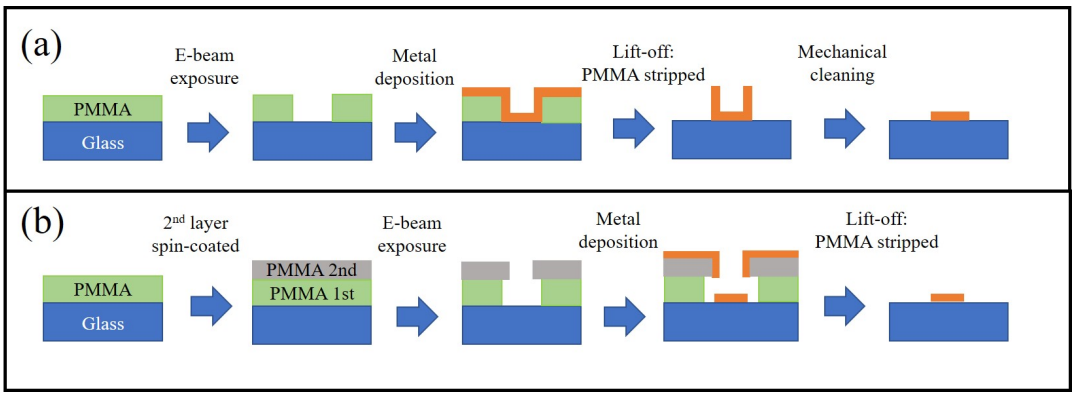

Figure 6.5: Schematics of two common types of lift-off processes: (a) a single-layer lift-off process, (b) a bi-layer lift-off process.

As the first step, 2 cm $\times$ 2 cm chips were diced from fused silica wafer, cleaned using acetone and IPA, and then were blow-dried using nitrogen. A 2% wt PMMA in anisole solution, with a molecular weight of 450,000, was used for the bottom resist layer. The diced silica samples were spin-coated at 5000 rpm for 60 seconds with an acceleration of 300 rps, and then baked at 180 °C for 30 minutes, which resulted in a 50-nm-thick bottom resist layer. Similarly, a 2% wt PMMA in anisole solution, with a molecular weight of 950,000, was used for the top resist layer. The top layer was spin-coated at 7000 rpm for 60 seconds, with an acceleration of 300 rps, which resulted in a 25-nm-thick TOP resist layer. A non-conductive substrate, such as silica,

can result in charge buildup during E-beam exposure (commonly termed as charging). To avoid charging effect during E-beam lithography of our plasmonic nanostructures, espacer, a water-soluble conductive polymer solution, was spin-coated at 2500 rpm for 25 seconds with an acceleration of 300 rps. The plasmonic nanostructures were then patterned using 30-kV Raith E-beam lithography system (CRPuO, uOttawa) with a dose of 550 $\mu C/cm^2$.

After the patterning, the samples were rinsed in de-ionized water to remove the espacer layer, and post-baked on a hot plate at 80 °C for 1 hour. The resist was then developed for 2 minutes in 3:1 MIBK-IPA (Methyl isobutyl ketone-Isopropyl Alcohol) mixture at 20 °C, followed by IPA rinse. With the PMMA bi-layer pattern prepared, metalization was then carried out. An Angstrom Nexdep evaporator was used for thermal evaporation of 20 nm gold. As a final step of the fabrication of plasmonic nanostructures, the lift-off of PMMA was performed using acetone.

6.2.2 Structural proximity error correction for E-beam lithography

Proximity error in E-beam lithography has been discussed earlier (Section 3.3.1), in the context of its effect on nearby structures; however, for the case of the plasmonic structures, due to the small scale of sub-100-nm, intra-structure proximity effect is more pronounced [136]. This intra-structure proximity effect results in a low fidelity between the designed plasmonic structures and the fabricated ones. It is also to be noted that E-beam lithography systems can resolve circular structures more accurately, as compared to structures with sharp edges, such as rectangles and triangles with sub-100-nm resolution. This is due to more accurate beam sweep technique used for circles, where the electron beam spirals inward or outward to resolve a circle. This represents the main reason why the structural proximity effect correction (PEC) used for countering intra-structure proximity effects was not required for the case of our sub-100-nm photonic crystal holes (as discussed in Chapter 3). However, the designed plasmonic nanoantennas were geometrical shapes with sharp edges (bars, split-rings, L-antennas and triangular nanoantennas), hence, the structural PEC was applied.

Fabrication test runs showed that, without applying the structural PEC, sharp edges could not be resolved. Figure 6.6 (d) shows the top-view SEM image of nanobar antenna array, fabricated using our bi-layer lift-off process and the uncorrected bar structure, as shown in Figure 6.6 (a). It was evident from this test that without structural PEC, sharp edges could not be resolved, and they came out as rounded edges. It has been shown in earlier studies that structural PEC by the addition of small "serifs" can improve the fabrication fidelity of nanobar antennas, resulting in sharper edges [136, 162, 163].

We utilized a similar approach for our various plasmonic structures. Test runs were done to determine the size of the serifs for the best fabrication fidelity for each plasmonic structure design. As an example of this structural modification, Figure 6.6 (b) shows how square serifs were added at the edge of the original structure, as shown in Figure 6.6 (a). The overlapping area between the serifs and the bar results in the polygon shown in Figure 6.6 (c). This polygon is patterned in order to obtain nanobars with sharp edges. We found that the serif squares with the side of 15 nm produce the best result for our nanobar antennas with the dimensions of 200 $\times$ 120 nm. The top-view SEM image of the fabricated and PEC-corrected nanobars is shown in Figure 6.6 (e).

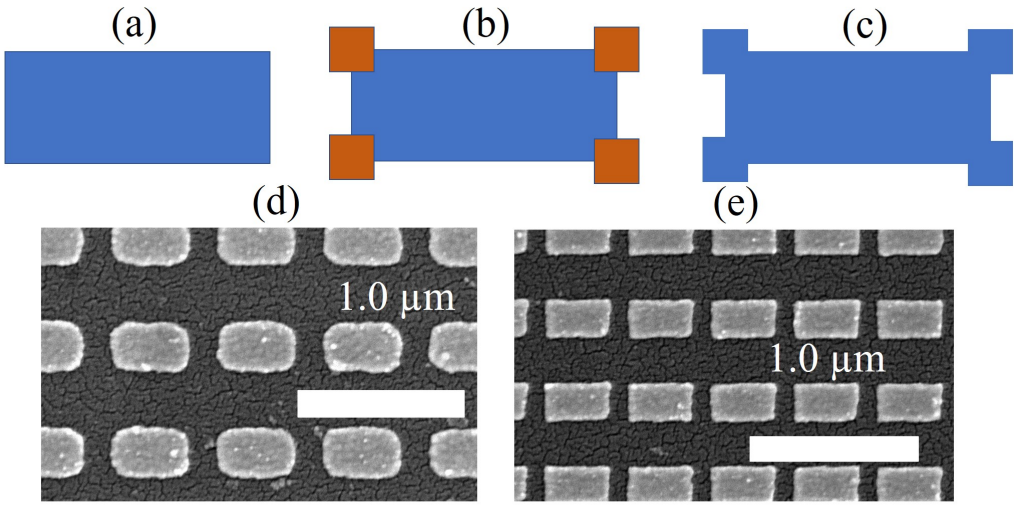

Figure 6.6: Structural PEC on nanobar antennas: (a) uncorrected bar structure, as designed in the E-beam CAD file, (b) addition of squares at the edges, centered at each edge of the nanobar, (c) PEC-corrected structure: overlap of the bar and the serif squares, (d) top-view SEM image of nanobar antenna array fabricated using the structure shown in (a), and (e) top-view SEM image of the nanobar antenna array fabricated using the PEC-corrected structure, as shown in (d).

6.2.3 Fabricated plasmonic devices and future work

Using our bi-layer lift-off process and structural PEC technique, as explained above, we fabricated a variety of plasmonic nanostructures, consisting of 20 nm gold on silica. Figure 6.7 presents the top-view SEM images of various nanoantennas that we fabricated. These include nanobars [as shown in Figure 6.7 (a), single antennas, as well as arrays of nanobars, dimensions and periodicity varied as per the designs], split-ring resonators [as shown in Figure 6.7 (b)], triangular nanoantenna arrays [as shown in Figure 6.7 (c), arrays with various sizes and periodicities were fabricated], nanodiscs [as shown in Figure 6.7 (d), no structural-PEC was required for nanodiscs, proving that the E-beam lithography system is well-suited for patterning circular structures] and gap-antennas [as shown in Figure 6.7 (e), currently, the smallest gap resolved using our fabrication process is 60 nm].

Our plasmonic fabrication process has been successfully implemented to fabricate a variety of nanoantenna structures. We are currently fabricating a few samples based on these structures for optical characterization, and also working on engineering our process for resolving gap-antennas with the target gaps as small as 20 nm.

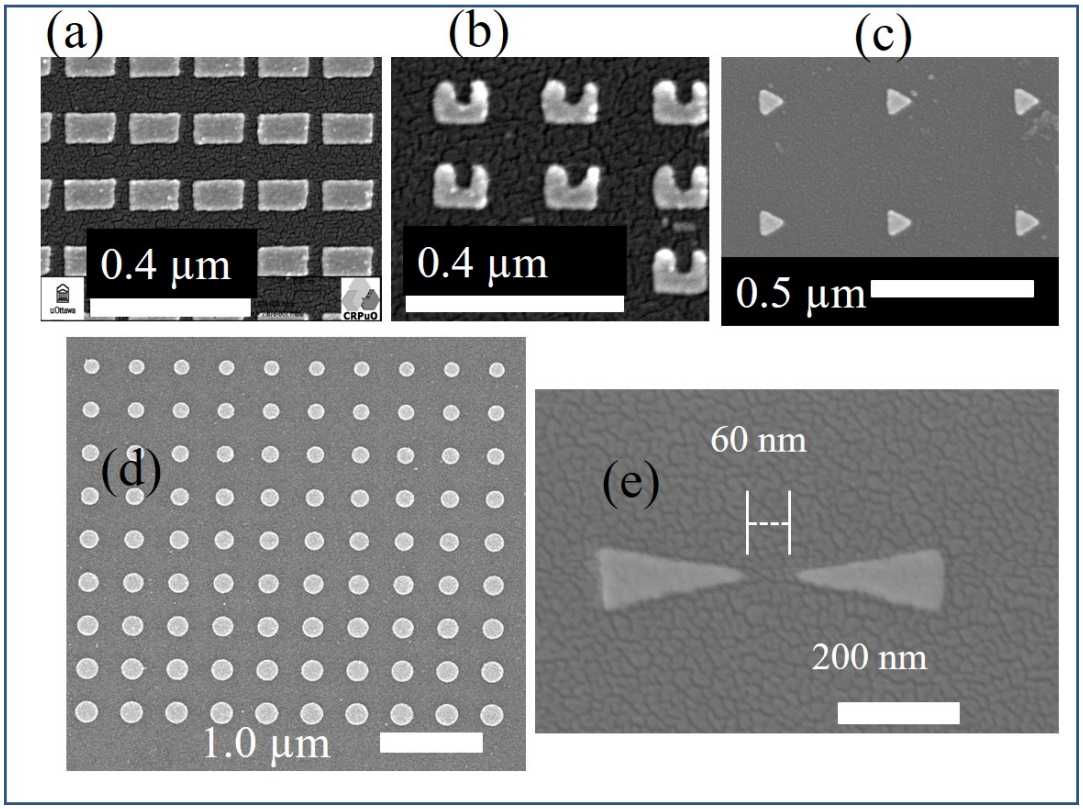

Figure 6.7: Top-view SEM images of 20 nm gold-on-silica plasmonic structures: (a) nanobar array, (b) split-ring resonator array, (c) triangular nanoantenna array, (d) nanodiscs of various diameters, (e) plasmonic gap antenna with a 60-nm gap.

Chapter 7

Conclusion

This doctoral dissertation presented fabrication processes, and their engineering methodology, for a variety of integrated photonic devices, primarily based on III-V semiconductors. We presented strip-loaded and nanowire aluminum gallium arsenide (AlGaAs) waveguide designs for enhanced optical nonlinear interaction. Based on these two designs, we proposed a novel design of half-core waveguide, with low propagation loss and high optical intensity, arising from low effective mode area. The three AlGaAs waveguide designs were then optimized, fabricated and optically characterized. The results confirm our hypothesis that the half-core waveguides are a compromise design with the propagation loss similar to that of strip-loaded waveguides, and the effective mode area much smaller compared to that of strip-loaded waveguides. Our results show that AlGaAs half-core waveguides can provide more efficient nonlinear optical interactions, compared to strip-loaded waveguides.

We then described the fabrication process for high-Q gallium arsenide photonic crystal nanocavities designed for an experimental study of polariton-blockade effect. A repeatable fabrication process comprising electron beam lithography, plasma etching and wet-chemical post-processing was engineered. The fabricated photonic crystal nanocavities are currently undergoing optical characterization for further design iterations.

Design, fabrication and optical characterization of strip-loaded indium gallium arsenide phosphide (InGaAsP) waveguides were then carried out to demonstrate the potential of quaternary III-V semiconductors for integrated nonlinear optics. We presented the first demonstration of self-phase modulation and four-wave mixing in InGaAsP waveguides. Two-photon absorption was also experimentally measured for InGaAsP. A variety of plasma etching techniques were presented for plasma etching of indium phosphide, namely, room-temperature etching, heated-substrate etching and plasma-heated etching. We are currently in the process of fabricating dispersion-engineered InGaAsP nanowire waveguides, suitable for four-wave mixing with a wide spectral tunability.

We then presented our experimental work on gallium nitride waveguides (GaN). GaN's wide band-gap makes it a very attractive material platform for integrated photonic devices. GaN has many photonics and optoelectronics applications, such as, *e.g.*, lasers and LEDs. However, GaN suffers from growth imperfections, leading to very high propagation losses. We presented the first demonstration of GaN waveguides grown on (-201) β-Gallium Oxide (Ga_2O_3), experimentally shown to have better optical quality than GaN grown on Sapphire. Patterning process, plasma etching and a wet-chemical post-processing technique were presented for the fabrication of low-loss GaN waveguides on β-Ga_2O_3. The propagation loss for these waveguides was experimentally determined to be 7.5 dB/cm, which is lower than in other reported studies on GaN channel waveguides. We intend to carry this work

further with the growth and fabrication of optimized nanowire designs for GaN waveguides on Ga_2O_3 substrate. These compact waveguides can be utilized for integrated nonlinear optics over a broad spectral range, enabling applications ranging from quantum computing to all-optical signal processing.

We also presented two project streams that are not related to the broader theme of this work, which is III-V integrated devices. The first is our work on silicon photonic crystal waveguides. We presented our published studies on a wet-chemical post-processing method for spectral tuning of slow light photonic crystal waveguides. The fabrication process and the details of the post-processing were presented, along with the optical characterization and simulation results. We have experimentally demonstrated that repeat cycles of our post-processing procedure can be used to achieve a precise control over the final operating wavelength of PC waveguides, since each cycle blue-shifts the operating wavelength by 1.6 ± 0.1 nm, excluding the first cycle. We used similar devices to experimentally demonstrate that the spectral sensitivity of a Mach–Zehnder (MZ) interferometer can be enhanced through structural slow light. We observed a 20-fold resolution enhancement by placing a dispersion-engineered, slow-light, photonic-crystal waveguide in one arm of a fiber-based MZ interferometer. The second stream of projects, unrelated to III-V semiconductors, was our work on the fabrication of plasmonic nanostructures. We presented a bi-layer lift-off process and a structural proximity effect correction technique, for the fabrication of a variety of plasmonic nanostructures. Our fabricated structures included nanobars, nanodiscs, split-ring resonators, triangular nanoantennas and gap-antennas, with sub-100-nm dimensions. All of these structures were fabricated in 20 nm gold-on-silica, without any adhesion layer. We are currently working on engineering this process to resolve gap-antennas with gaps as small as 20 nm.

In summary, this doctoral work presented repeatable and reliable micro and nanofabrication processes for III-V semiconductor integrated photonic devices.

Bibliography

[1] R. Hui, S. Taherion, Y. Wan, J. Li, S. X. Jin, J. Y. Lin, and H. X. Jiang, "Gan-based waveguide devices for long-wavelength optical communications", *Applied Physics Letters*, vol. 82, no. 9, pp. 1326–1328, 2003, ISSN: 00036951. DOI: 10.1063/1.1557790.

[2] D. Steigerwald, J. Bhat, D. Collins, R. Fletcher, M. Holcomb, M. Ludowise, P. Martin, and S. Rudaz, "Illumination with solid state lighting technology", *IEEE Journal of Selected Topics in Quantum Electronics*, vol. 8, no. 2, pp. 310–320, 2002, ISSN: 1077260X. DOI: 10.1109/2944.999186.

[3] S. Nakamura, T. Mukai, and M. Senoh, "Candela-class high-brightness InGaN/AlGaN double-heterostructure blue-light-emitting diodes", *Applied Physics Letters*, vol. 64, no. 13, pp. 1687–1689, Mar. 1994, ISSN: 00036951. DOI: 10.1063/1.111832.

[4] P. N. Prasad, *Introduction to Biophotonics*. Wiley-Interscience, 2003, p. 593, ISBN: 0471287709. DOI: 10.1002/0471465380. arXiv: arXiv:1011.1669v3.

[5] D. D. Gu, W. Meiners, K. Wissenbach, and R. Poprawe, "Laser additive manufacturing of metallic components: materials, processes and mechanisms", *International Materials Reviews*, vol. 57, no. 3, pp. 133–164, May 2012, ISSN: 0950-6608. DOI: 10.1179/1743280411Y.0000000014.

[6] G. Della Valle, R. Osellame, and P. Laporta, "Micromachining of photonic devices by femtosecond laser pulses", *Journal of Optics A: Pure and Applied Optics*, vol. 11, no. 1, p. 013 001, Jan. 2009, ISSN: 1464-4258. DOI: 10.1088/1464-4258/11/1/013001.

[7] X. Tao, *Wearable electronics and photonics*. CRC Press, 2005, pp. 1–250, ISBN: 9781855736054. DOI: 10.1533/9781845690441.198. arXiv: arXiv:1011.1669v3.

[8] D. J. Lockwood and L. Pavesi, "Silicon Fundamentals for Photonics Applications", in *Silicon Photonics, Topics in Applied Physics*, vol. 94, Springer, Berlin, Heidelberg, Feb. 2004, pp. 1–52, ISBN: 978-3-540-39913-1. DOI: 10.1007/978-3-540-39913-1_1.

[9] B. E. A. Saleh and M. C. Teich, *Fundamentals of photonics*. Wiley-Interscience, 2007, p. 1177, ISBN: 0471358320.

[10] W. Bogaerts, P. de Heyn, T. van Vaerenbergh, K. de Vos, S. Kumar Selvaraja, T. Claes, P. Dumon, P. Bienstman, D. van Thourhout, and R. Baets, "Silicon microring resonators", *Laser and Photonics Reviews*, vol. 6, no. 1, pp. 47–73, Jan. 2012, ISSN: 18638880. DOI: 10.1002/lpor.201100017. arXiv: arXiv:1208.0765v1.

[11] B. Jalali, "Silicon Photonics", *Journal of Lightwave Technology*, vol. 24, no. 12, pp. 4600–4615, Dec. 2006, ISSN: 0733-8724. DOI: 10.1002/9780470994535.

[12] N. Vico Triviño, U. Dharanipathy, J. F. Carlin, Z. Diao, R. Houdré, and N. Grandjean, "Integrated photonics on silicon with wide bandgap GaN semiconductor", *Applied Physics Letters*, vol. 102, no. 8, p. 081 120, Feb. 2013, ISSN: 00036951. DOI: 10.1063/1.4793759.

[13] G. Roelkens, L. Liu, D. Liang, R. Jones, A. Fang, B. Koch, and J. Bowers, "III-V/silicon photonics for on-chip and intra-chip optical interconnects", *Laser and Photonics Reviews*, vol. 4, no. 6, pp. 751–779, Nov. 2010, ISSN: 18638880. DOI: 10.1002/lpor.200900033.

[14] K. Gallo, G. Assanto, and G. I. Stegeman, "Efficient wavelength shifting over the erbium amplifier bandwidth via cascaded second order processes in lithium niobate waveguides", *Applied Physics Letters*, vol. 71, no. 8, p. 1020, Jun. 1997, ISSN: 00036951. DOI: 10.1063/1.119714.

[15] L. Eldada and L. W. Shacklette, "Advances in polymer integrated optics", *IEEE Journal on Selected Topics in Quantum Electronics*, vol. 6, no. 1, pp. 54–68, Jan. 2000, ISSN: 1077260X. DOI: 10.1109/2944.826873.

[16] L. Tong, R. R. Gattass, J. B. Ashcom, S. He, J. Lou, M. Shen, I. Maxwell, and E. Mazur, "Subwavelength-diameter silica wires for low-loss optical wave guiding", *Nature*, vol. 426, no. 6968, pp. 816–819, Dec. 2003, ISSN: 0028-0836. DOI: 10.1038/nature02193.

[17] F. Fiedler and A. Schlachetzki, "Optical parameters of InP-based waveguides", *Solid State Electronics*, vol. 30, no. 1, pp. 73–83, Jan. 1987, ISSN: 00381101. DOI: 10.1016/0038-1101(87)90032-3.

[18] C. Xiong, W. Pernice, K. K. Ryu, C. Schuck, K. Y. Fong, T. Palacios, and H. X. Tang, "Integrated GaN photonic circuits on silicon (100) for second harmonic generation", *Optics Express*, vol. 19, no. 11, p. 10 462, May 2011, ISSN: 1094-4087. DOI: 10.1364/OE.19.010462. arXiv: 1010.6042.

[19] R. A. Logan and F. K. Reinhart, "Optical Waveguides in GaAs-AlGaAs Epitaxial Layers", *IEEE Transactions on Electron Devices*, vol. 20, no. 12, p. 1173, Sep. 1973, ISSN: 15579646. DOI: 10.1109/T-ED.1973.17826.

[20] W. Stutius and W. Streifer, "Silicon nitride films on silicon for optical waveguides", *Applied Optics*, vol. 16, no. 12, p. 3218, Dec. 1977, ISSN: 0003-6935. DOI: 10.1364/AO.16.003218.

[21] a. Lupu, F. H. Julien, S. Golka, G. Pozzovivo, G. Strasser, E. Baumann, F. Giorgetta, D. Hofstetter, S. Nicolay, M. Mosca, E. Feltin, J. Carlin, and N. Grandjean, "Lattice-Matched GaN–InAlN Waveguides at λ=1.55 μm Grown by Metal – Organic Vapor Phase Epitaxy", *IEEE Photonics Technology Letters*, vol. 20, no. 2, pp. 102–104, Jan. 2008, ISSN: 1041-1135. DOI: 10.1109/LPT.2007.912551.

[22] M. Volatier, D. Duchesne, R. Morandotti, R. Arès, and V. Aimez, "Extremely high aspect ratio GaAs and GaAs/AlGaAs nanowaveguides fabricated using chlorine ICP etching with N_2 promoted passivation", *Nanotechnology*, vol. 21, no. 13, p. 134 014, Apr. 2010, ISSN: 0957-4484. DOI: 10.1088/0957-4484/21/13/134014.

[23] M. Galli, S. L. Portalupi, M. Belotti, L. C. Andreani, L. O'Faolain, and T. F. Krauss, "Light scattering and Fano resonances in high-Q photonic crystal nanocavities", *Applied Physics Letters*, vol. 94, no. 7, p. 071 101, Feb. 2009, ISSN: 00036951. DOI: 10.1063/1.3080683.

[24] M. Popovic, T. Barwicz, M. Dahlem, F. Gan, C. Holzwarth, P. Rakich, H. Smith, E. Ippen, and F. Kartner, "Tunable, fourth-order silicon microring-resonator add-drop filters", in *33rd European Conference and Exhibition on Optical Communication - ECOC 2007*, vol. 2007, IEE, 2007, pp. 123–123, ISBN: 978-3-8007-3042-1. DOI: 10.1049/ic:20070077.

[25] R. Rediker, T. Quist, and B. Lax, "High speed heterojunction photodiodes and beam-of-light transistors", *Proceedings of the IEEE*, vol. 51, no. 1, pp. 218–219, 1963, ISSN: 0018-9219. DOI: 10.1109/PROC.1963.1684.

[26] M. G. A. Bernard and G. Duraffourg, "Laser Conditions in Semiconductors", *Physica status solidi (b)*, vol. 1, no. 7, pp. 699–703, Jan. 1961, ISSN: 03701972. DOI: 10.1002/pssb.19610010703.

[27] Y.-M. He, Y. He, Y.-J. Wei, D. Wu, M. Atatüre, C. Schneider, S. Höfling, M. Kamp, C.-Y. Lu, and J.-W. Pan, "On-demand semiconductor single-photon source with near-unity indistinguishability", *Nature Nanotechnology*, vol. 8, no. 3, pp. 213–217, Feb. 2013, ISSN: 1748-3387. DOI: 10.1038/nnano.2012.262. arXiv: 1303.4058.

[28] R. H. Hadfield, "Single-photon detectors for optical quantum information applications", *Nature Photonics*, vol. 3, no. 12, pp. 696–705, Dec. 2009, ISSN: 1749-4885. DOI: 10.1038/nphoton.2009.230.

[29] B. H. Verbeek, C. H. Henury, N. A. Olsson, K. J. Orlowsky, R. F. Kazarinov, and B. H. Johnson, "Integrated Four-channel Mach-Zehnder Multi/Demultiplexer Fabricated with Phosphorous Doped SiO_2 Waveguides on Si", *Journal of Lightwave Technology*, vol. 6, no. 6, pp. 1011–1015, Jun. 1988, ISSN: 15582213. DOI: 10.1109/50.4092.

[30] H. Heidrich, P. Albrecht, M. Hamacher, H. P. Nolting, H. Schroeter-Janben, and C. M. Weinert, "Passive Mode Converter with a Periodically Tilted InP/GaInAsP Rib Waveguide", *IEEE Photonics Technology Letters*, vol. 4, no. 1, pp. 34–36, Jan. 1992, ISSN: 19410174. DOI: 10.1109/68.124867.

[31] T. L. Koch, U. Koren, G. Eisenstein, M. G. Young, M. Oron, C. R. Giles, and B. I. Miller, "Tapered Waveguide InGaAs/InGaAsP Multiple-Quantum-Well Lasers", *IEEE Photonics Technology Letters*, vol. 2, no. 2, pp. 88–90, Feb. 1990, ISSN: 19410174. DOI: 10.1109/68.47056.

[32] S. W. Koch, *Semiconductor-Laser Fundamentals*. Berlin, Heidelberg: Springer Berlin Heidelberg, 1999, ISBN: 3540641661. DOI: 10.1007/978-3-662-03880-2.

[33] S. Saeidi, K. M. Awan, L. Sirbu, and K. Dolgaleva, "Nonlinear photonics on-a-chip in III-V semiconductors: quest for promising material candidates", *Applied Optics*, vol. 56, no. 19, p. 5532, Jul. 2017, ISSN: 1559-128X. DOI: 10.1364/AO.56.005532.

[34] K. Dolgaleva, P. Sarrafi, P. Kultavewuti, K. M. Awan, N. Feher, J. S. Aitchison, L. Qian, M. Volatier, R. Arès, and V. Aimez, "Tuneable four-wave mixing in AlGaAs nanowires", *Optics Express*, vol. 23, no. 17, p. 22 477, Aug. 2015, ISSN: 1094-4087. DOI: 10.1364/OE.23.022477.

[35] I. L. Medintz, H. T. Uyeda, E. R. Goldman, and H. Mattoussi, "Quantum dot bioconjugates for imaging, labelling and sensing", *Nature Materials*, vol. 4, no. 6, pp. 435–446, Jun. 2005, ISSN: 1476-1122. DOI: 10.1038/nmat1390. arXiv: NIHMS150003.

[36] A. J. Nozik, "Quantum dot solar cells", *Physica E: Low-Dimensional Systems and Nanostructures*, vol. 14, no. 1-2, pp. 115–120, Apr. 2002, ISSN: 13869477. DOI: 10.1016/S1386-9477(02)00374-0.

[37] N. Holonyak, R. M. Kolbas, R. D. Dupuis, and P. D. Dapkus, "Quantum-Well Heterostructure Lasers", *IEEE Journal of Quantum Electronics*, vol. 16, no. 2, pp. 170–186, Feb. 1980, ISSN: 15581713. DOI: 10.1109/JQE.1980.1070447.

[38] R. Nagarajan, M. Kato, J. Pleumeekers, P. Evans, D. Lambert, A. Chen, V. Dominic, A. Mathur, P. Chavarkar, M. Missey, A. Dentai, S. Hurtt, J. Bäck, R. Muthiah, S. Murthy, R. Salvatore, S. Grubb, C. Joyner, J. Rossi, R. Schneider, M. Ziari, F. Kish, and D. Welch, "Single-chip 40-channel InP transmitter photonic integrated circuit capable of aggregate data rate of 1.6 Tbit/s", *Electronics Letters*, vol. 42, no. 13, p. 771, 2006, ISSN: 00135194. DOI: 10.1049/el:20060823. arXiv: 0504102 [arXiv:physics].

[39] D. Liang, G. Roelkens, R. Baets, and J. E. Bowers, "Hybrid integrated platforms for silicon photonics", *Materials*, vol. 3, no. 3, pp. 1782–1802, Mar. 2010, ISSN: 19961944. DOI: 10.3390/ma3031782.

[40] G. I. Stegeman, E. M. Wright, N. Finlayson, R. Zanoni, and C. T. Seaton, "Third Order Nonlinear Integrated Optics", *Journal of Lightwave Technology*, vol. 6, no. 6, pp. 953–970, Jun. 1988, ISSN: 15582213. DOI: 10.1109/50.4087.

[41] K. Iga, F. Koyama, and S. Kinoshita, "Surface Emitting Semiconductor Lasers", *IEEE Journal of Quantum Electronics*, vol. 24, no. 9, pp. 1845–1855, Sep. 1988, ISSN: 15581713. DOI: 10.1109/3.7126.

[42] V. Van, T. A. Ibrahim, K. Ritter, P. P. Absil, F. G. Johnson, R. Grover, J. Goldhar, and P. T. Ho, "All-optical nonlinear switching in GaAs-AlGaAs microring resonators", *IEEE Photonics Technology Letters*, vol. 14, no. 1, pp. 74–76, Jan. 2002, ISSN: 10411135. DOI: 10.1109/68.974166.

[43] A. Gaggero, S. J. Nejad, F. Marsili, F. Mattioli, R. Leoni, D. Bitauld, D. Sahin, G. J. Hamhuis, R. Nötzel, R. Sanjines, and A. Fiore, "Nanowire superconducting single-photon detectors on GaAs for integrated quantum photonic applications", *Applied Physics Letters*, vol. 97, no. 15, p. 151 108, Oct. 2010, ISSN: 00036951. DOI: 10.1063/1.3496457.

[44] L. F. Thompson, C. G. Willson, and M. J. Bowden, *Introduction to microlithography*. American Chemical Society, 1994, p. 527, ISBN: 0841228485. DOI: 10.1021/bk-1983-0219.

[45] D. C. Hays, H. Cho, K. B. Jung, Y. B. Hahn, C. R. Abernathy, S. J. Pearton, F. Ren, and W. S. Hobson, "Selective dry etching using inductively coupled plasmas. Part I. GaAs/AlGaAs and GaAs/InGaP", *Applied Surface Science*, vol. 147, no. 1, pp. 125–133, May 1999, ISSN: 01694332. DOI: 10.1016/S0169-4332(99)00103-8.

[46] R. Sanatinia, K. M. Awan, S. Naureen, N. Anttu, E. Ebraert, and S. Anand, "GaAs nanopillar arrays with suppressed broadband reflectance and high optical quality for photovoltaic applications", *Optical Materials Express*, vol. 2, no. 11, pp. 1671–1679, 2012, ISSN: 2159-3930. DOI: 10.1364/OME.2.001671. arXiv: arXiv:1106.1603.

[47] K. M. Awan, R. Sanatinia, and S. Anand, "Nanostructuring of GaAs with tailored topologies using colloidal lithography and dry etching", *Journal of Vacuum Science & Technology B, Nanotechnology and Microelectronics: Materials, Processing, Measurement, and Phenomena*, vol. 32, no. 2, p. 021 801, Mar. 2014, ISSN: 2166-2746. DOI: 10.1116/1.4862976.

[48] K. M. Awan, S. A. Schulz, D. X. Liu, K. Dolgaleva, J. Upham, and R. W. Boyd, "Post-process wavelength tuning of silicon photonic crystal slow-light waveguides.", *Optics letters*, vol. 40, no. 9, pp. 1952–5, May 2015, ISSN: 1539-4794.

[49] S. Naureen, R. Sanatinia, N. Shahid, and S. Anand, "High optical quality InP-based nanopillars fabricated by a top-down approach", *Nano Letters*, vol. 11, no. 11, pp. 4805–4811, 2011, ISSN: 15306984. DOI: 10.1021/nl202628m.

[50] E. Sauter, *Nonlinear optics*. Academic Press, 1996, p. 613, ISBN: 0121216829.

[51] K. Dolgaleva, W. C. Ng, L. Qian, and J. S. Aitchison, "Compact highly-nonlinear AlGaAs waveguides for efficient wavelength conversion", *Optics Express*, vol. 19, no. 13, p. 12 440, Jun. 2011, ISSN: 1094-4087. DOI: 10.1364/OE.19.012440.

[52] P. Kultavewuti, E. Y. Zhu, L. Qian, V. Pusino, M. Sorel, and J. Stewart Aitchison, "Correlated photon pair generation in AlGaAs nanowaveguides via spontaneous four-wave mixing", *Optics Express*, vol. 24, no. 4, p. 3365, Feb. 2016, ISSN: 1094-4087. DOI: 10.1364/OE.24.003365.

[53] H. F. Hameka, "Theory of three-photon absorption", *Physica*, vol. 32, no. 4, pp. 779–784, Apr. 1966, ISSN: 0031-8914. DOI: 10.1016/0031-8914(66)90010-3.

[54] S. W. Hell, K. Bahlmann, M. Schrader, A. Soini, H. M. Malak, I. Gryczynski, and J. R. Lakowicz, "Three-photon excitation in fluorescence microscopy.", *Journal of biomedical optics*, vol. 1, no. 1, pp. 71–4, 1996, ISSN: 1083-3668. DOI: 10.1117/12.229062.

[55] M. Albota, "Design of Organic Molecules with Large Two-Photon Absorption Cross Sections", *Science*, vol. 281, no. 5383, pp. 1653–1656, Sep. 1998, ISSN: 0036-8075. DOI: 10.1126/science.281.5383.1653.

[56] S. P. Schilders and M. Gu, "Three-dimensional autofluorescence spectroscopy of rat skeletal muscle tissue under two-photon excitation.", *Applied Optics*, vol. 38, no. 38, pp. 720–723, Feb. 1999, ISSN: 0003-6935. DOI: 10.1364/AO.38.000720.

[57] S. Adachi, *Properties of Semiconductor Alloys*. Wiley, 2009, p. 400.

[58] A. R. Denton and N. W. Ashcroft, "Vegards law", *Physical Review A*, vol. 43, no. 6, pp. 3161–3164, Mar. 1991, ISSN: 10502947. DOI: 10.1103/PhysRevA.43.3161.

[59] L. Vegard, "Die Konstitution der Mischkristalle und die Raumfllung der Atome", *Zeitschrift fr Physik*, vol. 5, no. 1, pp. 17–26, Jan. 1921, ISSN: 14346001. DOI: 10.1007/BF01349680.

[60] B. M. Cannon, T. Mahmood, W. Astar, P. Apiratikul, G. Porkolab, P. Boudra, T. Mohsenin, C. J. K. Richardson, and G. M. Carter, "All-optical amplitude-phase transmultiplexing of RZ-OOK and RZ-BPSK to RZ-QPSK by polarization-insensitive XPM using a nonlinear birefringent AlGaAs waveguide", *Optics Express*, vol. 21, no. 17, p. 19 885, Aug. 2013, ISSN: 1094-4087. DOI: 10.1364/OE.21.019885.

[61] G. Stegeman, A. Villenueuve, J. Kang, J. Aitchison, C. Ironside, K. Al-hemyari, C. Yang, C.-H. Lin, H.-H. Lin, G. Kennedy, R. Grant, and W. Sibbett, "AlGaAs BELOW HALF BANDGAP: THE SILICON OF NONLINEAR OPTICAL MATERIALS", *Journal of Nonlinear Optical Physics & Materials*, vol. 03, no. 03, pp. 347–371, Jul. 1994, ISSN: 0218-8635. DOI: 10.1142/S0218199194000213.

[62] A. W. Bett, F. Dimroth, G. Stollwerck, and O. V. Sulima, "III-V compounds for solar cell applications", *Applied Physics A: Materials Science and Processing*, vol. 69, no. 2, pp. 119–129, Aug. 1999, ISSN: 09478396. DOI: 10.1007/s003390050983.

[63] J. Meier, W. S. Mohammed, a. Jugessur, L. Qian, M. Mojahedi, and J. S. Aitchison, "Group velocity inversion in AlGaAs nanowires.", *Optics express*, vol. 15, no. 20, pp. 12 755–62, Oct. 2007, ISSN: 1094-4087. DOI: 10.1364/OE.15.012755.

[64] R. Iwanow, G. I. Stegeman, D. N. Christodoulides, R. Morandotti, D. Modotto, A. Locatelli, C. De Angelis, F. Pozzi, C. R. Stanley, M. Sorel, and J. S. Aitchison, "Enhanced third order nonlinear effects in AlGaAs nanowires", *Conference on Lasers and Electro-Optics and 2006 Quantum Electronics and Laser Science Conference, CLEO/QELS 2006*, vol. 14, no. 20, p. 9377, Oct. 2006, ISSN: 1094-4087. DOI: 10.1109/CLEO.2006.4627663.

[65] S. Gehrsitz, F. K. Reinhart, C. Gourgon, N. Herres, A. Vonlanthen, and H. Sigg, "The refractive index of AlGaAs below the band gap: Accurate determination and empirical modeling", *Journal of Applied Physics*, vol. 87, no. 11, pp. 7825–7837, Jun. 2000, ISSN: 0021-8979. DOI: 10.1063/1.373462.

[66] T. Maeda, J. W. Lee, R. J. Shul, J. Han, J. Hong, E. S. Lambers, S. J. Pearton, C. R. Abernathy, and W. S. Hobson, "Inductively coupled plasma etching of III-V semiconductors in BCl3-based chemistries. I. GaAs, GaN, GaP, GaSb and AlGaAs", *Applied Surface Science*, vol. 143, no. 1, pp. 174–182, Apr. 1999, ISSN: 01694332. DOI: 10.1016/S0169-4332(98)00594-7.

[67] B. A. Pathak, "ELECTROSTATIC (LANGMUIR) PROBE MEASUREMENTS IN RF DRIVEN He, N2, BCl3, AND BCl3/N2 PLASMAS", Aug. 2008.

[68] H. Tamura and H. Kurihara, "GaAs and GaAlAs Reactive Ion Etching in BCl3-Cl2 Mixture", *Japanese Journal of Applied Physics*, vol. 23, no. 9, pp. L731–L733, Sep. 1984, ISSN: 13474065. DOI: 10.1143/JJAP.23.L731.

[69] K. M. Awan, M. M. Muhammad, M. Sivan, S. Bonca, I. S. Roqan, and K. Dolgaleva, "Fabrication and optical characterization of GaN waveguides on (-201)-oriented beta-Ga2O3", *Opt. Mater. Express*, vol. 8, no. 1, pp. 88–96, Jan. 2018. DOI: 10.1364/OME.8.000088.

[70] R. Regener and W. Sohler, "Loss in low-finesse Ti:LiNbO3 optical waveguide resonators", *Applied Physics B Photophysics and Laser Chemistry*, vol. 36, no. 3, pp. 143–147, Mar. 1985, ISSN: 07217269. DOI: 10.1007/BF00691779.

[71] M. Pu, L. Ottaviano, E. Semenova, and K. Yvind, "Efficient frequency comb generation in AlGaAs-on-insulator", *Optica*, vol. 3, no. 8, p. 823, Sep. 2016, ISSN: 2334-2536. DOI: 10.1364/OPTICA.3.000823. arXiv: 1509.03620.

[72] E. Yablonovitch, "Inhibited spontaneous emission in solid-state physics and electronics", *Physical Review Letters*, vol. 58, no. 20, pp. 2059–2062, May 1987, ISSN: 00319007. DOI: 10.1103/PhysRevLett.58.2059.

[73] R. De La Rue and C. Seassal, "Photonic crystal devices: some basics and selected topics", *Laser & Photonics Reviews*, vol. 6, no. 4, pp. 564–597, Jul. 2012, ISSN: 1863-8899. DOI: 10.1002/lpor.201100044.

[74] S. John, "Strong localization of photons in certain disordered dielectric superlattices", *Physical Review Letters*, vol. 58, no. 23, pp. 2486–2489, Jun. 1987, ISSN: 00319007. DOI: 10.1103/PhysRevLett.58.2486.

[75] C. Weisbuch, H. Benisty, M. Rattie, C. J. Smith, and T. F. Krauss, "Advances in 2D semiconductor photonic crystals", *Synthetic Metals*, vol. 116, no. 1-3, pp. 449–452, Jan. 2001, ISSN: 03796779. DOI: 10.1016/S0379-6779(00)00412-4.

[76] J. D. (D. Joannopoulos, S. G. Johnson, J. N. Winn, and R. D. Meade, *Photonic crystals : molding the flow of light*. Princeton University Press, 2008, p. 286, ISBN: 9780691124568.

[77] Y. Xia, B. Gates, and S. H. Park, "Fabrication of three-dimensional photonic crystals for use in the spectral region from ultraviolet to near-infrared", *Journal of Lightwave Technology*, vol. 17, no. 11, pp. 1956–1962, 1999, ISSN: 07338724. DOI: 10.1109/50.802980.

[78] S. Ogawa, M. Imada, S. Yoshimoto, M. Okano, and S. Noda, "Control of light emission by 3D photonic crystals", *Science*, vol. 305, no. 5681, pp. 227–229, Jul. 2004, ISSN: 00368075. DOI: 10.1126/science.1097968.

[79] J. E. Baker, R. Sriram, and B. L. Miller, "Two-dimensional photonic crystals for sensitive microscale chemical and biochemical sensing", *Lab Chip*, vol. 15, no. 4, pp. 971–990, Feb. 2015, ISSN: 1473-0197. DOI: 10.1039/C4LC01208A.

[80] T. F. Krauss, R. M. De La Rue, and S. Brand, "Two-dimensional photonic-bandgap structures operating at near-infrared wavelengths", *Nature*, vol. 383, no. 6602, pp. 699–702, Oct. 1996, ISSN: 00280836. DOI: 10.1038/383699a0.

[81] S. Noda, A. Chutinan, and M. Imada, "Trapping and emission of photons by a single defect in a photonic bandgap structure", *Nature*, vol. 407, no. 6804, pp. 608–610, Oct. 2000, ISSN: 00280836. DOI: 10.1038/35036532.

[82] Y. Akahane, T. Asano, B. S. Song, and S. Noda, "High-Q photonic nanocavity in a two-dimensional photonic crystal", *Nature*, vol. 425, no. 6961, pp. 944–947, Oct. 2003, ISSN: 00280836. DOI: 10.1038/nature02063.

[83] B. S. Song, S. Noda, T. Asano, and Y. Akahane, "Ultra-high-Q photonic double-heterostructure nanocavity", *Nature Materials*, vol. 4, no. 3, pp. 207–210, Mar. 2005, ISSN: 14761122. DOI: 10.1038/nmat1320.

[84] M. Notomi, K. Yamada, A. Shinya, J. Takahashi, C. Takahashi, and I. Yokohama, "Extremely large group-velocity dispersion of line-defect waveguides in photonic crystal slabs", *Physical Review Letters*, vol. 87, no. 25, pp. 253902–253902–4, Nov. 2001, ISSN: 10797114. DOI: 10.1103/PhysRevLett.87.253902.

[85] L. H. Frandsen, A. V. Lavrinenko, J. Fage-Pedersen, and P. I. Borel, "Photonic crystal waveguides with semi-slow light and tailored dispersion properties", *Optics Express*, vol. 14, no. 20, p. 9444, Oct. 2006, ISSN: 1094-4087. DOI: 10.1364/OE.14.009444.

[86] L. O'Faolain, S. A. Schulz, D. M. Beggs, T. P. White, M. Spasenović, L. Kuipers, F. Morichetti, A. Melloni, S. Mazoyer, J. P. Hugonin, P. Lalanne, and T. F. Krauss, "Loss engineered slow light waveguides", *Optics Express*, vol. 18, no. 26, pp. 27 627–27 638, Dec. 2010, ISSN: 1094-4087. DOI: 10.1364/OE.18.027627.

[87] J. Kasprzak, M. Richard, S. Kundermann, A. Baas, P. Jeambrun, J. M. Keeling, F. M. Marchetti, M. H. Szymánska, R. André, J. L. Staehli, V. Savona, P. B. Littlewood, B. Deveaud, and L. S. Dang, "Bose-Einstein condensation of exciton polaritons", *Nature*, vol. 443, no. 7110, pp. 409–414, Sep. 2006, ISSN: 14764687. DOI: 10.1038/nature05131.

[88] A. Verger, C. Ciuti, and I. Carusotto, "Polariton quantum blockade in a photonic dot", *Physical Review B - Condensed Matter and Materials Physics*, vol. 73, no. 19, p. 193 306, May 2006, ISSN: 10980121. DOI: 10.1103/PhysRevB.73.193306. arXiv: 0511336 [cond-mat].

[89] M. Minkov and V. Savona, "Automated optimization of photonic crystal slab cavities.", *Scientific reports*, vol. 4, no. 1, p. 5124, May 2014, ISSN: 2045-2322. DOI: 10.1038/srep05124.

[90] K. Koshelev, M. Ali Mohammad, T. Fito, K. L. Westra, S. K. Dew, and M. Stepanova, "Comparison between ZEP and PMMA resists for nanoscale electron beam lithography experimentally and by numerical modeling", *Journal of Vacuum Science & Technology B, Nanotechnology and Microelectronics: Materials, Processing, Measurement, and Phenomena*, vol. 29, no. 6, 06F306, Nov. 2011, ISSN: 2166-2746. DOI: 10.1116/1.3640794.

[91] T. H. P. Chang, "Proximity effect in electron-beam lithography", *Journal of Vacuum Science and Technology*, vol. 12, no. 6, pp. 1271–1275, Nov. 1975, ISSN: 0022-5355. DOI: 10.1116/1.568515.

[92] P. Li, "A Review of Proximity Effect Correction in Electron-beam Lithography", Sep. 2015. arXiv: 1509.05169.

[93] T. A. Fretwell, R. Gurung, and P. L. Jones, "Curve fitting to Monte Carlo data for the determination of proximity effect correction parameters", *Microelectronic Engineering*, vol. 17, no. 1-4, pp. 389–394, Mar. 1992, ISSN: 01679317. DOI: 10.1016/0167-9317(92)90079-7.

[94] J. Zhou and X. Yang, "Monte Carlo simulation of process parameters in electron beam lithography for thick resist patterning", *Journal of Vacuum Science & Technology B: Microelectronics and Nanometer Structures*, vol. 24, no. 3, p. 1202, 2006, ISSN: 10711023. DOI: 10.1116/1.2192543.

[95] A. G. Foyt, "The electro-optic applications of InP", *Journal of Crystal Growth*, vol. 54, no. 1, pp. 1–8, Jul. 1981, ISSN: 00220248. DOI: 10.1016/0022-0248(81)90241-4.

[96] E. Kuphal, "Phase diagrams of InGaAsP, InGaAs and InP lattice-matched to (100)InP", *Journal of Crystal Growth*, vol. 67, no. 3, pp. 441–457, Aug. 1984, ISSN: 00220248. DOI: 10.1016/0022-0248(84)90036-8.

[97] M. Feng, L. W. Cook, M. M. Tashima, and G. E. Stillman, "Lattice constant, bandgap, thickness, and surface morphology of InGaAsP-InP layers grown by step-cooling, equilibrium-cooling, supercooling and two-phase-solution growth techniques", *Journal of Electronic Materials*, vol. 9, no. 2, pp. 241–280, Mar. 1980, ISSN: 03615235. DOI: 10.1007/BF02670849.

[98] F. Seker, K. Meeker, T. F. Kuech, and A. B. Ellis, "Surface chemistry of prototypical bulk II-VI and III-V semiconductors and implications for chemical sensing", *Chemical Reviews*, vol. 100, no. 7, pp. 2505–2536, 2000, ISSN: 00092665. DOI: 10.1021/cr980093r.

[99] P. Werle, F. Slemr, K. Maurer, R. Kormann, R. Mücke, and B. Jänker, "Near- and mid-infrared laser-optical sensors for gas analysis", *Optics and Lasers in Engineering*, vol. 37, no. 2-3, pp. 101–114, Feb. 2002, ISSN: 01438166. DOI: 10.1016/S0143-8166(01)00092-6.

[100] J. S. Parker, E. J. Norberg, R. S. Guzzon, S. C. Nicholes, and L. A. Coldren, "High verticality InP/InGaAsP etching in Cl2/H2/Ar inductively coupled plasma for photonic integrated circuits", *Journal of Vacuum Science & Technology B, Nanotechnology and Microelectronics: Materials, Processing, Measurement, and Phenomena*, vol. 29, no. 1, p. 011 016, Jan. 2011, ISSN: 2166-2746. DOI: 10.1116/1.3522659.

[101] V. M. Donnelly, "Temperature Dependence of InP and GaAs Etching in a Chlorine Plasma", *Journal of The Electrochemical Society*, vol. 129, no. 11, p. 2533, Nov. 1982, ISSN: 00134651. DOI: 10.1149/1.2123600.

[102] L. Chee-Wei and C. Mee-Koy, "Room-Temperature Inductively Coupled Plasma Etching of InP Using Cl2/N2 and Cl2/CH4/H2", *Chinese Physics Letters*, vol. 23, no. 4, pp. 903–906, Apr. 2006, ISSN: 0256-307X. DOI: 10.1088/0256-307X/23/4/039.

[103] E. S. Aydil and D. J. Economou, "Modeling of Plasma Etching Reactors Including Wafer Heating Effects", *Journal of The Electrochemical Society*, vol. 140, no. 5, p. 1471, May 1993, ISSN: 00134651. DOI: 10.1149/1.2221582.

[104] R. L. Sutherland, D. G. McLean, and S. Kirkpatrick, *Handbook of nonlinear optics.* Marcel Dekker, 2003, p. 971, ISBN: 9780824742430.

[105] M. Bass, C. DeCusatis, J. Enoch, V. Lakshminarayanan, G. Li, C. Macdonald, V. Mahajan, and E. Van Stryland, *Handbook of optics, third edition volume i: Geometrical and physical optics, polarized light, components and instruments(set)*, 3rd ed. New York, NY, USA: McGraw-Hill, Inc., 2010.

[106] J. S. Aitchison, D. C. Hutchings, J. U. Kang, G. I. Stegeman, and A. Villeneuve, "The nonlinear optical properties of AlGaAs at the half band gap", *IEEE Journal of Quantum Electronics*, vol. 33, no. 3, pp. 341–348, Mar. 1997, ISSN: 00189197. DOI: 10.1109/3.556002.

[107] G. Stringfellow, "Miscibility gaps in quaternary III/V alloys", *Journal of Crystal Growth*, vol. 58, no. 1, pp. 194–202, Jun. 1982, ISSN: 0022-0248. DOI: 10.1016/0022-0248(82)90226-3.

[108] G. P. Agrawal, "Nonlinear Fiber Optics", in *Nonlinear Science at the Dawn of the 21st Century*, Berlin, Heidelberg: Springer Berlin Heidelberg, 2000, pp. 195–211, ISBN: 9780123695161. DOI: 10.1007/3-540-46629-0_9. arXiv: arXiv:1011.1669v3.

[109] M. Dinu, F. Quochi, and H. Garcia, "Third-order nonlinearities in silicon at telecom wavelengths", *Applied Physics Letters*, vol. 82, no. 18, pp. 2954–2956, May 2003, ISSN: 00036951. DOI: 10.1063/1.1571665.

[110] B. Monemar, "III-V nitrides—important future electronic materials", *Journal of Materials Science: Materials in Electronics*, vol. 10, no. 4, pp. 227–254, 1999, ISSN: 09574522. DOI: 10.1023/A:1008991414520.

[111] S. Nakamura, T. Mukai, and M. Senoh, "Candela-class high-brightness InGaN/AlGaN double-heterostructure blue-light-emitting diodes", *Applied Physics Letters*, vol. 64, no. 13, pp. 1687–1689, Mar. 1994, ISSN: 00036951. DOI: 10.1063/1.111832.

[112] S. Sheppard, K. Doverspike, W. Pribble, S. Allen, J. Palmour, L. Kehias, and T. Jenkins, "High-power microwave GaN/AlGaN HEMTs on semi-insulating silicon carbide substrates", *IEEE Electron Device Letters*, vol. 20, no. 4, pp. 161–163, Apr. 1999, ISSN: 0741-3106. DOI: 10.1109/55.753753.

[113] T. Miyajima, T. Tojyo, T. Asano, K. Yanashima, S. Kijima, T. Hino, M. Takeya, S. Uchida, S. Tomiya, K. Funato, T. Asatsuma, T. Kobayashi, and M. Ikeda, "GaN-based blue laser diodes", *Journal of Physics: Condensed Matter*, vol. 13, no. 32, pp. 7099–7114, Aug. 2001, ISSN: 0953-8984. DOI: 10.1088/0953-8984/13/32/315.

[114] C. Stampfl and C. G. Van de Walle, "Energetics and electronic structure of stacking faults in AlN, GaN, and InN", *Physical Review B*, vol. 57, no. 24, R15052–R15055, Jun. 1998, ISSN: 0163-1829. DOI: 10.1103/PhysRevB.57.R15052.

[115] D. Kapolnek, X. H. Wu, B. Heying, S. Keller, B. P. Keller, U. K. Mishra, S. P. DenBaars, and J. S. Speck, "Structural evolution in epitaxial metalorganic chemical vapor deposition grown GaN films on sapphire", *Applied Physics Letters*, vol. 67, no. 11, pp. 1541–1543, Sep. 1995, ISSN: 0003-6951. DOI: 10.1063/1.114486.

[116] T. L. Tansley and R. J. Egan, "Point-defect energies in the nitrides of aluminum, gallium, and indium", *Physical Review B*, vol. 45, no. 19, pp. 10 942–10 950, May 1992, ISSN: 0163-1829. DOI: 10.1103/PhysRevB.45.10942.

[117] T. Sugahara, M. Hao, T. Wang, D. Nakagawa, Y. Naoi, K. Nishino, and S. Sakai, "Role of Dislocation in InGaN Phase Separation", *Japanese Journal of Applied Physics*, vol. 37, no. Part 2, No. 10B, pp. L1195–L1198, Oct. 1998, ISSN: 00214922. DOI: 10.1143/JJAP.37.L1195.

[118] M. M. Muhammed, M. Peres, Y. Yamashita, Y. Morishima, S. Sato, N. Franco, K. Lorenz, A. Kuramata, and I. S. Roqan, "High optical and structural quality of GaN epilayers grown on (-201)-oriented beta-Ga2O3", *Applied Physics Letters*, vol. 105, no. 4, p. 042 112, Jul. 2014, ISSN: 0003-6951. DOI: 10.1063/1.4891761.

[119] M. M. Muhammed, M. A. Roldan, Y. Yamashita, S.-L. Sahonta, I. A. Ajia, K. Iizuka, A. Kuramata, C. J. Humphreys, and I. S. Roqan, "High-quality III-nitride films on conductive, transparent (-201)-oriented beta-Ga2O3 using a GaN buffer layer", *Scientific Reports*, vol. 6, no. 1, p. 29 747, Sep. 2016, ISSN: 2045-2322. DOI: 10.1038/srep29747.

[120] G. Yu, G. Wang, H. Ishikawa, M. Umeno, T. Soga, T. Egawa, J. Watanabe, and T. Jimbo, "Optical properties of wurtzite structure GaN on sapphire around fundamental absorption edge", *Applied Physics Letters*, vol. 70, pp. 3209–3211, Jun. 1997, ISSN: 00036951. DOI: 10.1063/1.119157.

[121] M. Rebien, W. Henrion, M. Hong, J. P. Mannaerts, and M. Fleischer, "Optical properties of gallium oxide thin films", *Applied Physics Letters*, vol. 81, no. 2, pp. 250–252, Jul. 2002, ISSN: 0003-6951. DOI: 10.1063/1.1491613.

[122] D. A. Stocker, E. F. Schubert, and J. M. Redwing, "Crystallographic wet chemical etching of GaN", *Applied Physics Letters*, vol. 73, no. 18, pp. 2654–2656, Dec. 1998, ISSN: 00036951. DOI: 10.1063/1.122543.

[123] K. W. Kim, S. D. Jung, D. S. Kim, H. S. Kang, K. S. Im, J. J. Oh, J. B. Ha, J. K. Shin, and J. H. Lee, "Effects of TMAH treatment on device performance of normally off Al 2O3/GaN MOSFET", *IEEE Electron Device Letters*, vol. 32, no. 10, pp. 1376–1378, Oct. 2011, ISSN: 07413106. DOI: 10.1109/LED.2011.2163293.

[124] A. Stolz, E. Cho, E. Dogheche, Y. Androussi, D. Troadec, D. Pavlidis, and D. Decoster, "Optical waveguide loss minimized into gallium nitride based structures grown by metal organic vapor phase epitaxy", *Applied Physics Letters*, vol. 98, no. 16, p. 161 903, Apr. 2011, ISSN: 0003-6951. DOI: 10.1063/1.3582055.

[125] R. Geiss, A. Chowdhury, C. M. Staus, H. M. Ng, S. S. Park, and J. Y. Han, "Low loss GaN at 1550nm", *Applied Physics Letters*, vol. 87, no. 13, p. 132 107, Sep. 2005, ISSN: 0003-6951. DOI: 10.1063/1.2061868.

[126] T. Sekiya, T. Sasaki, and K. Hane, "Design, fabrication, and optical characteristics of freestanding GaN waveguides on silicon substrate", *Journal of Vacuum Science & Technology B, Nanotechnology and Microelectronics: Materials, Processing, Measurement, and Phenomena*, vol. 33, no. 3, p. 031 207, May 2015, ISSN: 2166-2746. DOI: 10.1116/1.4917487.

[127] R. Hui, S. Taherion, Y. Wan, J. Li, S. X. Jin, J. Y. Lin, and H. X. Jiang, "Gan-based waveguide devices for long-wavelength optical communications", *Applied Physics Letters*, vol. 82, no. 9, pp. 1326–1328, 2003, ISSN: 00036951. DOI: 10.1063/1.1557790.

[128] O. Westreich, M. Katz, Y. Paltiel, O. Ternyak, and N. Sicron, "Low propagation loss in GaN/AlGaN-based ridge waveguides", *Physica status solidi (a)*, vol. 212, no. 5, pp. 1043–1048, May 2015, ISSN: 18626300. DOI: 10.1002/pssa.201431663.

[129] O. S. Magaña-Loaiza, B. Gao, S. A. Schulz, K. Awan, J. Upham, K. Dolgaleva, and R. W. Boyd, "Enhanced spectral sensitivity of a chip-scale photonic-crystal slow-light interferometer", *Optics Letters*, vol. 41, no. 7, p. 1431, Apr. 2016, ISSN: 0146-9592. DOI: 10.1364/OL.41.001431. arXiv: 1601.07820.

[130] T. Baba, "Slow light in photonic crystals", *Nature Photonics*, vol. 2, no. 8, pp. 465–473, Aug. 2008, ISSN: 17494885. DOI: 10.1038/nphoton.2008.146. arXiv: 0504112 [physics].

[131] M. Lončar, D. Nedeljković, T. P. Pearsall, J. Vučković, A. Scherer, S. Kuchinsky, and D. C. Allan, "Experimental and theoretical confirmation of Bloch-mode light propagation in planar photonic crystal waveguides", *Applied Physics Letters*, vol. 80, no. 10, pp. 1689–1691, Mar. 2002, ISSN: 00036951. DOI: 10.1063/1.1452791.

[132] T. F. Krauss, "Slow light in photonic crystal waveguides", *Journal of Physics D: Applied Physics*, vol. 40, no. 9, pp. 2666–2670, May 2007, ISSN: 00223727. DOI: 10.1088/0022-3727/40/9/S07.

[133] T. F. Krauss, "Why do we need slow light?", *Nature Photonics*, vol. 2, no. 8, pp. 448–450, Aug. 2008, ISSN: 17494885. DOI: 10.1038/nphoton.2008.139.

[134] B. S. Song, S. Noda, T. Asano, and Y. Akahane, "Ultra-high-Q photonic double-heterostructure nanocavity", *Nature Materials*, vol. 4, no. 3, pp. 207–210, Mar. 2005, ISSN: 14761122. DOI: 10.1038/nmat1320.

[135] J. Li, T. P. White, L. O'Faolain, A. Gomez-Iglesias, and T. F. Krauss, "Systematic design of flat band slow light in photonic crystal waveguides", *Optics Express*, vol. 16, no. 9, p. 6227, Apr. 2008, ISSN: 1094-4087. DOI: 10.1364/OE.16.006227.

[136] S. A. Schulz, J. Upham, F. Bouchard, I. De Leon, E. Karimi, and R. W. Boyd, "Quantifying the impact of proximity error correction on plasmonic metasurfaces [Invited]", *Optical Materials Express*, vol. 5, no. 12, p. 2798, Dec. 2015, ISSN: 2159-3930. DOI: 10.1364/OME.5.002798.

[137] E. Kuramochi, M. Notomi, S. Hughes, A. Shinya, T. Watanabe, and L. Ramunno, "Disorder-induced scattering loss of line-defect waveguides in photonic crystal slabs", *Physical Review B*, vol. 72, no. 16, p. 161 318, Oct. 2005, ISSN: 1098-0121. DOI: 10.1103/PhysRevB.72.161318.

[138] L. O'Faolain, X. Yuan, D. McIntyre, S. Thoms, H. Chong, R. De La Rue, and T. Krauss, "Low-loss propagation in photonic crystal waveguides", *Electronics Letters*, vol. 42, no. 25, p. 1454, 2006, ISSN: 00135194. DOI: 10.1049/el:20063077.

[139] T. Asano, B.-S. Song, and S. Noda, "Analysis of the experimental Q factors (~ 1 million) of photonic crystal nanocavities", *Optics Express*, vol. 14, no. 5, p. 1996, Mar. 2006, ISSN: 1094-4087. DOI: 10.1364/OE.14.001996.

[140] J. Li, L. O'Faolain, S. A. Schulz, and T. F. Krauss, "Low loss propagation in slow light photonic crystal waveguides at group indices up to 60", *Photonics and Nanostructures - Fundamentals and Applications*, vol. 10, no. 4, pp. 589–593, Oct. 2012, ISSN: 1569-4410. DOI: 10.1016/J.PHOTONICS.2012.05.006.

[141] D. M. Beggs, T. P. White, L. O'Faolain, and T. F. Krauss, "Ultracompact and low-power optical switch based on silicon photonic crystals", *Optics Letters*, vol. 33, no. 2, p. 147, Jan. 2008, ISSN: 0146-9592. DOI: 10.1364/OL.33.000147.

[142] K. Hennessy, A. Badolato, A. Tamboli, P. M. Petroff, E. Hu, M. Atatüre, J. Dreiser, and A. Imamoğlu, "Tuning photonic crystal nanocavity modes by wet chemical digital etching", *Applied Physics Letters*, vol. 87, no. 2, p. 021 108, Jul. 2005, ISSN: 0003-6951. DOI: 10.1063/1.1992656.

[143] B.-S. Song, T. Nagashima, T. Asano, and S. Noda, "Resonant-wavelength tuning of a nanocavity by subnanometer control of a two-dimensional silicon-based photonic crystal slab structure.", *Applied optics*, vol. 48, no. 26, pp. 4899–903, Sep. 2009, ISSN: 1539-4522.

[144] A. Gomez-Iglesias, D. O'Brien, L. O'Faolain, A. Miller, and T. F. Krauss, "Direct measurement of the group index of photonic crystal waveguides via Fourier transform spectral interferometry", *Applied Physics Letters*, vol. 90, no. 26, p. 261 107, Jun. 2007, ISSN: 0003-6951. DOI: 10.1063/1.2752761.

[145] D. Taillaert, P. Bienstman, and R. Baets, "Compact efficient broadband grating coupler for silicon-on-insulator waveguides", *Optics Letters*, vol. 29, no. 23, p. 2749, Dec. 2004, ISSN: 0146-9592. DOI: 10.1364/OL.29.002749.

[146] S. Johnson and J. Joannopoulos, "Block-iterative frequency-domain methods for Maxwell's equations in a planewave basis", *Optics Express*, vol. 8, no. 3, p. 173, Jan. 2001, ISSN: 1094-4087. DOI: 10.1364/OE.8.000173.

[147] N. D. M. Von N. W. Ashcroft, "Solid State Physics", *Physik in unserer Zeit*, vol. 9, no. 1, pp. 33–33, Jan. 1978, ISSN: 00319252. DOI: 10.1002/piuz.19780090109.

[148] S. Hughes, L. Ramunno, J. F. Young, and J. E. Sipe, "Extrinsic Optical Scattering Loss in Photonic Crystal Waveguides: Role of Fabrication Disorder and Photon Group Velocity", *Physical Review Letters*, vol. 94, no. 3, p. 033 903, Jan. 2005, ISSN: 0031-9007. DOI: 10.1103/PhysRevLett.94.033903.

[149] S. G. Johnson, M. L. Povinelli, M. Soljačić, A. Karalis, S. Jacobs, and J. D. Joannopoulos, "Roughness losses and volume-current methods in photonic-crystal waveguides", *Applied Physics B*, vol. 81, no. 2-3, pp. 283–293, Jul. 2005, ISSN: 0946-2171. DOI: 10.1007/s00340-005-1823-4.

[150] L. O'Faolain, T. P. White, D. O'Brien, X. Yuan, M. D. Settle, and T. F. Krauss, "Dependence of extrinsic loss on group velocity in photonic crystal waveguides", *Optics Express*, vol. 15, no. 20, pp. 13 129–13 138, Oct. 2007, ISSN: 1094-4087. DOI: 10.1364/OE.15.013129.

[151] B. Wang, S. Mazoyer, J. P. Hugonin, and P. Lalanne, "Backscattering in monomode periodic waveguides", *Physical Review B - Condensed Matter and Materials Physics*, vol. 78, no. 24, p. 245 108, Dec. 2008, ISSN: 10980121. DOI: 10.1103/PhysRevB.78.245108.

[152] M. Patterson, S. Hughes, S. Combrié, N. V. Tran, A. De Rossi, R. Gabet, and Y. Jaouën, "Disorder-induced coherent scattering in slow-light photonic crystal waveguides", *Physical Review Letters*, vol. 102, no. 25, p. 253 903, Jun. 2009, ISSN: 00319007. DOI: 10.1103/PhysRevLett.102.253903. arXiv: 0906.0464.

[153] L. O'Faolain, S. A. Schulz, D. M. Beggs, T. P. White, M. Spasenović, L. Kuipers, F. Morichetti, A. Melloni, S. Mazoyer, J. P. Hugonin, P. Lalanne, and T. F. Krauss, "Loss engineered slow light waveguides", *Optics Express*, vol. 18, no. 26, p. 27 627, Dec. 2010, ISSN: 1094-4087. DOI: 10.1364/OE.18.027627.

[154] G. Mie, "Beitrge zur Optik trber Medien, speziell kolloidaler Metallsungen", *Annalen der Physik*, vol. 330, no. 3, pp. 377–445, Jan. 1908, ISSN: 15213889. DOI: 10.1002/andp.19083300302.

[155] R. H. Ritchie, "Plasma Losses by Fast Electrons in Thin Films", *Physical Review*, vol. 106, no. 5, pp. 874–881, Jun. 1957, ISSN: 0031899X. DOI: 10.1103/PhysRev.106.874.

[156] U. Kreibig and M. Vollmer, *Optical Properties of Metal Clusters*, ser. Springer Series in Materials Science. Berlin, Heidelberg: Springer Berlin Heidelberg, 1995, vol. 25, ISBN: 978-3-642-08191-0. DOI: 10.1007/978-3-662-09109-8. arXiv: arXiv:1011.1669v3.

[157] H. Raether, *Surface Plasmons on Smooth and Rough Surfaces and on Gratings*, ser. Springer Tracts in Modern Physics. Berlin, Heidelberg: Springer Berlin Heidelberg, 1988, vol. 111, ISBN: 978-3-540-17363-2. DOI: 10.1007/BFb0048317.

[158] S. A. Maier, M. L. Brongersma, P. G. Kik, S. Meltzer, A. A. Requicha, and H. A. Atwater, "Plasmonics - A route to nanoscale optical devices", *Advanced Materials*, vol. 13, no. 19, pp. 1501–1505, Sep. 2001, ISSN: 09359648. DOI: 10.1002/1521-4095(200110)13:19<1501::AID-ADMA1501>3.0.CO;2-Z.

[159] S. A. Maier and H. A. Atwater, "Plasmonics: Localization and guiding of electromagnetic energy in metal/dielectric structures", *Journal of Applied Physics*, vol. 98, no. 1, p. 011 101, Jul. 2005, ISSN: 00218979. DOI: 10.1063/1.1951057. arXiv: 1312.6806.

[160] J. Zhang, L. Zhang, and W. Xu, "Surface plasmon polaritons: Physics and applications", *Journal of Physics D: Applied Physics*, vol. 45, no. 11, p. 113 001, Mar. 2012, ISSN: 00223727. DOI: 10.1088/0022-3727/45/11/113001.

[161] W. L. Barnes, A. Dereux, and T. W. Ebbesen, "Surface plasmon subwavelength optics", *Nature*, vol. 424, no. 6950, pp. 824–830, Aug. 2003, ISSN: 00280836. DOI: 10.1038/nature01937. arXiv: 1312.6806.

[162] L. E. Ocola, "Nanoscale geometry assisted proximity effect correction for electron beam direct write nanolithography", *Journal of Vacuum Science & Technology B: Microelectronics and Nanometer Structures*, vol. 27, no. 6, p. 2569, Nov. 2009, ISSN: 10711023. DOI: 10.1116/1.3237135.

[163] T. Klimpel, M. Schulz, R. Zimmermann, H.-J. Stock, and A. Zepka, "Model based hybrid proximity effect correction scheme combining dose modulation and shape adjustments", *Journal of Vacuum Science & Technology B, Nanotechnology and Microelectronics: Materials, Processing, Measurement, and Phenomena*, vol. 29, no. 6, 06F315, Nov. 2011, ISSN: 2166-2746. DOI: 10.1116/1.3662879.